Mechanisms for Charge Selectivity in Photoelectrochemical Systems

by

Aaron James Kaufman

A dissertation accepted and approved in partial fulfillment of the

requirements for the degree of

Doctor of Philosophy

in Chemistry

Dissertation Committee:

Carl Brozek, Chair

Shannon Boettcher, Advisor

George Nazin, Core Member

Benjamin Aleman, Institutional Representative

University of Oregon

Winter 2025

DISSERTATION ABSTRACT

Aaron James Kaufman

Doctor of Philosophy in Chemistry

Title: Mechanisms for Charge Selectivity in Photoelectrochemical Systems

Photoelectrochemical (PEC) systems rely on charge-selective contacts to facilitate electron transfer processes critical for energy conversion reactions. This dissertation examines the fundamental electron transfer mechanisms that enable charge separation at semiconductor-electrocatalyst interfaces. Through experimental studies, we establish that heterojunction formation and the pinch-off effect dominate charge selectivity in a noble metal/III-V photocathode system. Additionally, we develop a wireless photovoltage mapping technique that enables direct measurement of interfacial potential gradients across chemically distinct sites, advancing the characterization of buried charge transfer processes.

Further, this work identifies the presence of adaptive and cooperatively adaptive junctions in $SrTiO_3$-based overall water splitting systems. These mechanisms dictate charge separation efficiency and influence carrier transport at the semiconductor-electrocatalyst interface. The ability of electrocatalysts to dynamically modulate their electronic properties under operating conditions is demonstrated as a key factor in achieving efficient charge selectivity.

The experimental techniques developed in this dissertation advance the characterization of PEC systems, allowing for precise determination of interfacial charge transfer dynamics. The results provide a framework for improving PEC device efficiency by refining material interfaces and optimizing electron transfer pathways. The findings contribute to the broader understanding of interfacial charge dynamics in semiconductor systems and have implications for applications beyond water splitting, including CO2 reduction and nitrogen fixation. By identifying and quantifying dominant charge-selective mechanisms, this work enhances the theoretical and experimental understanding of PEC devices and provides strategies for improving their performance through material and interfacial engineering.

This dissertation includes [previously published] [unpublished] [coauthored] material.

CURRICULUM VITAE

NAME OF AUTHOR: Aaron James Kaufman

GRADUATE AND UNDERGRADUATE SCHOOLS ATTENDED:

University of Oregon, Eugene
University of Oregon, Eugene
University of Wisconsin-Eau Claire, Eau Claire

DEGREES AWARDED:

Doctor of Philosophy, Chemistry, 2025, University of Oregon
Masters of Science, Applied Physics, 2020, University of Oregon
Bachelors of Science, Physics, 2018, University of Wisconsin-Eau Claire

AREAS OF SPECIAL INTEREST:

Electrochemistry
Photoelectrochemistry
Semiconductor Device Physics

PROFESSIONAL EXPERIENCE:

Applied Physics Intern, Nanohmics, Inc., 11 months

GRANTS, AWARDS, AND HONORS:

Knight Campus Transitioning Fellows Scholarship, University of Oregon, 2020
DOE-SCGSR Fellowship S1, Department of Energy Office of Science, 2023

PUBLICATIONS:

Kaufman, A. J.; Nielander, A. C.; Meyer, G. J.; Maldonado, S.; Ardo, S.; Boettcher, S. W. Absolute Band-Edge Energies Are over-Emphasized in the Design of Photoelectrochemical Materials. *Nat Catal* **2024**, *7* (6), 615–623. https://doi.org/10.1038/s41929-024-01161-0.

Kaufman, A. J.; Krivina, R. A.; Shen, M.; Boettcher, S. W. Controlling Catalyst–Semiconductor Contacts: Interfacial Charge Separation in p-InP Photocathodes. *ACS Energy Lett.* **2022**, *7* (1), 541–549. https://doi.org/10.1021/acsenergylett.1c02590.

McKenzie, J.; Pennington, D. L.; Ericson, T.; Cope, E.; **Kaufman, A. J.**; Cozzolino, A. F.; Johnson, D. C.; Kadota, K.; Hendon, C. H.; Brozek, C. K. Tunable Interlayer Interactions in Exfoliated 2D van Der Waals Framework Fe(SCN)2(Pyrazine)2. Advanced Materials 2024, 36 (46), 2409959. https://doi.org/10.1002/adma.202409959.

Shen, M.; **Kaufman, A. J**.; Huang, J.; Price, C.; Boettcher, S. W. Nanoscale Measurements of Charge Transfer at Cocatalyst/Semiconductor Interfaces in BiVO4 Particle Photocatalysts. Nano Lett. 2022, 22 (23), 9493–9499. https://doi.org/10.1021/acs.nanolett.2c03592.

[unpublished work at the time of submission]

Kaufman, A.J., Boettcher, S. W. Cooperatively Adaptive Junctions on Single Crystal $SrTiO_3$. (*2024 draft produced*), Manuscript in preparation. Target Journal: Nature Materials

Kaufman, A.J., Crumlin, E.J., Boettcher, S. W. Wireless Photovoltage Using Ambient Pressure X-ray Photoelectron Spectroscopy. (*2024 draft produced*), Manuscript in preparation. Target Journal: ACS Energy Letters

Kaufman, A.J., Crumlin, E.J., Boettcher, S. W. APXPS Photovoltage Measurement Through a Heterojunction on Pt|InOx|p-InP Photocathode. (*2024 draft produced*), Manuscript in preparation. Target Journal: ACS Applied Materials & Interfaces (Letters Section)

ACKNOWLEDGMENTS

I would like to express my gratitude to my advisor, Dr. Shannon Boettcher, for his guidance, support, and mentorship throughout my research journey. His insights and expertise have been invaluable in shaping my scientific approach and understanding of photoelectrochemical systems. The investigations of the works within this manuscript were supported in part by the Department of Energy (DOE), Basic Energy Science (BES), grant no. DE-SC0014279. I would also like to thank the Department of Energy Office of Science Graduate Student Research (SCGSR) program for its support of my research. A special thanks to my DOE-SCGSR advisor, Dr. Ethan Crumlin, for his invaluable mentorship and guidance. I am also grateful to the members of his research group for their collaboration and support during my time working with them.

I am incredibly grateful to my lab mates for their collaboration and camaraderie. In particular, I would like to thank Liam Twight and Nick D'Antona for their friendship and encouragement. Their support made even the most challenging moments of research more manageable and enjoyable. I extend my appreciation to my undergraduate mentees, Kaden Wheeler and Sawyer Lazar. Kaden, who has continued his academic journey by pursuing a Ph.D. at the University of Southern California, and Sawyer, who is now pursuing a Ph.D. at the University of North Carolina at Chapel Hill, have both demonstrated dedication and enthusiasm that made mentoring a truly rewarding experience.

I would also like to acknowledge the staff at CAMCOR for their technical expertise and support. Dr. Steve Golledge provided invaluable guidance with XPS, Steve Wiemholt provided

expertise in repairing technical instruments, and Kurt Langworthy offered essential leadership as Director. Their assistance greatly enhanced the quality of my research. Additionally, I am thankful to the members of the Knight Campus Internship Program, particularly Dr. Fuding Lin, for his thoughtful conversations over tea, and the administrative team, including Betsy Tanenbaum and Lynde Ritzow, for their support. Finally, I would like to express my gratitude to the Chemistry administrative office staff, including Christi Mabinuori, Carissa Bosch, and all other administrators who have facilitated my research and academic progress. Their dedication ensures that students and researchers can focus on their work without administrative hurdles.

I would like to thank my family and my fiancée Megan for their love and support.

To everyone who has played a role in my academic and professional journey, thank you for your support, guidance, and encouragement.

Table of Contents

Chapter Page

LIST OF FIGURES

Figure Page

LIST OF TABLES

Chapter 1: INTRODUCTION TO TECHNIQUES AND MECHANISMS

Section A. Introduction and overview

Photoelectrochemical (PEC) systems offer a promising pathway for sustainable energy conversion, yet the fundamental mechanisms governing charge selectivity at semiconductor-electrocatalyst interfaces remain poorly understood. This dissertation investigates these mechanisms through a combination of advanced experimental techniques, providing new insights into interfacial charge dynamics that are critical for improving PEC device efficiency. This chapter contains three sections introducing the reader to techniques and mechanisms used and proposed throughout this document and a completed peer reviewed perspective published in Nature Communications. This introduction will equip the readers with the language and concepts used and provide the governing framework for Photoelectrochemical (PEC) systems.

The first technique that will be described is the dual-working-electrode (DWE) featured in subsequent chapters. This technique was used in Chapter 2 to identify change to the Pt|p-InP photocathode interface after preparation, during and after electrochemical operation. The DWE technique provided the first clues as to the mechanism that governs the Pt|p-InP. These insights moved the study to the nano scale, where electrocatalyst patterning by electrodeposition or by electron beam lithography defined nanostructures on chemically controlled interfaces. These nanoscopic junctions were interrogated by conductive atomic force microscopy, (c-AFM) which identified and measured the emergence of a nano-scale charge selective mechanism called the pinch-off effect. While later shown to be a short lived mechanism, it illustrated a clear transition

in junction properties and highlighted the dominant mechanism called a heterojunction formation on this III/V photocathode.

The following chapter, Chapter 3, will focus on the development of a wireless photovoltage measurement technique. In PEC systems, photovoltage is the driving force for electrochemical reactions and is a product of charge selective contacts. Therefore, this new technique both provides a wireless measurement of the driving force for reactions while simultaneously highlighting the mechanisms which enabled it, through chemically distinct mapping of photovoltage. This technique uses ambient pressure x-ray photoelectron spectroscopy (AP-XPS) to measure the photovoltage established at chemically distinct sites. To develop this technique, interdigitated top-contact Schottky solar cells on silicon were fabricated to verify and identify challenges with this technique, (here the Schottky junction is the mechanism for carrier selectivity). This completed work is to be submitted for review by the time of this oral defense.

The final section of Chapter 3 utilized the wireless photovoltage mapping by AP-XPS to revisit and characterize the buried InOx|pInP heterojunction which was identified in Chapter 2. Conventional voltage measurement techniques are not able to measure such a junction. This completed work, to be submitted as a short letter, highlights wireless photovoltage mapping's unique capability to measure charge selectivity through complex geometries and across heterogeneous materials.

The final research chapter of this work investigates the mechanisms which govern overall water splitting (OWS) PEC systems. In OWS, the system needs to drive two half reactions. In the case studied within this work, the OWS system of $SrTiO_3$ nanoparticles drives both the HER and the OER on separate electrocatalyst sites decorated on the nanoparticle. In Chapter 4, I use

the DWE technique on single crystals of $SrTiO_3$ to investigate the adaptive junction mechanism for carrier selective contacts at the Pt|n-STO and the CoOx|n-STO interfaces. This work further employs common three electrode characterization techniques such as cyclic voltammetry (CV) and staircase potentio electrochemical impedance spectroscopy (SPEIS) or the Mott-Schottky technique to illustrate small asymmetries in exposed crystal facets. Finally, the AP-XPS was used to measure and confirm cooperative adaptive junctions of Pt and CoOx on a single crystal of $SrTiO_3$ <111>. Chapter 4 embodies a complete work to be submitted near the time of this defense.

Section B, Mechanisms

Five mechanisms for carrier selective contacts are discussed within this work, including the heterojunction mechanism, pinch-off effect, buried junction (introduced as the Schottky junction), the adaptive junction, and the cooperative adaptive junction. Each of these mechanisms provide a framework to understand how each contact selectively collects the desired carrier and generates free-energy to drive the energetically uphill electrochemical reactions of hydrogen and oxygen bonds breaking and forming. These mechanisms are proposed to be wider reaching than only serving water splitting chemistry. The same concepts could be applied to photoelectrochemical conversion processes, like CO_2 reduction, Nitrogen fixation, and glycerol oxidation

These mechanisms do not need to be mutually exclusive. For instance, illustrated in chapter 2, The pinch-off effect was observed at the nanoscale and may still play a role in determining Pt|p-Inp electron selectivity but the heterojunction mechanism was observed to dominate.

Section C, Perspective

Paper A: Absolute band-edge energies are over-emphasized in the design of photoelectrochemical materials:

Aaron J. Kaufman†, Adam C. Nielander†, Gerald J. Meyer†, Stephen Maldonado†, Shane Ardo† & Shannon W. Boettcher†. *Nat Catal* **7**, 615–623 (2024).

†These authors contributed equally to this work

This section contains co-authored work previously published in *Nature Catalysis* in 2024. Reproduced with permission from [*Nat Catal* **7**, 615–623 (2024)]. Aaron J. Kaufman and Shannon W. Boettcher initiated the Perspective. Aaron J. Kaufman wrote the first draft and generated its figures. Adam C. Nielander, Gerald J. Meyer, Stephen Maldonado and Shane Ardo edited and contributed substantially to articulating the concepts. Aaron J. Kaufman and Shannon W. Boettcher wrote the final paper with input from all authors.

Introduction:

Suppose one desires to identify a semiconductor material that can photoreduce a species with a formal reduction potential $\varepsilon^{\circ\prime}$. Such a reduction could be a one-electron transfer for application in organic synthesis, environmental remediation or solar energy conversion, or a kinetically complex multi-electron transfer as in the reduction of H_2O or H^+ to H_2 fuel. A typical starting point would be to consult a photoelectrochemistry review article for the band-edge positions of semiconducting materials relative to the vacuum energy level and/or standard hydrogen electrode energy level, typically in an aqueous electrolyte[1-4]. With the knowledge that

bandgap photoexcitation creates electron–hole pairs that relax/thermalize to the band edges before interfacial electron transfer occurs, an inspection of the tabulated conduction-band-edge energy (E_c) relative to $-q\varepsilon^{\circ\prime}$ would allow one to predict whether a given semiconductor was appropriate for the desired reaction (the variables used in this contribution are defined in Table A.S1). One might also conclude that interfacial electron transfer from the semiconductor into solution would not occur at all if $-q\varepsilon^{\circ\prime} > E_c$, that is, if the reduction potential lies above the conduction-band energy. These ideas are misleading and are often not the limiting property for photoelectrochemical devices and particulate photocatalysts. Distinct rate processes developing excess charge, described in this Perspective, can move the tabulated E_c value relative to the $-q\varepsilon^{\circ\prime}$ without a chemical transformation. A reduction potential that falls outside the semiconductor bandgap may impact the current–voltage behavior and voltage-dependent interfacial kinetics, but does not in fact preclude facile electron transfer.

Tabulated band-edge positions are poor indicators of interfacial redox chemistry because they are not singular parameters—they are sensitive to the chemical environment and surface chemistry and are modulated by interface electrostatics. The free energies of non-equilibrium electronic charge carriers (for example, the hole and electron quasi-Fermi levels) in a semiconductor, at steady state and under illumination, determine their ability to drive overall reactions and perform chemical work[5]. The degree to which the quasi-Fermi levels split under illumination, in turn, depends on the kinetics of charge transfer; that is, the surfaces or interfaces acting as charge-carrier-selective contacts, not on the absolute band-edge energies. In this Perspective, we discuss the origins of the common misconception that absolute band edges are critical and illustrate the underlying design principles for improved materials and interfaces, operative charge-

separation/collection mechanisms and stabilization strategies at semiconductor/electrolyte interfaces.

Governing Equations:

The purpose of this section is to show how the band-edge positions are not the critical parameters for the selection of semiconductors because they shift in response to carrier accumulation and surface chemistry. Consider a semiconductor without dopants and without interfacial electric fields at equilibrium (that is, the so-called flat-band condition). With generality to molecular, particulate and bulk semiconductor photoabsorbers, we can write the following equilibrium expressions for a pair of redox reactions (either outer-sphere one-electron reactions or multi-step electron-transfer reactions) that include both electrons (e_{cb}^{-}), holes (h_{vb}^{+}), and O (oxidized) and R (reduced) species, with the specific charge not included for simplicity of notation:

$$\text{Reaction 1: } \nu_1 e_{cb}^{-} + O_1 \underset{k'_{1,et}}{\overset{k_{1,et}}{\rightleftharpoons}} R_1, \quad \nu_1 h_{vb}^{+} + R_1 \underset{k'_{1,ht}}{\overset{k_{1,ht}}{\rightleftharpoons}} O_1 \tag{A.1}$$

$$\text{Reaction 2: } \nu_2 e_{cb}^{-} + O_2 \underset{k'_{2,et}}{\overset{k_{2,et}}{\rightleftharpoons}} R_2, \quad \nu_2 h_{vb}^{+} + R_2 \underset{k'_{2,ht}}{\overset{k_{2,ht}}{\rightleftharpoons}} O_2 \tag{A.2}$$

Marcus theory shows how the standard electron-transfer rate constant for an outer-sphere redox reaction (that is, where electron transfer is across the double layer) can be expressed in terms of the energy difference between the band edge and redox energy[6,7]. While in some (ideal) cases Marcus theory describes the kinetics of electron transfer from a semiconductor to molecular acceptors[8,9], photochemical fuel-forming reactions do not generally proceed as purely outer-sphere reactions, but instead involve catalytic species and mechanistic steps with inner-sphere

intermediates (that is, species that may interact in the strong-coupling limit)[10]. Furthermore, band-edge positions are generally unknown under the experimental conditions of interest as they are not singular parameters. Ab initio calculations can provide a guide, but are limited in that they assume an atomic-scale structure and termination of the active surface and interface solvent/double-layer structure that is typically experimentally unknown. Predicting rate constants for practically relevant photoelectrochemical processes thus remains a major challenge.

The free energy of charge carriers in a semiconductor is described by their electrochemical potential ($\bar{\mu}_i^{\alpha}$). In general, assuming thermal equilibrium, for species *i* in phase α:

$$\bar{\mu}_i^{\alpha} = \mu_i^{\alpha} + z_i F \phi^{\alpha} = (\mu_i^{0\alpha} + RT \ln a_i^{\alpha}) + z_i F \phi^{\alpha} = \left(\frac{\partial G}{\partial \nu_i}\right)_{T,P,\nu_{j\neq i}} \quad \text{(A.3)}$$

Under illumination, one can separate the electrochemical potential of conduction band electrons from valence band holes. In semiconductor physics, these quantities are termed the electron and hole quasi-Fermi levels (E_{fn} and E_{fp}, respectively). Although quasi-Fermi levels are understood for populations of electronic charge carriers, the concept applies in the ergodic limit to individual species[11]. For example, if a semiconductor particle is sufficiently small so that there are few excited carriers, the time-averaged behavior is equivalent to the ensemble average across many particles, and energies can be described in terms of the quasi-Fermi level. Regardless of the band-edge position under the flat-band condition, the quasi-electrochemical potentials of conduction-band electrons and valence-band holes in the photoabsorber ($\bar{\mu}_n^{\mathrm{absr}}$ and $\bar{\mu}_p^{\mathrm{absr}}$, respectively) will tend towards equilibrium, transferring charge according to equations (A.1) and (A.2), or via the recombination of electrons and holes at the surface and within the bulk of the photoabsorber. To drive an overall uphill $\Delta G_{\mathrm{rxn}} > 0$) chemical reaction with light, the quasi-

Fermi-level splitting (E_{fn} - E_{fp}) must be greater in magnitude than ΔG_{rxn} under steady-state reaction conditions (and relevant species activities at the surface). Differences between $E_{fn}$and E_{fp}beyond this minimum energy value are needed due to associated kinetic (catalytic) and mass-transport energy losses.

Semiconductor/liquid junctions:

Next consider a wide-bandgap ($\mathbf{E}_g \approx 3$–4 eV) semiconductor particle with a conduction band energy (or equivalently potential, which is the energy per charge on the relevant reference scale) that is not high enough to drive the hydrogen evolution reaction (that is, not reducing enough to drive the reduction of H_2O or H^+ to form H_2) but a valence band energy that is substantially below (that is, more oxidizing) the reversible oxygen reduction potential (Fig. A.1). Under illumination, a small photoexcited carrier concentration (n' and p') is needed to produce the minimum thermodynamically required difference between $\bar{\mu}_n^{\mathrm{absr}}$ and -$\bar{\mu}_p^{\mathrm{absr}}$ to drive water splitting because of the low equilibrium concentrations of holes and electrons (n^{eq} and p^{eq}) in a wide-bandgap semiconductor. The total free energy available to drive chemical reactions is given by the difference between the electron and hole quasi-Fermi levels (or equivalent electrochemical potentials) according to equation (A.4).

$$E_{fn} - E_{fp} = \mathbf{E}_g + RT \ln \frac{n'p'}{N_C N_V} = RT \ln \frac{n'p'}{{n_i}^2} > \Delta G_{\mathrm{rxn}} \; (+ \Delta G_{\mathrm{losses}}) \qquad \text{(A.4)}$$

where n_i is the intrinsic carrier concentration ΔG_{rxn} and $\Delta G_{\mathrm{losses}}$ are the molar free energy of the reaction and that lost to the environment leading to inefficiency. Note

that equation (A.4) does not include variables associated with the kinetics of the electron-transfer reactions or the absolute band-edge positions.

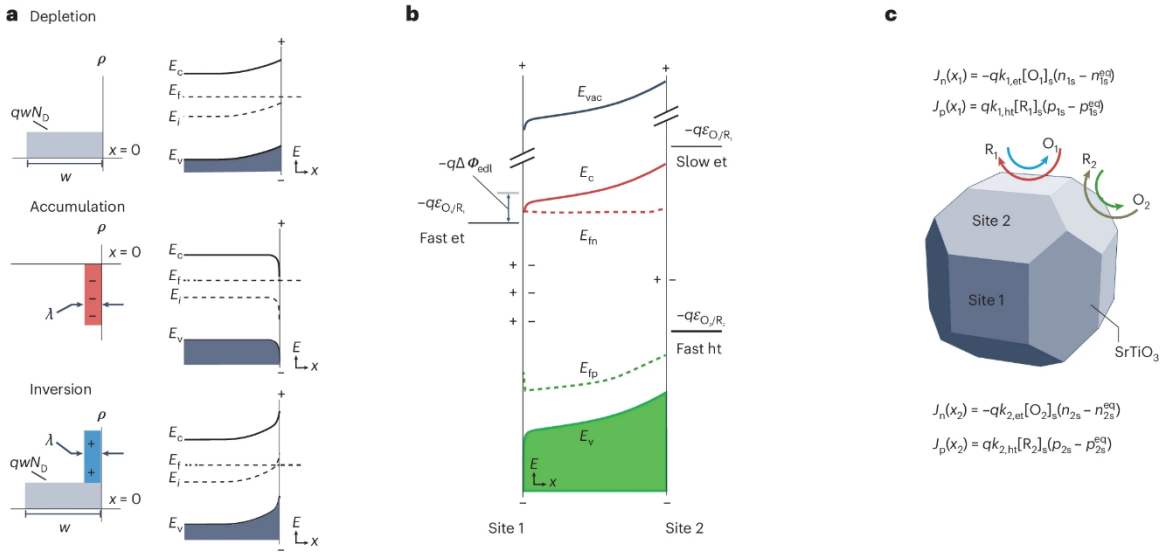

Figure A.1. Interface energies and reactions. a, Excess charge-carrier-density plots (left) and band diagrams (right) for an n-type semiconductor in depletion, accumulation and inversion due to equilibration with a contacting phase (for example, redox species). b, Depleted photoabsorber particle (site 2) driving misaligned half reactions under illumination (simulated one-dimensional COMSOL Multiphysics model, $N_D = 10^{14}$ cm^{-3}, length = 1 μm, and disparate electron-transfer (et) and hole-transfer (ht) rates at the electron- and hole-selective contacts, respectively). Accumulated surface electrons (site 1) pull up the photoabsorber energy levels relative to $q\mathcal{E}_{O_1/R_1}$ by an electrostatic potential energy $q\Delta\phi_{edl}$, allowing photoexcited electrons to drive a reduction reaction on the semiconductor surface whose energy is out of the bandgap. c, Possible facet-dependent oxidation and reduction kinetics and rate equations quantifying charge-carrier selectivity, as discussed in the text.

How can both electrons and holes transfer if the conduction-band-edge energy is not high enough to drive the reaction? Consider the following qualitative picture. The kinetics of hole transfer from semiconductor to solution species initially will be fast as the valence band holes are quite oxidizing, while electrons transfer slowly. This will lead to a build-up of negative electron charge on/in the semiconductor, which is equivalent to an applied negative bias that raises the electron quasi-Fermi level and eventually the band edges, increasing the reducing power of the

photoexcited electrons. This process will occur until the rates of both hole and electron transfer are equal (at steady state). If the semiconductor particle is already doped n-type, as most metal oxides used in water splitting are[12-15], this negative charging under photoexcitation is termed majority carrier accumulation (electrons in an n-type semiconductor). The same phenomena can occur with the addition of excess minority carriers (holes in an n-type semiconductor), which is called inversion. The excess mobile carriers reside close to the surface of the semiconductor, typically within the first few atomic layers, as required by Gauss's law (Figure A.1a). This analysis assumes that there is no chemical change (for example, cation intercalation/deintercalation, changing surface termination or surface oxidation) that modifies the surface electrochemical potential without requiring the development of excess space charge—such processes can also play an important role in dictating interfacial energetics[16-18].

Experimental data support the qualitative picture outlined above[19-22]. Grimm et al. showed systematic control of the interface photovoltage in H- and CH_3-terminated crystalline p-Si and n-Si photoelectrodes, governed by the reversible potential of the solution redox couple (Figure A.2a)[22]. These surfaces have low defect densities, with nearly every Si surface atom chemically terminated. If the redox potential of the solution was outside the bandgap of Si (that is, under flat-band conditions), the interface was driven into either inversion, where the minority carrier concentration at the surface exceeds that of the majority carriers in the semiconductor bulk, or accumulation, where excess majority carriers are at the surface[23]. Inversion creates the functional equivalent of a buried junction, leading to high photovoltages, while accumulation leads to an Ohmic contact between the solution and semiconductor.

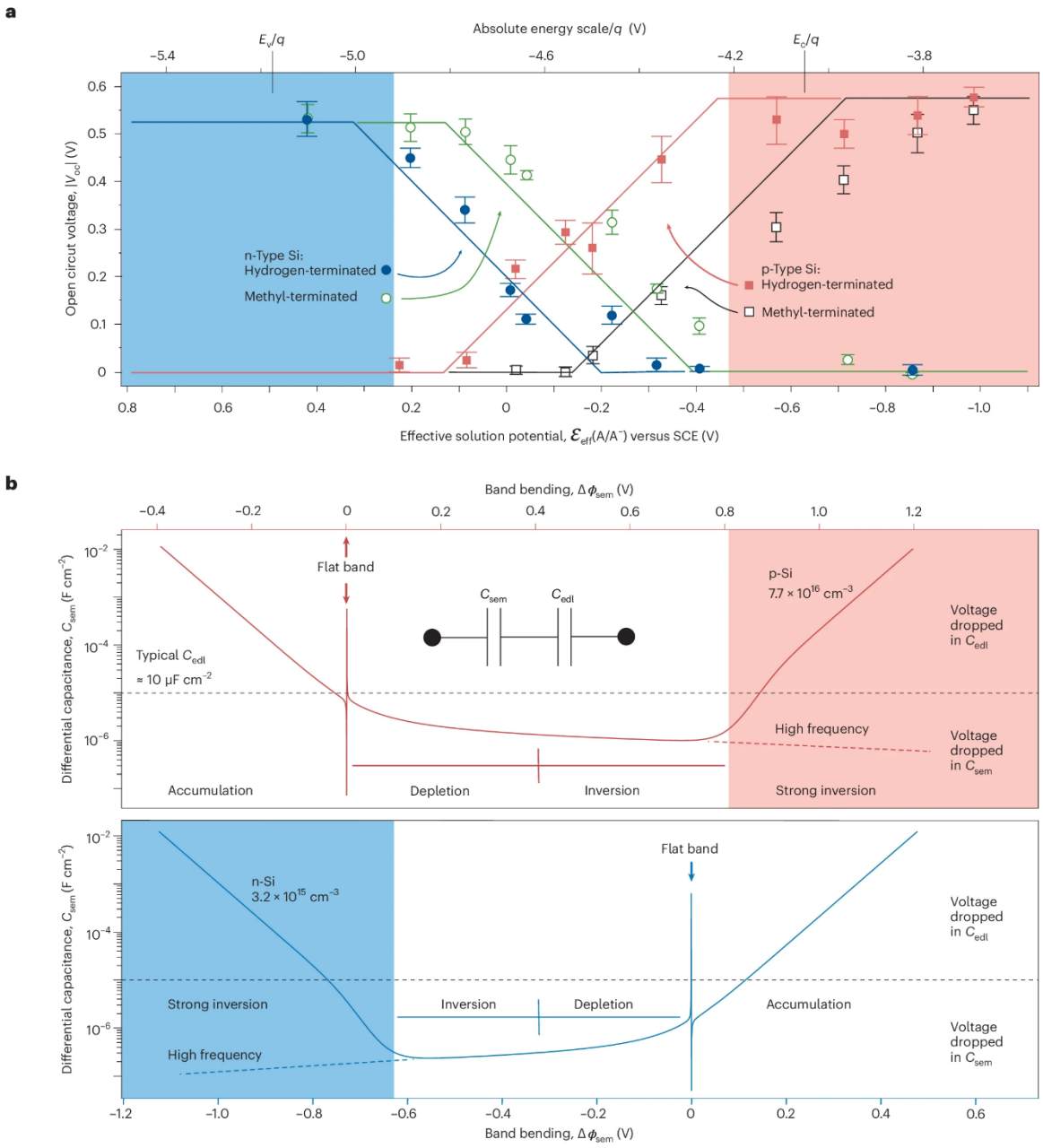

Figure A.2. Accumulation, depletion and inversion at photochemical junctions. a, The absolute value of V_{oc} ($|V_{oc}|$) measured for n- and p-type H- and CH_3-terminated Si with corresponding error bars as a function of the reducing power of the A/A^- redox couple in the electrolyte, $\mathcal{E}_{eff}(A/A^-)$; data from ref. [22]) that is aligned with the absolute energy scale and the differential capacitances in b. The solid lines are a guide to the eye and show the trends. Here, V_{oc} was directly measured from the semiconductor against a Pt electrode poised at the Nernstian potential of the solution ($\mathcal{E}(A/A^-)$) and plotted against the effective solution potential ($\mathcal{E}_{eff}(A/A^-)$), normalizing the minority-carrier acceptor concentration to 10 mM. The regions highlighted in blue and red correspond to strong inversion for n-type Si (dopant density of 3×10^{15} cm^{-3}) and p-type Si (dopant density of 8×10^{16} cm^{-3}), respectively. b, Semiconductor differential capacitance (C_{sem}) for p-type Si (top) and n-type Si (bottom) at 295 K, taken from

the calculated space-charge density[24], as a function of band bending ($\Delta\phi_{sem}$). The vertical asymptotes correspond to flat-band potentials. C_{sem} values have been plotted using the same dopant density as used by Grimm et al.[22] A double-layer capacitance (C_{edl}) of 10 μF cm^{-2} is shown as an approximate reference for relative voltage drops ($\Delta\phi_{edl}$, $\Delta\phi_{sem}$). The expected high-frequency dark response in the inversion region is shown by a dashed line when the rate of generation of the minority carrier at the surface is low.

While the regenerative photoelectrochemical cell architecture used by Grimm et al. has only one electrochemically active semiconductor interface, the demonstration of large (bulk-recombination-limited) photovoltages with solution potentials outside the absolute-energy limits of the Si bandgap is conceptually the same as the picture for the hypothetical wide-bandgap semiconductor described above. For example, the difference between the H- and CH_3-terminated surfaces leads to a systematic shift in the band-edge positions of ~0.4 V due to changes in the interface dipole. Regardless, there is no change in the maximum interface photovoltage or the ability to drive any given redox reaction irrespective of the reaction's redox potential[25]. The relative positions of the solution reduction potential/energy and the band edge energy positions do not determine the photochemical reactions that photoexcited carriers can drive. In fact, the highest photovoltages were observed for a p-Si photoelectrode in contact with a redox couple, dimethylcobaltocene (Figure A.2a), whose reduction potential close to −1 V versus the saturated calomel electrode (SCE) is much more negative than the conduction band edge (at flat band) for Si at about −0.6 V versus SCE[24,26]. The absolute conduction band energy/potential value is irrelevant for determining which reductions p-Si can drive due to, in this case, carrier inversion.

Evidence for inversion has been reported at photoelectrochemical interfaces via near-surface channel conductance measurements[27], photocapacitance[28] and infrared spectroscopy[29].

In the absence of other observations, the data in Figure A.2a could also be explained by densities of surface states that prevent larger degrees of band bending and high photovoltages (that is, surface-state-induced Fermi-level pinning) [30,31]. However, near-surface channel conductance measurements on some of the systems are inconsistent with this possibility[27]. Nevertheless, when large densities of surface states do cause Fermi-level pinning, the resultant photoelectrode behavior is like that of a buried junction or a photoelectrode in inversion—the photovoltage is independent of the redox potential of the solution and the absolute band-edge energies remain irrelevant with respect to which reactions can be driven.

The data in Figure A.2a come from measurements of the semiconductor operating under accumulation, depletion, or inversion conditions, which can be understood with equivalent-circuit models. At semiconductor/liquid junctions, the simplest model consists of two capacitors, one representing the charge stored in the semiconductor space charge region (C_{sem}) and the other the Helmholtz double layer (C_{edl}). More complex models that include a diffuse layer, interfacial surface states and other corrections can also be used[3], but they are not needed to illustrate accumulation, depletion and inversion conditions. The absolute electrostatic potential drops across

the space charge region ($\Delta\phi_{sem}$) and double layer ($\Delta\phi_{edl}$) are inversely related to their relative capacitances by the conservation of charge (equation (A.5)), where equilibration of the surface electrochemical potential sets the degree of band bending and therefore the potential dropped in the semiconductor ($\Delta\phi_{sem}$; Figure A.2b).

$$\frac{\Delta\phi_{\mathrm{sem}}}{\Delta\phi_{\mathrm{edl}}} = \frac{C_{\mathrm{edl}}}{C_{\mathrm{sem}}} \tag{A.5}$$

The surface charge and C_{sem} depend on the applied potential in a manner that can be calculated from carrier statistics and Poisson's equation[24], but the key point is that the magnitudes of the potential drops in each region depend on both C_{sem} and C_{edl}. The value of $\Delta\phi$ is thus larger across the region with the smaller capacitance between C_{sem} and C_{edl}. Simply, the smaller capacitance reflects where the electrostatic potential change is larger. Plots of measured capacitance as a function of electrode potential may thus illustrate when accumulation or depletion conditions are operative, but such data are rarely reported, presumably due to the presence of surface states[32].

As a semiconductor electrode is biased into accumulation, the experimentally measured capacitance (C_{exp}) increases and saturates to the value of C_{edl}. In this condition, $\Delta\phi_{edl}$ is larger than $\Delta\phi_{sem}$. That is, applying a bias to a semiconductor electrode in accumulation does not substantially move the (quasi-)Fermi levels relative to the band edges. Instead, the applied bias primarily shifts the band edges relative to a reference point in solution. Through equation (A.5), the quantity of

charge from majority carriers (that is, $\Delta\phi_{sem} \times C_{sem}$) accumulated at the semiconductor surface must be counterbalanced exactly by the charge from ions in solution (that is, $\Delta\phi_{edl} \times C_{edl}$) gathered at the interface. Physically, the availability of ions from solution at this location is limiting because the abundance of majority carriers from within the semiconductor at the surface is large in accumulation, that is, C_{exp} tends to C_{edl}.

In depletion, the opposite is true. C_{exp} tends to C_{sem} because the total charge from the majority carriers in the semiconductor space charge region is much smaller than from the available ions in solution that could move to the interface. Correspondingly, $\Delta\phi_{sem}$ is substantially larger than $\Delta\phi_{edl}$ in depletion. This statement is equivalent to stating that the applied bias moves the (quasi-)Fermi levels relative to a reference point in solution, but the band-edge values are largely unchanged relative to that same reference point.

In accumulation, the interpretation of $\Delta\phi_{sem}$ is straightforward. C_{sem} is effectively independent of time/frequency because the equilibration of majority carriers from the bulk to the interface is fast on the relevant timescale of the impedance measurement. In inversion, the interpretation of $\Delta\phi_{sem}$ is more nuanced. C_{sem} can have a measurable time dependence as the supply of minority carriers to the surface depends on an interplay between the rate of thermal generation, drift, losses from recombination and consumption from interfacial processes. Accordingly, the measured capacitance–potential profile in inversion is a function of the frequency of

measurement/observation (Figure A.2b, dashed versus solid line) and is strongly influenced by the operative kinetics of minority-carrier generation, transport, trapping and transfer[33]. This is why Mott–Schottky plots of impedance often remain linear in inversion at potentials well past the band edge and can make the increase in measured capacitance due to inversion difficult to observe[32,34-40].

Nanoscopic and molecular systems:

In a bulk semiconductor, the number of band-edge states is large compared with the number of carriers at the surface. Thus, the chemical potential at the surface does not change with the build-up of charge (that is, the activity term $a_i\alpha$ for charge carriers in equation (A.3) becomes nearly constant and is unaffected by further changes in carrier density at the surface, as in a polarized metal electrode).

Nanoscopic and molecular systems show similar behaviour (Figure A.3), but there are differences. Semiconductor nanoparticles are typically (practically) undoped, that is, their size limits the number of atomic substitutions. Yet, under illumination, they can accumulate electrons or holes at steady state. In general, the rates of photochemical electron and hole transfer are not initially identical following illumination. When the system reaches steady state, by definition, the time derivatives of all concentrations are zero. This means that the concentrations of electrons and holes build up to different extents such that it is the rates of photochemical electron and hole transfer that are ultimately balanced. This process leads to a steady-state electrostatic potential

developing across the nanoparticle/solution interface. This change in $\Delta\phi$ moves the energies of the band edges relative to the solution reduction potential (or energy) for the reasons stated above. The steady-state electron and hole concentrations are thus defined by the reactant and product concentrations, charge-transfer rate constants and relevant generation/recombination mechanisms and rates.

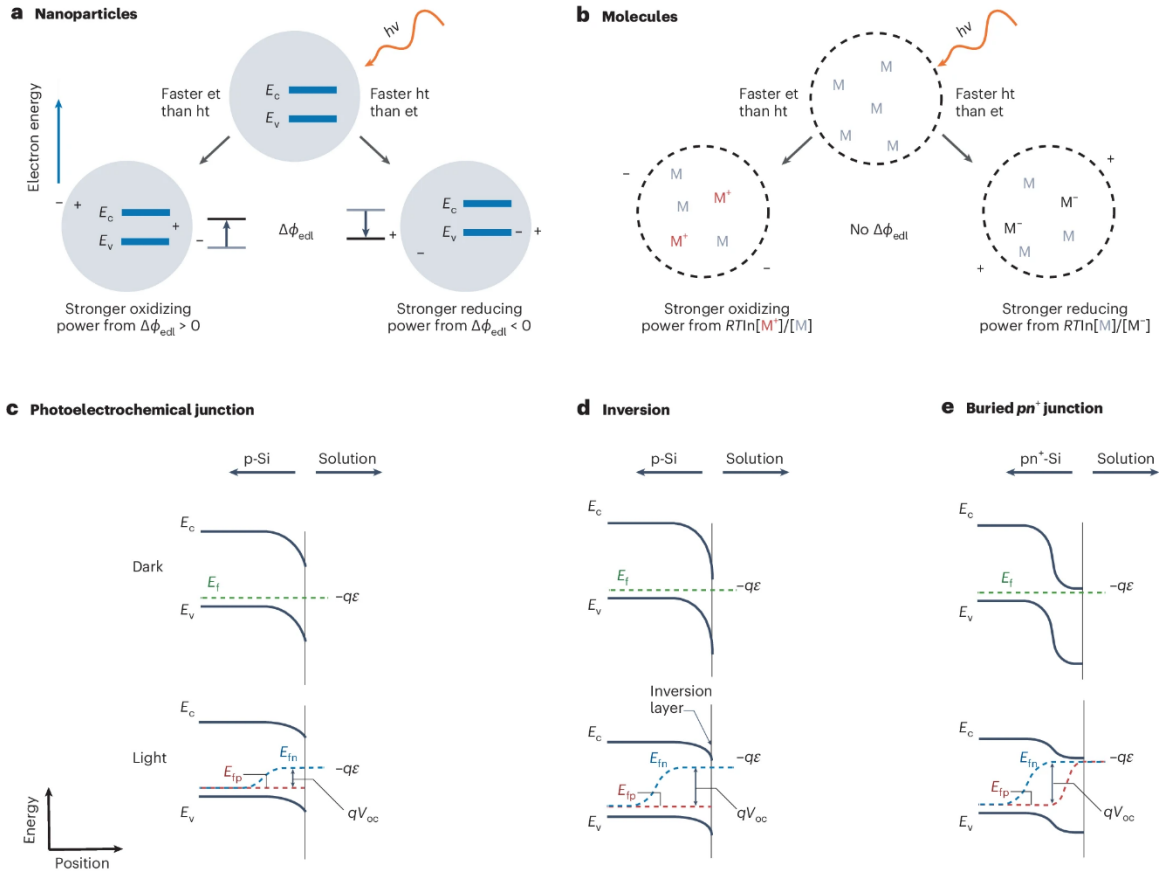

Figure A.3. Band diagrams and photochemical charge accumulation in nanoscopic and molecular systems. a, Due to the kinetic limitations of either electron transfer (et) or hole transfer (ht), nanoparticles can accumulate either multiple electrons or holes, respectively, at steady state. This process leads to changes in the reducing or oxidizing power of the carriers associated with changes in electrostatic potential profiles. b, Molecular energy levels are typically well spaced, leading to changes in the reducing or oxidizing power of the ensemble via effects described by the Nernst equation and thus are more limited in range. c–e, Example band diagrams in the dark and under illumination for a photoelectrochemical junction in typical depletion conditions (c), with an inversion layer (d) and with a buried pn^+ junction (e).

Note that both the inversion layer and the buried junction can equivalently shift E_c and E_v relative to the solution redox potential, as in this example, due to an additional electric potential drop across the electrical double layer.

For soluble molecular systems (M), the initial rates of electron and hole transfer will also not be identical in the ensemble of individual molecules. Molecular systems can thus also accumulate M^- or M^+ at steady state (representing an additional negative or positive charge on M, which may also be initially charged). This process shifts the Nernst potential of the redox solution containing the ensemble of molecules through a change in the activities:

$$\mathcal{E}_{M^+/M} = \mathcal{E}^{\mathrm{o}}_{M^+/M} + \frac{RT}{nF}\ln\frac{a_{M^+}}{a_{\mathrm{M}}} \tag{A.6}$$

and

$$\mathcal{E}_{M/M^-} = \mathcal{E}^{\mathrm{o}}_{M/M^-} + \frac{RT}{nF}\ln\frac{a_{M}}{a_{M^-}} \tag{A.7}$$

We note that this is different from a semiconductor particle that can build up charge at one energy level (the band edge) as electronic states are closely packed in energy. In a molecule, the electronic states are usually widely spaced in energy and thus this is not generally possible. Hence, there is no mechanism to smoothly vary the electric potential term for molecular systems via a process analogous to accumulation or inversion in a semiconductor. Instead, changes in chemical potential dominate contributions to changes in free energy under photoexcitation. As such, the primary mechanism to change the oxidation or reduction strength of a specific molecular chromophore is to change the activity/concentration of the oxidized or reduced species.

The importance of charge-transfer kinetics and interface/contact selectivity

If band-edge energy positions (at flat band) do not matter much for semiconductor photoelectrochemistry, what does? Charge-transfer kinetics and interface charge-carrier selectivity are crucial. Consider a photoelectrode that has been fabricated to have a buried n^+p junction, such as Pt/n^+p-Si, and used as an efficient photocathode for photoelectrochemical H_2 production (Figure A.3)[4]. The n^+p junction is selective towards the collection of photoexcited electrons over holes because of the higher conductivity of electrons compared with holes in the n^+ region[41]. Pt makes an Ohmic, unselective contact with the n^+-Si surface (emitter) layer, but that is inconsequential to the system behaviour because the n^+-Si layer is very thin and absorbs little light; the photocurrent is dominated by electron–hole pairs that separate at the n^+p junction before reaching the Pt/n^+-Si junction. The n^+p junction here is functionally equivalent to the case of strong inversion. Such an interface can be contrasted with Pt/p-Si, which is not very selective towards electrons over holes because the relative lack of interfacial band bending leads to substantial surface hole concentrations and hole conductivity. In all these cases, the absolute band edges of the semiconductor are irrelevant to the ability of the photoelectrode to drive an efficient Faradaic reaction.

In a simple model including carrier generation and interfacial charge transfer, Roe et. al. derived the limits on $V_{\mathrm{oc}} \leq (E_{fn} - E_{fp})/q$ across a two-contact (photovoltaic or photochemical) device. The set of four rate equations for electron and hole partial currents, $J_n(x)$ and $J_p(x)$, at contacts x_1 and x_2 are given in Figure A.1 (ref. [42]). The out-of-equilibrium surface electron and hole densities, $\Delta n = (n_x - n_x^{eq})$ and $\Delta p = (p_x - p_x^{eq})$, under illumination drive electron and hole partial currents. The magnitude of the current response is related directly to the kinetics of

electron or hole transfer ($k_{1,et}$ or $k_{1,ht}$) and local species concentrations or, similarly, the equilibrium-exchange-current densities (J_{0n}^{x} and J_{0p}^{x}). The terms J_{0n}^{x} and J_{0p}^{x} define $(E_{fn} - E_{fp})/q$ and V_{oc} under steady-state illumination, and therefore the maximum free energy available to do work. Interfacial kinetics places limits on the maximum uphill chemical reaction that a photoabsorber can drive. This kinetic model applies identically to photoabsorbers beyond bulk semiconductors, including particulate photocatalysts, and could be adapted to molecular absorbers.

In particulate semiconductor photoelectrochemistry, the above considerations simultaneously apply to two spatially separated contacts on the same light-absorbing particle, with one contact selectively collecting electrons and the other holes[43-45]. The carrier selectivity of these contacts, along with the inherent properties of the semiconductor (mobility, lifetime, absorption coefficient), determine the ability of the semiconductor to drive any given photochemical reaction with a specific ΔG_{rxn}. The measured absolute band-edge energies are of limited importance. Because many tests are carried out with sacrificial electron or hole acceptors (thus leading to the case where ΔG_{rxn} is near zero or even negative and spontaneous without light), understanding of the underlying physics has often been obscured. One example of such a system is the black (defective) TiO_2, which makes large amounts of H_2 under illumination only in the presence of fast sacrificial hole acceptors, despite the likely low absolute energy of the conduction band defect states and probable lack of photovoltage generation[46].

Corrosion and band edge energies:

Gerischer proposed that semiconductors are inherently unstable in photoelectrochemical systems when the standard potentials for corrosion/decomposition are situated within the band edges[47]. For example, the anodic reaction $CdS + 2h^{+} \rightarrow Cd^{2+} + S$ has a standard potential more negative

on an electrochemical scale than the valence band of CdS. As a result, n-CdS is thermodynamically unstable in water under illumination. However, this does not mean that n-CdS and other semiconductors with similar energetics cannot function meaningfully as photoelectrodes in water. The prolonged and stabilized operation of n-type CdS, ZnO, Cu_2O, CdTe and metal dichalcogenide photoanodes in water has been achieved through the manipulation of interfacial kinetics in two ways. One strategy is to alter the electrolyte chemistry so that the redox reactions of interest greatly outpace the undesirable corrosion reactions for the flux of photogenerated carriers. Kinetic strategies that speed up the rate of productive reactions for electrons and holes through electrocatalysis will lower the steady-state population of electrons and holes at the surface (and quasi-Fermi-level splitting), also suppressing the competing corrosion reactions[48]. A second strategy is to coat the semiconductor surface with a protective thin film that specifically impedes corrosion/decomposition processes[49-51]. Such protective surface layers generally form a buried-junction-type structure where the charge-carrier selectivity of the passivating surface layer in contact with the bulk semiconductor controls the ability of the semiconductor to drive a specific reaction. We also note that because corrosion reactions take place on the semiconductor surface, and thus inside the electrical double layer, their relative potentials shift in the same way as the band-edge potential if the semiconductor moves into inversion or accumulation, that is, corrosion reactions are not outer-sphere processes.

Conclusion:

We have clarified a common misconception of band-edge alignment with reduction potentials as a key material design principle for photocatalysts. Semiconductor absorbers can support excess charge densities where the kinetics of surface reactions will determine the resulting products.

This clarification enables research of perhaps previously ignored materials and informs design principles for photocatalyst systems engineering for both one-electron redox reactions and more-complex multi-electron-transfer reactions (for example, H_2 evolution, H_2O oxidation and CO_2 reduction). In multi-electron-transfer reactions, charge often accumulates at surface sites and how that charge is screened by electrolyte ions determines whether or not the apparent band edges shift with charge accumulation[15]. In the search for earth-abundant and efficient photocatalysts, the two primary materials properties of importance are sufficient optoelectronic properties of the absorber (optical absorption coefficient and free-carrier lifetime) and the ability to make both hole- and electron-carrier-selective contacts that connect the semiconductor with the catalytic sites that drive the oxidation and reduction half reactions of interest.

Chapter 2: PINCH-OFF EFFECT AND HETEROJUNCTION GOVERNING A III/V PHOTOCATHODE SYSTEM

Paper B: Controlling Catalyst-Semiconductor Contacts: Interfacial Charge Separation in p-InP Photocathodes

.

Aaron J. Kaufman, Raina A. Krivina, Meikun Shen, & Shannon W. Boettcher. *ACS Energy Lett.* 2022, 7, 1, 541–549

 Aaron J. Kaufman and Shannon W. Boettcher. conceived the experiments and led the project. Raina A. Krivina collected, processed, and consulted on XPS data analysis. TEM images were collected by Peter Eschbach, Facility Director at Oregon State University Electron Microscopy Facility. Aaron J. Kaufman conducted all other experiments. Aaron J. Kaufman and Shannon W. Boettcher analyzed the data and wrote the manuscript with input from all authors.

Introduction:

Photoelectrochemical (PEC) water splitting produces H_2 from water and light and offers the possibility of integrating solar-energy conversion with storage, ideally leading to simple lower-cost device architectures. InP is particularly well-suited for efficient conversion of solar to chemical energy because of its ideal bandgap of 1.35 eV, high electron mobility, and low surface-recombination velocity.[1-3] To achieve high efficiency, however, the surface must be coated with electrocatalysts. Pt/p-InP and Pt/p-$Ga_xIn_{1-x}P$, for example, reduce protons with high photocathode efficiency (>12%) and external quantum efficiency (>80%).[2] While Pt is among the most-active for the hydrogen-evolution reaction (HER), Pt also has a high work function (5.65 eV) that is consequently aligned with the Fermi level of p-type InP.[2, 4] For example, p-InP with an acceptor concentration of 4×10^{17} cm^{-3} has a Fermi level (5.64 eV) that is more positive than that of Pt (on the vacuum scale), which should form an ohmic, non-carrier-selective contact (i.e., a Schottky barrier of zero) based on conventional theories of metal–semiconductor contacts.[5] However, when this combination is used in photoelectrodes, a rectifying, Schottky-like contact is formed that leads to interfacial photovoltages of >0.7 V and high photocathode efficiencies.[2-3, 6] More-recent work has used TiO_2 interlayers to protect the InP, which further appear to increase the interface photovoltage.[7] An improved understanding of the mechanisms for selective collection of photoexcited minority carriers over majority carriers at catalyst/semiconductor interfaces would facilitate the design of durable and efficient photoelectrodes from InP specifically and more generally illustrate design principles that can be translated to other material systems.

There are several possible explanations for the high photocathode efficiencies for p-InP with Pt and other noble-metal catalyst layers. Heller et al. noticed that, for Pt, Ru, or Rh, irrespective of

the metal-catalyst work function, the open-circuit voltage (V_{oc}) of the catalyzed photocathode was similar and approached that expected for p-InP contacted with the H^+/H_2 redox couple (0.9 ± 0.2 eV).[1-3] They hypothesized that H_2 permeates the metal catalyst, accumulates at the interface, and sets an interfacial barrier height that leads to high electron selectivity at the H–Pt/p-InP junction (Figure B.1a). Aspnes et al. showed in a dry two-electrode system that an H_2 gas atmosphere led to increased rectification of the Pt/p-InP interface, purportedly due to modulation of the Pt work function.[3] Recently, Nunes et al. reported that an interfacial oxide coupled with an H_2 gas atmosphere also yields increased electronic barriers/photovoltages in the "theoretically" ohmic Pt/p-Si system.[8]

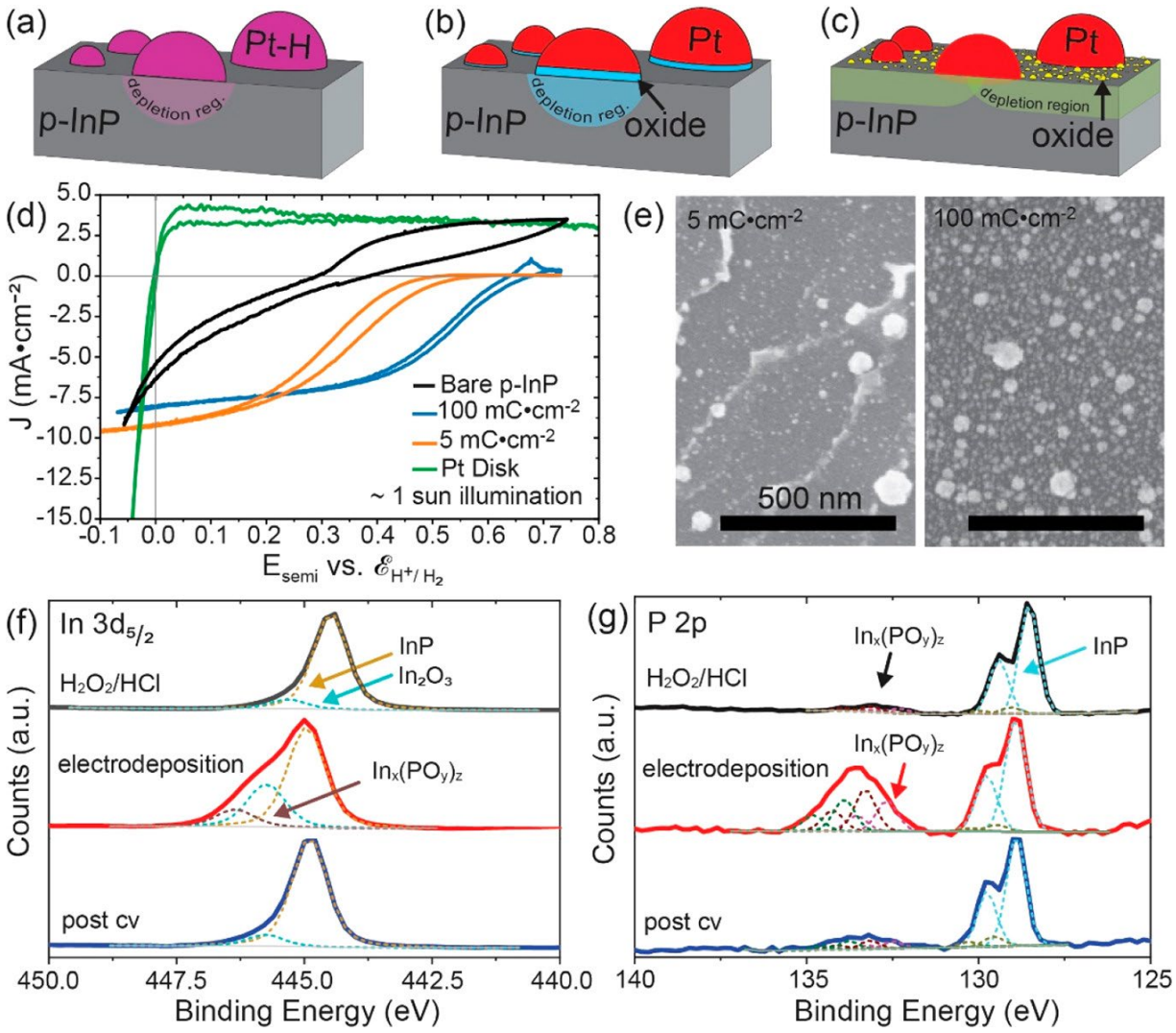

Figure B.1. Survey of Pt|p-InP junctions. Possible mechanisms of interfacial charge-carrier selectivity in Pt/p-InP photocathodes. (a) Adaptive-junction behavior caused by Pt alloying with H2 thus lowering its work function. (b) Heterojunction formation by an interfacial oxide. (c) Pinch-off effect caused by a peripheral material increasing the effective barrier at the catalyst/semiconductor interface. (d) Typical photoelectrode J–E curves in 1 M HClO4 illuminated at ~100 mW cm–2 of solar simulation, for two Pt loading conditions (100 and 5 mC cm–2 of charge passed during Pt photoelectrodeposition). (e) SEM images of the two samples at the same scale. (f) XPS spectra of the In 3d5/2 peak show surface conversion of the InP to In2O3 from H2O2/HCl pretreatment to postelectrodeposition of Pt; the In2O3 persists while higher-energy suboxides diminish after illuminated cyclic voltammetry. The shift to higher binding energy of all of the In species is thought to originate from surface-charging effects, as the Pt 4f peaks did not shift. Changes in band bending may also play a role in the shift. (g) Phosphate species of mixed ratios seen near 133 eV in the P 2p spectra were most prevalent after electrodeposition and persist in greater amounts than after etching pretreatment.

A second mechanism that could modulate the catalyst/semiconductor interface is the formation of an interfacial oxide (Figure B.1b). InP naturally forms a surface oxide consisting of $In_x(PO_3)_z$, $In(PO_4)$, P_2O_5, and In_2O_3 when exposed to air and/or aqueous solution under anodic conditions.[6, 9-15] In_2O_3 is typically a conductive n-type oxide; however, it is soluble at the low pH used in electrolytes for these InP photocathodes. This complex oxide may grow directly on p-InP and undercut the Pt particles or form through thin catalyst films *via* oxygen diffusion at defects or pinholes. This n-type oxide could generate an electron-selective contact due to the high conductivity of electrons (over holes) as discussed by Würfel broadly in the context of photovoltaic devices.[16] Such an interlayer might govern the nature of the junction irrespective of the metal-catalyst deposited on the upmost layer. The construction of n-In_2O_3/p-InP heterojunction solid-state solar cells, for example, is known.[17]

The nanoscale size of the metal-catalyst contacts to the p-InP could also be important (Figure B.1c). Nanoparticle layers usually result from the photoelectrodeposition of metals on semiconductor surfaces and are often intentionally sought to reduce parasitic optical absorption in the catalyst layer. We previously showed that for Ni nanoparticles contacting n-Si photoanodes, smaller particles give rise to dramatically larger photovoltages and photoelectrode efficiency.[18] This observation was quantitatively explained by the pinch-off effect for heterogeneous nonuniform Schottky contacts. When the radius of nanoscale contacts is similar in dimension to the depletion-region depth in the regions surrounding the nanoscale contacts, a new effective barrier describes the transport through the contac.[18-21] This effective barrier may be modeled analytically by Tung's patch theory to predict a photovoltage that depends on metal nanocontact (catalyst particle) radius (see the Supporting Information).[21]

Herein, we use a combination of macroscale photoelectrode measurements, surface-sensitive spectroscopies, conducting atomic force microscopy (C-AFM), and transmission electron microscopy (TEM), on both well-defined nanopatterned Pt and heterogeneous electrodeposited Pt on p-InP, to illustrate the roles the physical phenomena outlined above play in controlling the charge-carrier selectivity at the catalyzed photochemical junction. Specifically, we discover that hydrogen adsorption/alloying with Pt catalyst material alone is insufficient to explain the large photovoltages at the Pt/p-InP interface, in contradiction to earlier findings. Instead, the formation of an n-type In-rich oxide between the Pt and p-InP appears essential to generate an interface that selectively collects electrons over holes. We further find that the pinch-off effect is indeed critical in setting the interface selectivity at Pt nanoparticles on p-InP prior to the formation of an interface oxide, but that after photochemical testing is not significantly important. These results are useful because they illustrate how to engineer interfaces between active catalyst materials and semiconductor absorbers independent of the specific work function of the catalyst and in ways not easily predicted based on traditional Schottky-contact theory. These insights are relevant not only to designing higher-efficiency III–V photocathodes from InP and $Ga_xIn_{1-x}P$ materials but also for more complicated systems like oxide photocatalyst particles where precise control over doping and materials composition is not possible.[7, 22-26]

Interface Selectivity:

All PEC devices must generate a gradient in the electrochemical potential of electrons ($\nabla\bar{\mu_n}$) and holes ($\nabla\bar{\mu_p}$) to separate and collect photogenerated carriers. This can be realized by different relative electron and hole conductivities at the two contacts to the semiconductor absorber. In a typical photoelectrode, the catalyst surface layer or particles must comprise one selective contact,

while the electrical back contact comprises the other. Alternatively, in a dispersed photocatalyst particle that drives both cathodic and anodic reactions on the same absorber, two different, and spatially separated, catalyst sites must yield independent hole- and electron-selective contacts. The profiles in $\bar{\mu}_n$ and $\bar{\mu}_p$ are parameters, however, which one cannot readily engineer. Instead, the relative electron and hole conductivities at each contact are usually controlled with a heterojunction or *via* band bending that depletes the majority carrier.[16] The local electron or hole currents j_n or j_p at a contact are related to the local conductivities σ_n and σ_p and $\nabla\bar{\mu}_n$ and $\nabla\bar{\mu}_p$.

$$j_n = \frac{-\sigma_n}{q}\nabla\bar{\mu}_n \tag{B.1}$$

$$j_p = \frac{\sigma_p}{q}\nabla\bar{\mu}_p \tag{B.2}$$

These physics similarly control the performance of contacts in photovoltaic devices. Lonergan and co-workers described selective contacts under open-circuit conditions and determined the limits of photovoltage between the two contacts, V_{oc}. In the context of a photoelectrode, V_{oc} is the steady-state voltage that develops under illumination between the catalyst layer (usually collecting minority carriers) and the back contact to the semiconductor. Lonergan defines the selectivity, *S*, as the ratio in partial equilibrium-exchange current densities at the respective contact, denoted $\boldsymbol{J_0}$ and j_0 for the dominate and secondary carrier at the semiconductor/contact interface.[27]

$$V_{oc} = \frac{k_b T}{q}\ln(S), S = \frac{\boldsymbol{J_0}}{j_0} \tag{B.3}$$

A key fundamental challenge in semiconductor photoelectrochemistry, therefore, is to achieve control over the catalyst/semiconductor contact selectivity to allow for the generation of high photovoltages and photocurrents.

Interface Measurements:

Figure B.1d shows conventional (macroscopic) photoelectrochemical analysis of p-InP photocathodes coated with electrodeposited Pt nanoparticles (SEM micrographs in Figure B.1e). The data show that the Pt particles on p-InP selectively collect photoexcited electrons because the photovoltage is substantial (∼0.7 V), and significant photocurrents attributed to HER on the Pt particle surface are measured (∼10 mA cm^{-2}). To explore the factors affecting this electron collection, we compare two different Pt loadings photoelectrodeposited with 100 and 5 mC cm^{-2} of integrated cathodic charge passed during Pt deposition from a chloroplatinic acid solution (after an H_2O_2/HCl etch to remove surface oxides). While the V_{oc} and photocurrents for the two samples are similar (Figure B.1d, blue and orange curves), the slope of the *J–E* curves near the open-circuit potential are different. For the sample with 100 mC cm^{-2} of Pt deposition charge, the *J–E* curve approaches the open-circuit potential near 0.7 V vs the reversible hydrogen electrode (RHE) with a steep slope. In contrast, the *J–E* curve for the 5 mC cm^{-2} has a shallow slope near V_{oc} suggestive of a tunnel barrier between the Pt and p-InP that is impeding charge transport.[28] The higher density of electrodeposited Pt for the 100 mC cm^{-2} sample apparently reduces the effect of this tunnel barrier. To understand this in more detail, it is necessary to uncover the chemical composition of the interfaces, particularly after photoelectrochemical cycling.[6, 25]

Ex situ X-ray photoelectron spectroscopy (XPS) of the p-InP photocathode was used to analyze the surface composition. A control p-InP sample pretreated with H_2O_2/HCl yields a clean InP peak in the In $3d_{5/2}$ peak (Figure B.1f) and the P 2p (Figure B.1g) spectrum with the absence of significant surface oxide that was present in the as-received sample (Figure B.S1). After

H_2O_2/HCl treatment and the electrodeposition of 5 mC cm^{-2} of Pt, an increase in binding energy for the InP peak in the In $3d_{5/2}$ spectra is observed which agrees with literature values for In_2O_3.[9, 11, 13] A mixed indium phosphate peak at higher binding energies is found in the P 2p spectra. Following 1 dark and 5 illuminated CV cycles in 1 M $HClO_4$, the In_2O_3 peak remains but the relative intensity of the mixed indium-phosphate peak decreased (see the discussion of peak position and chemical analysis in the Supporting Information). The presence of a mixed In_2O_3 and $In_x(PO_y)_z$ on InP has been observed previously.[6, 9-12, 29] The presence of this mixed oxide observed by XPS coincides with carrier-selective junction behavior we find in the macroscopic photoelectrode *J–E* curves (Figure B.1d).

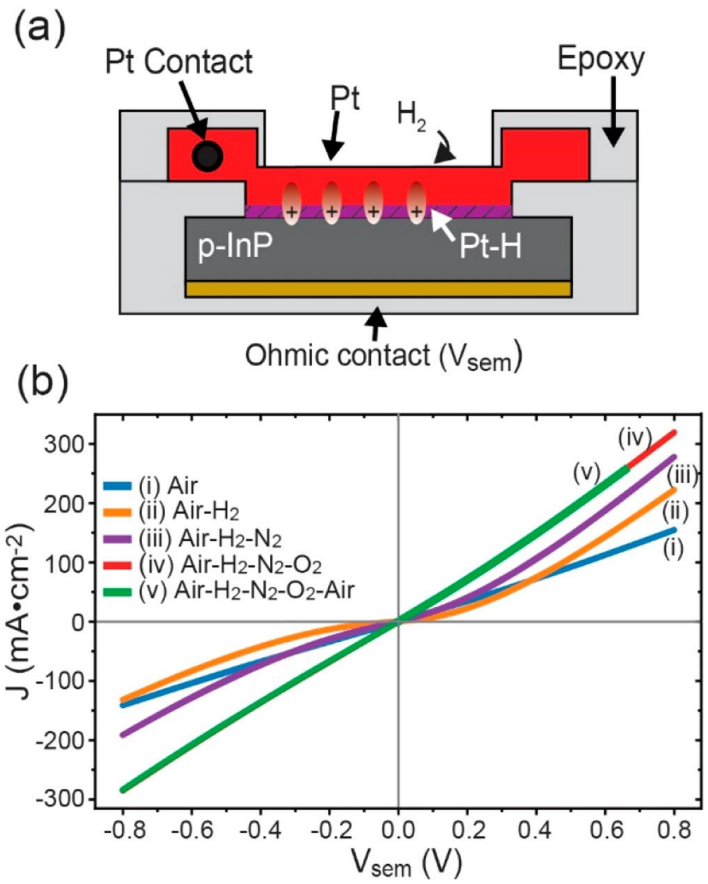

Figure B.2. Effect of H_2 on Pt/p-InP interface. (a) Device geometry with top contact to the Pt thin film illustrating one possible mechanism for the formation of electron-selective contacts. H_2 reacts with the Pt thin film to form Pt–H which affects the dipole at the Pt/p-InP interface. (b) Results of dry, macroscopic, two-electrode *J–V* curves of contacts made by depositing 40 nm of Pt by electron-beam deposition on p-InP (pretreated with conc. HCl) that display ohmic behavior. After treatment with H_2 for 10 min (curve ii), the response deviates from linearity, but no large barrier is apparent. Exposure to an oxidizing O_2/air atmosphere returns the linear *J–V* response, consistent with loss of absorbed hydrogen.

To study the effects of ambient H_2 on the electrical characteristics of the junction, a 40 nm Pt film was deposited by electron-beam deposition on the p-InP. The creation of a Pt–H interfacial dipole (Figure B.2a) formed by the dissociation and diffusion of protons to the Pt(film)/p-InP interface, as in metal/insulator/semiconductor gas-sensor devices, could lower the apparent work function and develop an energetic barrier for holes.[30-32] The nonlinear *J–V* curves in Figure B.2b show that the H_2 indeed induces a small barrier at the Pt(film)/p-InP junction, but the overall *J–V* characteristics remained nearly symmetric. The developed barrier was reversibly eliminated after the junction was reintroduced to an O_2-containing atmosphere. The absorption of H_2, and

the hypothesized Pt work function lowering implied by Figures B.2b and B.3c, is consistent with the H_2 gas sensor literature.[30-32] However, this mechanism was not observed to transition the pristine Pt(film)/p-InP ohmic junction to a rectifying, electron-selective contact observed in the *operando* data shown in Figure B.1d (Pt particles) and Figure B.3c (Pt film).[30, 32]

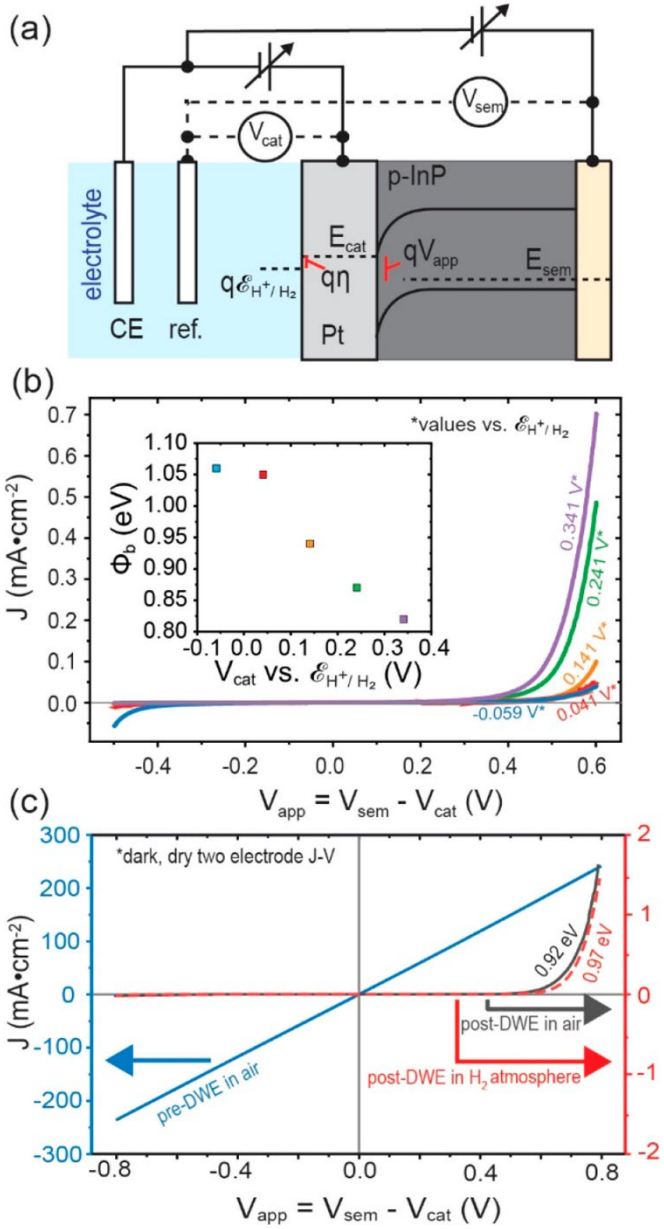

Figure B.3. *Operando* dual-working-electrode experiments. (a) DWE PEC experiment schematic. (b) J–V_{app} response as V_{cat} (E_{cat}/q) is controlled relative to a reference electrode (the values of V_{cat} for each curve are labeled next to each versus RHE). The inset plots the calculated barrier height from the Schottky diode equation with respect to V_{cat}. J–V curves shift positive at V_{cat} values approaching 0 V vs. RHE, indicative of the barrier height increase

with decreasing V_{cat} evident in the inset. (c) Dry two-electrode measurements before and after the DWE experiment illustrate an irreversible shift from ohmic to rectifying. The apparent Schottky barrier heights from fitting the *J–V* curves are printed next to each curve.

The dual-working-electrode (DWE) PEC configuration was then used to study the *operando* Pt/p-InP junction behavior. Figure B.3a illustrates the hypothesized Schottky-like junction formed between Pt and p-InP and how the electrode potentials are sensed and controlled. With DWE PEC the applied potential between semiconductor back contact and catalyst, V_{app}, can be controlled and measured directly. We measure the current across the Pt(film)/p-InP junction while simultaneously poising V_{cat} (i.e. E_{cat}/q) at various potentials versus the reference electrode in the electrolyte. The $J–V_{app}$ characteristics of the junction were rectifying under *operando* conditions, which is different than the ohmic behavior observed *ex situ*. As discussed below, we propose an interfacial oxide layer grows by diffusing to the interface through the Pt film. This interfacial oxide likely dictates the junction properties. The irreversible change observed in the *J–V* curves after the DWE experiment in Figure B.3c contrasts the reversible Pt work-function lowering caused by H_2 absorption in Figure B.2b and suggests a permanent transition, like that of Pt/p-InP converting to a Pt/InO_x/p-InP heterojunction. Additionally, the measured current in Figure B.3c was nearly 2 orders of magnitude lower after DWE PEC experiments than before, indicating a more resistive junction. V_{cat} was stepped from 0.241 V to −0.059 V then stepped back to 0.341 V vs RHE in 1 V increments. Calculated from the Schottky diode equation, barrier heights in Figure B.3b increased systematically with more-negative V_{cat} indicative of a degree of adaptive-junction behavior, but they level off at V_{cat} more negative than the RHE.[18, 33-34] The largest barrier heights, >1 eV, are similar to those observed in In_2O_3/p-InP heterojunctions.[17] At V_{cat} positive of RHE, the barrier height of the interfacial oxide linearly tracked with V_{cat}, probably due to

electrochemical doping of the newly formed interfacial oxide. More negative V_{cat} would be expected to increase its Fermi level as the oxide is reduced and charge-compensating protons intercalated, leading to the observed adaptive-junction behavior.[35-39] We propose the constant barrier height observed at potentials near, and more negative than, the RHE is fixed by the redox potential of H^+/H_2.[2] At more-negative potentials than the RHE the Pt catalyst and InO_x is fixed at the redox potential of H^+/H_2, and the remaining voltage is dropped in the double layer of the electrolyte rather than in the oxide. The calculated barrier height was observed to reversibly decrease when qV_{cat} was returned positive to 0.341 V vs RHE. While the small change in barrier height (Δ = 0.24 eV in Figure B.3b inset) was observed to be reversible from qV_{cat} −0.059 to 0.341 V vs RHE under electrochemical conditions, the dry *J–V* characteristics were not reversible from before to after the DWE experiment (Figure B.3c) (*i.e.*, which changed from ohmic to rectifying). After the *operando* DWE measurements, the dry junction was still sensitive to H_2 gas with a calculated barrier height increase of 0.05 eV under H_2. This was, however, a factor of 5 smaller change than the increase during electrochemical reduction of protons.

As opposed to the thin-film Pt catalyst layers described above, most photoelectrodes use nanoparticle catalysts to decrease parasitic light absorption. Catalyst nanocontacts, however, often display differing electrical properties than their thin-film analogues.[18] Dry, conducting AFM (C-AFM) was thus used to measure the electrical-transport properties across individual Pt nanocontacts. Semiconductor photoelectrodes are usually decorated with electrocatalyst particles by electrodeposition.[2, 22] By controlling the integrated cathodic charge during photoelectrodeposition, we produced a range of Pt particle densities (Figure B.S7). The 5 mC cm^{-2} samples were used for their low particle densities with a variety of diameters which could be independently measured by C-AFM on a single electrode (Figure B.S7). *J–V* curves from

electrodeposited Pt particles displayed a barrier of 0.86 ± 0.16 eV independent of particle size (Figure B.S8). The InP surface for these samples also contained substantial In_2O_3 and $InPO_x$ (based on XPS analysis) after electrodeposition.

To assess the role of nanocontacts in the absence of substantial interfacial oxide, we then studied Pt nanoparticles on p-InP defined by electron-beam lithography (EBL). Surface oxides were removed by H_2O_2/HCl etching, and nanodisk arrays were created by EBL. Immediately following preparation, the nanocontacts were analyzed by C-AFM and illuminated C-AFM (Figure B.4a). The largest disk, approximately 250 nm in radius, displayed nearly ohmic current–voltage (*J–V*) response with a small photovoltage (0.05 V). The smallest disk, approximately 50 nm, displayed a Schottky-like *J–V* response with a larger photovoltage (0.48 V). The inverse trend of photovoltage with disk radii is exemplified across many contacts and samples in Figure B.4b. The same sample was subject to further oxidation in humid, room-temperature air and reanalyzed by illuminated C-AFM. A similar trend in photovoltage was observed with an increase in photovoltage at all radii. The dependence of V_{oc} on particle radius was not observed on EBL-defined nanodisks after being subject to dark and light CV in 1 M $HClO_4$, but rather a roughly constant V_{oc} at all radii was observed.

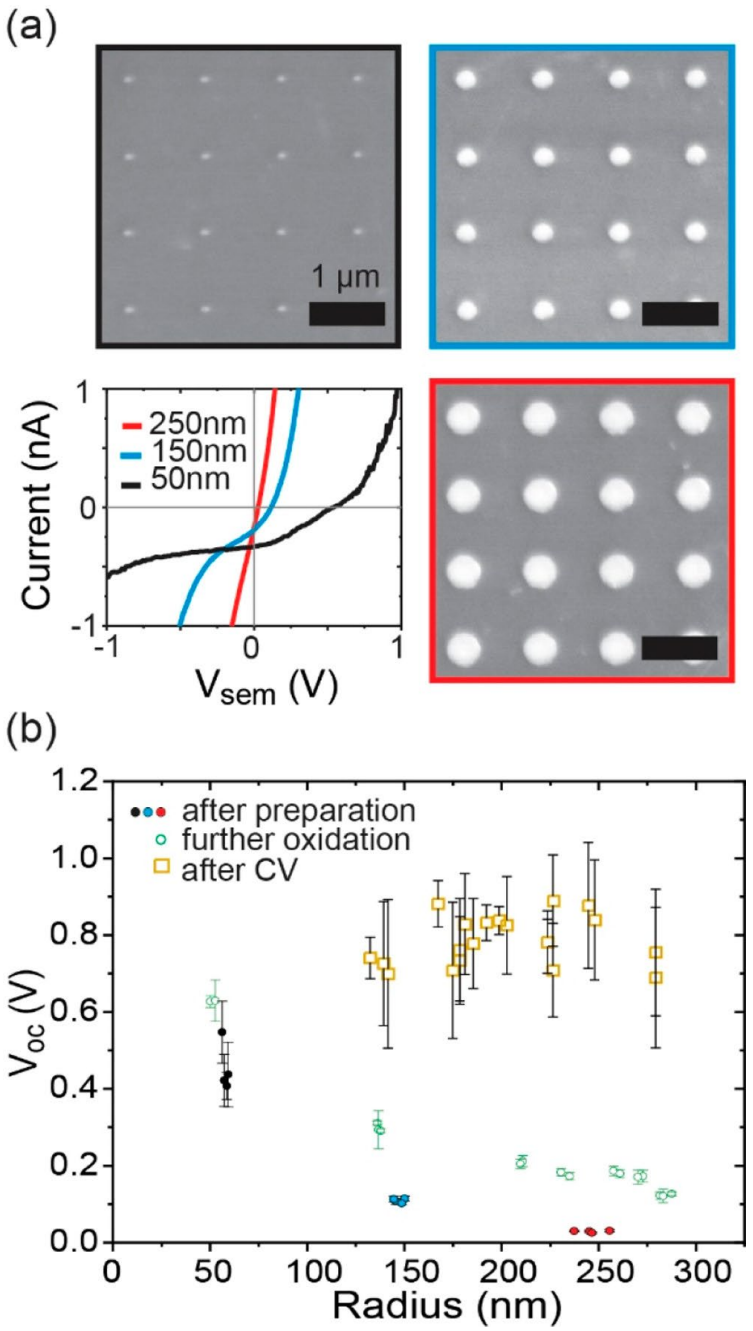

Figure B.4. Pinch-off effect at EBL Pt nanodisks. The pinch-off effect measured by C-AFM. Pt nanocontacts, 8 nm thick, deposited on H_2O_2/HCl pretreated p-InP surface by electron-beam lithography, metal evaporation, and lift-off. (a) Representative scanning-electron microscope (SEM) images (top left, top right, bottom right) color-coordinated to *J*–*V* curves of individual nanocontacts of corresponding radius from illuminated (~5 suns) conducting AFM (bottom left). (b) The V_{oc} values for Pt/p-InP individual nanocontacts illuminated by laser-light spillover around the probe cantilever extracted from *J*–*V* curves. The V_{oc} increases with decreasing nanocontact radius, in agreement with the pinch-off model. The V_{oc} data were collected from the same sample subject to 2 weeks of further oxidation in room-temperature air. Increased V_{oc} was observed for all disk radii. The yellow squares signify V_{oc}'s recorded from a unique sample after a single dark CV (−0.3 to 0.5 V vs SCE) in 1

M $HClO_4$ and 5 illuminated CV cycles (−0.3 to 0.6 V vs SCE), with one-sun equivalent illumination

The increased carrier selectivity for the EBL contacts with decreasing radius is readily explained with pinch-off theory.[18] Pt nanodisks (particles), when surrounded by a high-barrier-forming oxide, will begin to adopt the barrier of the peripheral material when their dimension is on the order of, or smaller than, the width of the depletion width in the semiconductor. The pinched-off particles' photovoltage is thus also a function of its radius (see the Supporting Information for further discussion and derivations). When the diameter of the contact is on the order of the depletion region, ∼500 nm for the In_2O_3/p-InP junction, the pinch-off effect is expected.[19] Larger Pt/InP nanocontacts (which have not been further oxidized) appear ohmic and are less electron-selective (Figure B.4). In fact, even for particles 150 nm in radius, only a small photovoltage is observed, consistent with pinch-off theory that predicts minimal effect as the contact diameter approaches 500 nm in this case. These data support the presence of a thin layer of In_2O_3 natively grown on the peripheral p-InP exposed to air following the metal lift-off procedure. Further oxidation in air and by cyclic voltammetry eliminates the pinch-off effect because the particles become undercut by the peripheral oxide (or an interfacial oxide forms by the diffusion of oxygen to the interface through the thin Pt disk) as in Figure B.3. Therefore, while the pinch-off effect substantially affects nanoscale contacts between Pt and bare p-InP, it does not appear to be of significant importance in the photochemical devices, unlike Ni/n-Si contacts where it was found to be the dominant effect controlling the interface charge-carrier selectivity.[18]

The Role of Oxide Heterojunctions

A sufficiently thick n-type oxide interlayer, such as In_2O_3, would be expected to form a heterojunction with p-InP.[17] The complex mixed oxide on the surface of p-InP contains In_2O_3 based on XPS (Figures B.1 and B.5), which has been observed by others under various preparation methods.[6, 9, 11-12, 29] On Pt junctions prepared by electrodeposition, the presence of the mixed oxide was observed directly after deposition and electrochemistry (Figure B.1). Because the electrodeposited particles in Figure B.1 are all smaller than 80 nm, the particles would be subject to the pinch-off effect as seen in Figure B.4b, although no dependence of the particles' radius on its barrier height was observed in Figure B.S8. The EBL samples, with the surface oxide removed before Pt deposition, also display an interfacial oxide after CV by TEM analysis (Figure B.5). Therefore, whether Pt is electrodeposited or deposited by physical vapor deposition (both thin-film and EBL nanocontacts), an interfacial oxide is generated after illuminated electrochemical cycling in 1 M $HClO_4$. The initially pinched-off smallest EBL Pt nanocontacts, while electron-selective, can achieve greater photovoltages by reducing the recombining hole current (j_0) *via* the formation of the surface oxide that is highly electron-conducting (thus increasing selectivity).[16, 27]

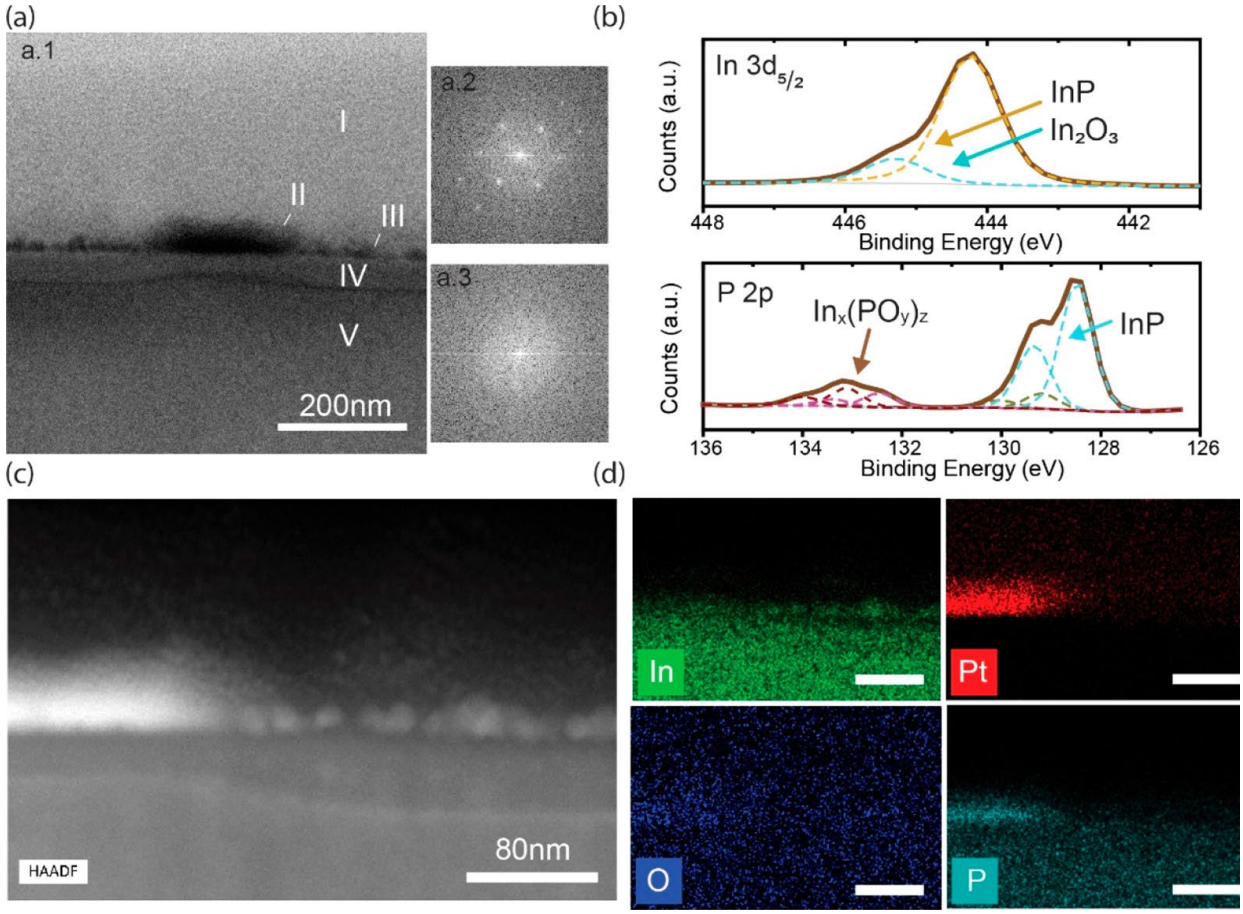

Figure B.5. Cross section of Pt|InOx|p-InP heterojunction. Structural and chemical analysis of nanocontacts following photoelectrochemistry. (a) TEM micrograph of an EBL-defined nanocontact post electrochemistry (a.1) with reduced fast Fourier transforms of region V (a.2) and region IV (a.3). (b) Of the same sample, XPS spectra of In $3d_{5/2}$ (top) and P 2p (bottom) indicate the composition of the sample's surface. (c) High-angle annular dark-field (HAADF) image with correlated EDS maps (d) of In (top left), Pt (top right), O (bottom left), and P (bottom right).

A TEM cross section of the photoelectrochemically cycled EBL-defined Pt nanodisks further demonstrates the formation of the heterojunction. Cross sections of electrochemically cycled EBL Pt nanodisks reveal an interlayer between the Pt disk and the p-InP substrate (Figure B.5a). This interlayer is observed to be amorphous by TEM analysis (Figure B.5a.3) and thinner under the Pt disk. Energy-dispersive X-ray spectroscopy (EDS) mapping (Figure B.5c,d) displays In in lower concentrations in the interlayer than in the substrate and in higher concentrations in the nodes atop the interlayer next to the Pt disks. In^{3+} may have dissolved in acidic electrolyte

creating the In-deficient layer and then been electrochemically reduced back onto the electrode's surface. These nodes are not Pt, which was found only at the Pt disk. P appears nearly homogeneous with decreased detection in the interlayer. High concentrations of P observed in the Pt disk region may be a result of higher-order scattering events emitting X-rays from the neighboring region, the interlayer, as well as possible interface "smearing" during FIB cross-sectioning. The Pt Lα peak and P Kα peak were used to identify Pt and P, respectively, to avoid misidentification of Pt by peak overlap with P Kα. However, the Pt M and P Kα peak overlap and the uncertainty in deconvolving the peaks (i.e., Pt M identified as P Kα) may contribute to the higher-than-expected apparent concentration of P in the Pt region.

The low oxygen detection was attributed to its small atomic number yielding low detection sensitivity. The higher concentration of oxygen observed in the Pt disk region was thus attributed to electron scattering into the interlayer and not Pt oxide. For more-accurate surface-chemical analysis unaffected by these possible artifacts, XPS was used to identity the composition of the amorphous surface oxides and other surface species (Figure B.5b).

Conclusion:

Pt prepared on pretreated p-InP surfaces should yield an ohmic/nonselective junction based on simple Schottky-contact models, and this is observed experimentally (Figures B.2b and B.3c). The H_2O_2/HCl pretreatment removes surface oxides (Figures B.1f,g and B.S1a,b), resulting in a more-pristine Pt/p-InP interface which was nonselective and ohmic in dry *J*–*V* curves. The substantial presence of In_2O_3 and $In_x(PO_y)_z$ by XPS, however, corresponded to rectifying *J*–*V* curves. In_2O_3 may exist in the periphery, giving rise to the pinch-off effect, which is evident from the size-dependent photovoltages found for EBL Pt/p-InP. However, no size dependence is

observed in V_{oc} after dark and light CV analysis (Figure B.4b). Further oxidation underneath the Pt by either undercutting or oxygen diffusion through the Pt film would increase the barrier (V_{oc}) and eventually diminish the pinch-off effect due to heterojunction formation.

After driving the HER, the photocurrent and V_{oc} were observed to decrease (Figure B.S10c,e). Other groups have shown similar behavior and attributed it to the removal of a surface oxide.[2, 6] Allowing the surface to rest at V_{oc} restores the photovoltage (Figure B.S10b,d), presumably due to the regrowth of the oxide under the more-positive rest potential of the system. Changes in the photovoltage might also be affected by hydrogen spill over at Pt nanoparticles.[40] Another important feature is likely the protection of n-type In_2O_3 (that forms the electrical heterojunction with p-InP) from etching by indium phosphates and polyphosphates that are more chemically stable at pH 0 leading to a layered surface-oxide structure.[6, 11, 25] After photoelectrochemical analysis, nanoscale electrical contacts on p-InP share similar electrical properties as the macroscopic thin-film sample. These experiments thus support the idea that the formation of a dynamic surface oxide, that is slowly dissolving and reforming, is responsible for generating the electron-selective catalyst contacts for precious metals on p-InP and likely also p-$Ga_xIn_{1-x}P$.

InP is one example of a highly efficient absorber used in photoelectrodes which readily form n-type surface oxides.[23, 29, 41-42] We demonstrated a mechanism by which efficient absorbers may be decorated with the desired catalysts while the absorber's surface becomes carrier-selective by natural oxidation (*i.e.*, without additional thin-film deposition steps). We showed various mechanisms control electron selectivity in different ways and situations. H_2 alloying, the previously proposed mechanism, is not primarily responsible for governing the selectivity in this system. Instead, the surface indium oxide forms an adaptive junction that becomes more electron-selective as the catalyst layer accumulates negative charge, likely due to the reduction

(increased electron doping) of the hydrated and porous In oxide.[35] Such adaptive-junction effects have not previously been considered in the context of conducting metal-oxide heterojunctions on III–V semiconductors.

These results are further broadly important for other PEC systems, like $BiVO_4$ and metal sulfides, where vacancy/defect modulation at the semiconductor surface could affect carrier selectivity by modulating the carrier concentration in that region (and hence band bending and conductivity surrounding or under a catalyst contact).[43-44] In this work, we observed the formation of an n-type oxide (likely doped with oxygen vacancies and protonic defects) increasing electron selectivity. Similarly for oxide photoelectrodes, the surface near the electrocatalyst contact could become reduced (e.g., by e^-/H^+ injection) or further oxidized (relative to the bulk, either at surface cations or at bridging or terminal oxo groups), which in turn would increase the electron and hole selectivity, respectively.

Single-particle overall-water-splitting systems, where both hydrogen- and oxygen-evolution reactions occur at spatially separated contacts on the same particle, are likely also influenced by related phenomena. These contacts, for example, might become more selective for their appropriate reaction when the surface is reduced or further oxidized either under or around the catalyst/semiconductor interface.[24, 26] The presence of H_2 alloying also might similarly increase the electron selectivity for the metal HER catalyst in single-particle photocatalysts. Single-particle systems which are decorated with nanoparticle electrocatalysts would also be subject to the pinch-off effect if a peripheral material forms a larger barrier than at the catalyst/semiconductor junction alone. Transformations in the surrounding surface (shown in this work by the growth of indium oxide) or intentional catalyst coatings employed in core–shell architectures might provide the peripheral material required for pinch-off-enhanced selectivity.

As a specific example, an increase in electron selectivity of HER catalysis during operation on single-particle systems may in fact be important to enhance carrier separation and contribute to the high external quantum efficiency observed on optimized catalyst-decorated $SrTiO_3$.[24] In sum, the mechanisms detailed in this work may provide further routes to enhance performance—or in fact already play a significant role in efficient carrier separation—on a variety of overall water splitting particles, photoanodes, and photocathodes.

Chapter 3: WIRELESS PHOTOVOLTAGE MEASUREMENTS BY AP-XPS FOR PEC SYSTEMS

Paper C: Wireless Photovoltage Using Ambient Pressure X-ray Photoelectron Spectroscopy

Aaron J. Kaufman, Ethan J. Crumlin & Shannon W. Boettcher.

This chapter contains co-authored work [unpublished], the intended journal of submission was {*ACS Energy Letters*}. Aaron J. Kaufman and Shannon W. Boettcher. conceived the experiments and led the project with support from Ethan J. Crumlin. Aaron J. Kaufman conducted all experiments at the Advanced Light Source at Lawrence Berkeley National Lab (LBL) and fabricated the devices used in this study at the University of Oregon. The AP-XPS studies within this work were collected as part of Aaron J. Kaufman's DOE-SCGSR fellowship at LBL. Aaron J. Kaufman, Ethan J. Crumlin, and Shannon W. Boettcher analyzed the data and wrote the manuscript with input from all authors.

Introduction:

Ambient Pressure x-ray Photoelectron Spectroscopy (AP-XPS) can be used to understand and map interfacial potentials at material-specific sites, while also providing rich chemical information. This capability illustrates the driving force for electrochemically active surfaces, including those in photoelectrochemical devices[1-5]. X-ray photoelectron spectroscopy (XPS) has long been employed to probe interfacial chemistry by quantifying the binding energy of photoemitted electrons, which reports on the local environment of the electron. Advancements in AP-XPS, particularly within the tender regime, facilitate measurements under operating

conditions, including interrogating the chemistry of near-surface species through a liquid electrolyte layer[1-4]. XPS spectra not only reports on the electron's local bonding environment but also its electrostatic environment. Such capabilities make AP-XPS an invaluable tool for investigating carrier dynamics with chemical specificity in environments that closely mimic real-world operating conditions.

The application of AP-XPS to photovoltage in photoelectrochemical systems has garnered increasing interest as more AP-XPS instruments come online[5-8]. Many of these instruments use a solar simulator to pump the system to be studied operando or in-situ. For bright x-ray sources commonly used in these studies, such as synchrotron radiation, the charge carrier generation rate due to the x-rays can parallel and sometimes exceed that of the solar simulator. This phenomenon, often associated with charging, can shift core-level binding energies from their expected positions when using an insufficient reference. This could result in gross misinterpretations of chemical states and band edge positions as they develop an unintended x-ray-induced photovoltage[9]. However, by this same process, the light-induced shifts in binding energy could be used to spectroscopically measure photovoltages when all electron-hole-pair generating sources are carefully considered. For instance, quasi-Fermi level splitting by x-rays and other common ionizing sources in lab-based XPS instruments has been measured in semiconducting materials and mapped across distinct layers of heterojunction solar cells[9-10]. While possibly misleading, the ability of the technique to wirelessly measure photovoltage in specific core levels underscores its utility for studying carrier separation at interfaces. Suzer et al. observed light-induced core-level shifts in GaN and Si p-n junctions using a pulsed potential method for deconvoluting the generation due to x-rays[11-12]. Additionally, AP-XPS in the dip-and-pull configuration has been used to measure core-level binding-energy shifts attributed to

electrochemical potential gradients that would otherwise be inaccessible in traditional "wired" electrical methods[1, 13-14]. Despite these solid-state developments, AP-XPS's potential for wireless photovoltage mapping, across and through complex geometries in PEC devices, has yet to be fully realized and its complications fully understood.

$$BE_{\mathrm{i}} = h\nu - \left(KE_{\mathrm{d}} + W_{\mathrm{F,d}}\right) \quad \text{(C.1.1)}$$

$$h\nu = BE_{\mathrm{i}} + W_{\mathrm{F,i}} + KE_{\mathrm{i}} \quad \text{(C.1.2)}$$

$$KE_{\mathrm{d}} = KE_{\mathrm{i}} + W_{\mathrm{F,i}} - W_{\mathrm{F,d}} \quad \text{(C.1.3)}$$

where BE_{i} is the binding energy, KE_{i} is the kinetic energy, $W_{\mathrm{F,i}}$ is the work function and $h\nu$ is the x-ray photon energy. Subscript i and d indicate position at the sample or detector.

Imagine a perfect wire connecting a Pt metal sample to the XPS's analyzer. XPS measures the kinetic energy of photoemitted electrons from the sample. This kinetic energy is linearly related to the binding energy of that electron by equation 1.2. If an electron is emitted from state S_{i} to the void, it will possess kinetic energy, KE_{i}, once ejected from the surface and it will be measured to have the kinetic energy, KE_{d}, at the detector when the Fermi level of the detector is equal to that of the sample, i.e., the sample is grounded to the analyzer. With the platinum grounded to the analyzer, you would observe the Pt4f, Pt3d, and so on at their respective positions when referenced to the Fermi level of the analyzer. Now imagine a 5 V battery is added between the Pt sample and the analyzer's ground. Because Pt is a conductive metal and undergoes no chemical change, all the electrochemical potential is electrostatic. When this voltage is applied to the sample versus the ground of the analyzer, the kinetic energy of the photoemitted electrons from the same state is changed by the applied amount. That is to say, all core levels are shifted by the

applied voltage, which is observed as a binding energy shift in the final spectra due to the principle of superposition in electrostatics. Photovoltages established at metal contacts, in the absence of chemical change, create the same apparent binding energy shifts.

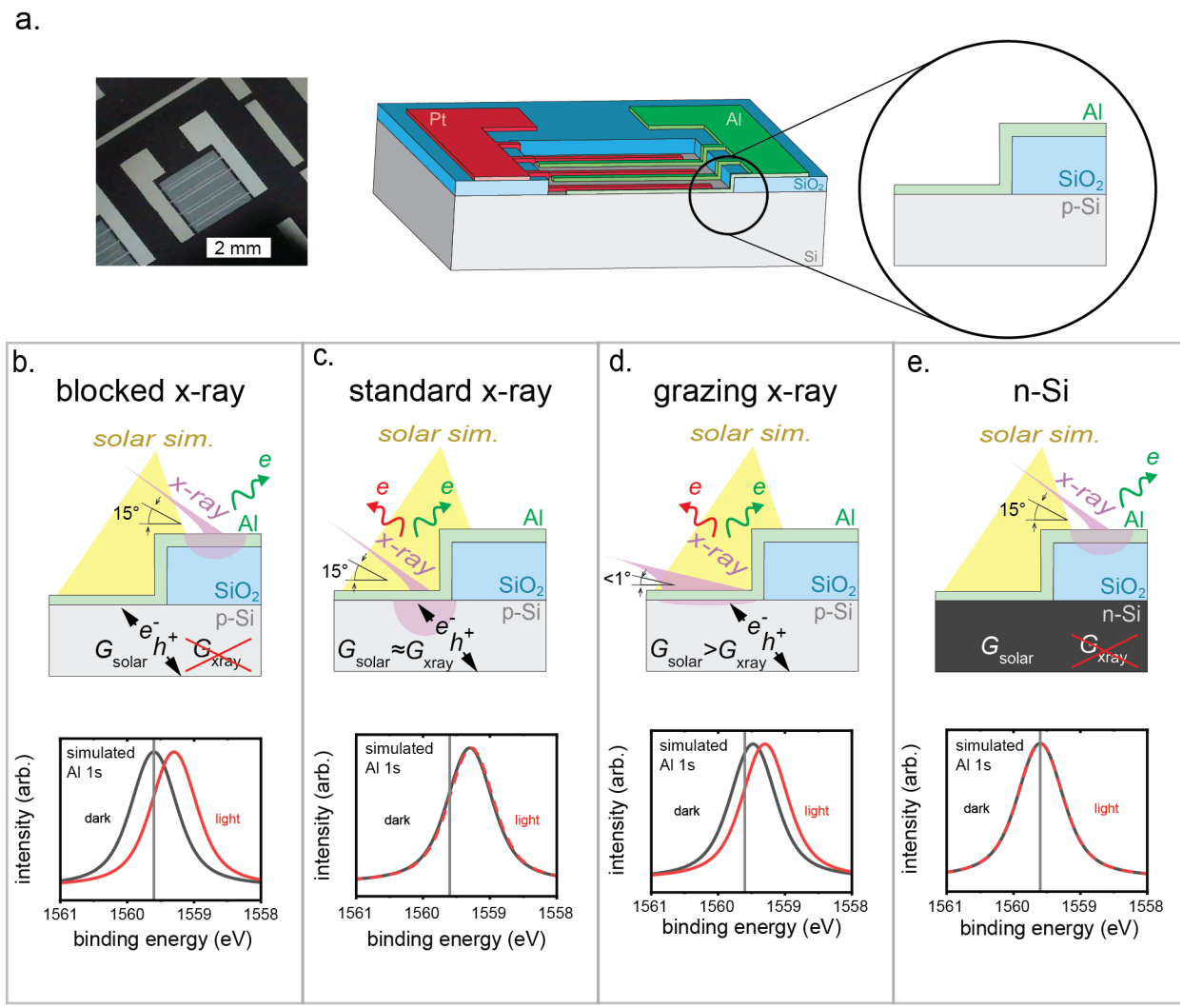

Figure C.1. Experimental configuration. An image and diagram of a single interdigitated solar cell (a) used in this study. Pannels (b-d) depict x-ray and illumination configurations used to control where x-rays interacted with the samples (indicated by the highlighted oblong hemispherical regions (x-ray = purple, solar = yellow)). Below the diagrams are simulated Al 1s under the respective conditions. Solar illumination is simulated to produce 0.3 eV shift in the Al 1s to lower binding energies. The x-ray generation rate is simulated to be equal to that of solar illumination. Grazing incidence was simulated to decrease the x-ray flux by 3 orders of magnitude.

In this study, Schottky silicon solar cells with interdigitated top contacts, seen in figure 1, were employed as a clean model system to elucidate the challenges and capabilities of AP-XPS in photovoltage studies. By leveraging AP-XPS to analyze core-level shifts in aluminum and platinum top contacts on n- and p-type silicon under various illumination conditions, this work bridges existing gaps in the literature and lays out a framework for this technique. Beyond demonstrating the technique's utility, it critically examines overlooked challenges associated with x-ray-induced artifacts and proposes actionable strategies to enhance the reliability of photoelectrochemical measurements using AP-XPS. Throughout this document, “dark” refers to the condition where x-rays are the only generation source (all viewports covered, the solar simulator light is blocked, without charge neutralization, or ion impingement). If the x-ray flux is turned off, it will be explicitly mentioned. These findings are expected to inform future studies and establish best practices for addressing interfacial phenomena.

Experimental:

Schottky contact solar cells were fabricated using p-type (B, 10 Ω•cm) and n-type (P, 100 Ω•cm) silicon substrates with aluminum (Al) and platinum (Pt) contacts (University Wafer). This simplified design incorporated one ohmic and one Schottky contact, facilitating targeted investigation of contact-dependent carrier dynamics. Direct laser writing (MicroTech LaserWriter LW405C) photolithography (Resist: AZ1512) defined the contact geometry, followed by etching with 6:1 buffered oxide etch (BOE) to achieve precise patterning. To enhance junction quality and minimize surface recombination, a thin passivation oxide layer was thermally grown prior to metallization (90min at 450C in 100% O2). Metals were deposited via physical vapor deposition (PVD) techniques, including e-beam (Pt) and resistive heating (Al), ensuring uniform coverage of 40nm films. These Schottky cells are intended as model systems,

paralleling photoelectrochemical devices, to systematically explore the potential and limitations of wireless photovoltage measurements using AP-XPS.

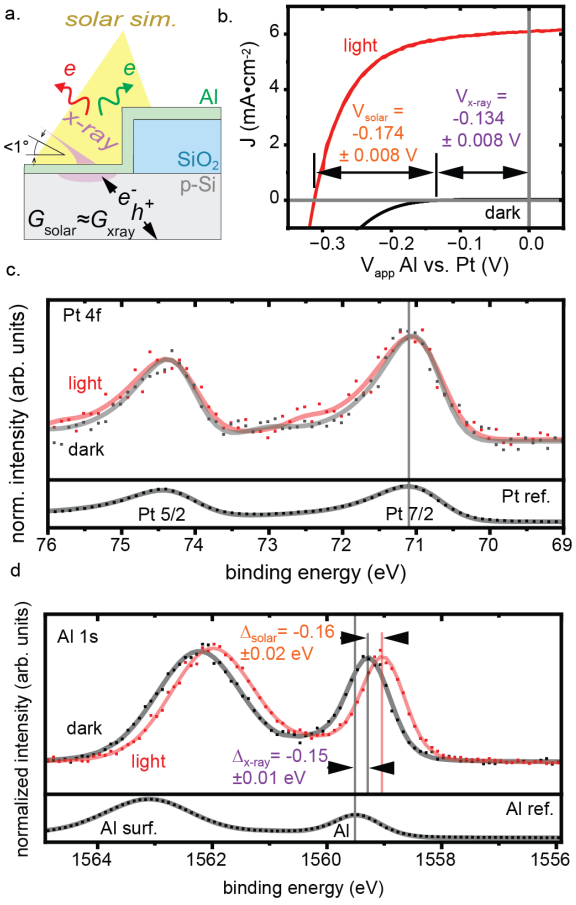

Figure C.2. Simultaneous measurement of heterogenous potential. A diagram for p-type silicon with platinum and aluminum interdigitated contacts under illumination with x-ray probe at a grazing incidence around 1 degree to decrease x-ray flux. In-Situ J/V curves taken before XPS spectra were taken with x-rays on in the dark and under approximately 0.1 sun illumination. The "dark" curve displays x-ray induced photocurrent and voltage, minimized by the grazing incidence. XPS spectra of Al 1s and Pt 4f spectra collected in the dark (with x-rays on) and under 0.1 sun illumination in vacuum.

APXPS Measurements:

BL 9.3.1 was used for AP-XPS measurements at 4 keV. Using 9.3.1's feedthroughs, electrical connections were established to the samples' contact pads and ohmic back contact using silver paste to minimize contact resistance and ensure stable electrical grounding inside the sample chamber. APXPS spectra were acquired for Pt (4f) and Al (1s) core levels under dark and illuminated conditions (0.1 sun, as measured by a UV005 photodiode, though sample orientation and shadowing may cause deviations from this value). Grazing-incidence x-rays were employed to reduce x-ray-induced photocurrent, ensuring that the observed core-level shifts predominantly reflected photogenerated carrier effects (G_{solar}). This was done by rotating the theta of the sample manipulator to below 1-degree grazing angle, (between 0.5 and 0.1, see diagram in supplemental). Controlling x-ray intensity was critical to decouple light- and x-ray-induced phenomena without an applied bias, providing reliable photovoltage measurements albeit, the collection time for the same signal-to-noise ratio scales linearly with the x-ray intensity. The simplified system highlights the direct effects of APXPS measurement conditions and their parallels to operational PEC systems.

Results and Discussion:

Wireless photovoltage measurements using AP-XPS hinge on the ability to detect illumination-induced shifts in core-level binding energies. However, challenges associated with x-ray-induced artifacts pose significant risks to data interpretation. This section elucidates the utility of AP-XPS, highlights key pitfalls, and outlines strategies to address them. The Schottky cells used serve as a simplified analogue for PEC systems, enabling controlled exploration of these challenges by making direct comparisons to in-situ current/voltage (J/V) characterization. Simultaneous measurements of electron (Al) and hole (Pt) selective top contacts on p-type Si with the ohmic back contact of Si grounded to the analyzer were done under grazing incidence to

decrease x-ray flux and ensure that the carrier generation rate from x-rays ($G_{x\text{-}ray}$) was negligible compared to that from solar illumination (G_{solar}). Figure 2b shows dark and light in-situ J/V curves recorded before XPS measurements with x-rays on to assess the impact of illumination on the electrically measured photovoltage (labeled V_{solar} and $V_{x\text{-}ray}$). Systematic alternation of light and dark cycles, collected in triplicate, enabled the isolation of solar illumination effects from x-ray-induced carrier generation. Figure 2 illustrates the electrical Voc (V_{solar}=-0.174 V) measured by in-situ J/V vs its dark reference agrees with the Al 1s binding energy shift (Δ_{solar}=-0.16) to lower binding energies as it accumulates electrons. Furthermore, the overall light induced shift in the Al 1s spectra relative to the internal aluminum reference illustrates the total photovoltage induced shifts from both the solar simulator and the x-rays, also in agreement with the in-situ JV characterization. In contrast, the Pt 4f spectra remains unaffected by the x-rays and solar simulator during light/dark cycles and aligns with its internal reference because it forms an ohmic contact. A small high binding energy shoulder peak emerges under light bias due to $Pt(OH)_2$ formed as the Pt contact collects holes. By using a clean model system, this approach provides insights to carrier selective contacts under solar illumination without external bias, crucial for the interpretation of later PEC systems.

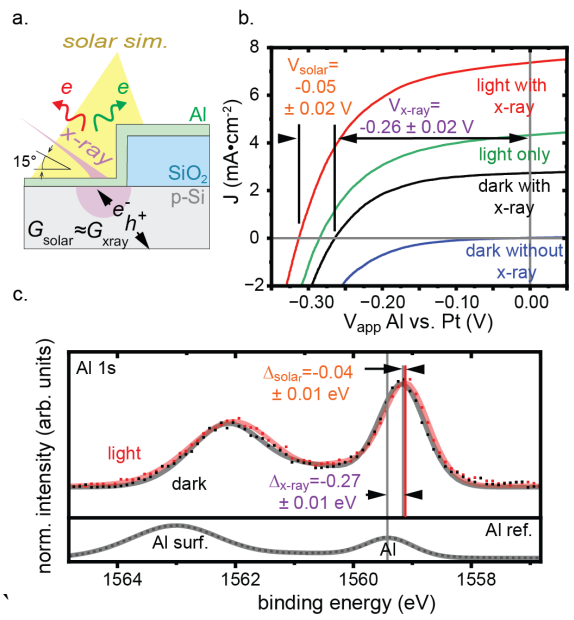

Figure C.3. Influence of x-ray probe. A diagram for p-type silicon under regular incidence, 15 degrees. In-Situ J/V curves taken before xps spectra were taken with combinations of generation sources. The "x-ray only" curve displays x-rays induced photocurrent and voltage, Almost equal to that of the solar simulator. (c) As a result only small changes are seen in the XPS spectra of Al 1s collected in the dark (with x-rays) and under 0.1 sun illumination in vacuum.

When the $G_{x\text{-}ray}$ is not attenuated or decreased and on the order of or larger than G_{solar}, the effects of light/dark cycling may not be noticed. Increasing the x-ray angle from extreme grazing (<1 degree) to the standard 15 degrees for ALS BL 9.3.1, the solar simulator induced shifts in the Al 1s spectra were small in comparison to Figure C.2. This is caused by the logarithmic relationship between photovoltage and photocurrent.

$$V_{oc} = 0.0595 \times \log\left(\frac{J_{ph}}{J_0} + 1\right) \qquad \text{(C.2.1)}$$

An increase in photocurrent by 1 order of magnitude will increase the photovoltage by 59.5 mV, as seen in equation 2.1. In figure 3, the Al 1s spectra illustrates approximately a 40mV shift to lower binding energies with solar illumination, which agrees with in-situ J/V characterization and expected for a photocurrent increase of 4.4 mA/cm^2 (*light with x-ray – dark with x-ray*). These curves alone illustrate the influence of x-rays on this type of measurement and underscore the need to manage the $G_{x\text{-}ray}$ for successful implementation of this technique.

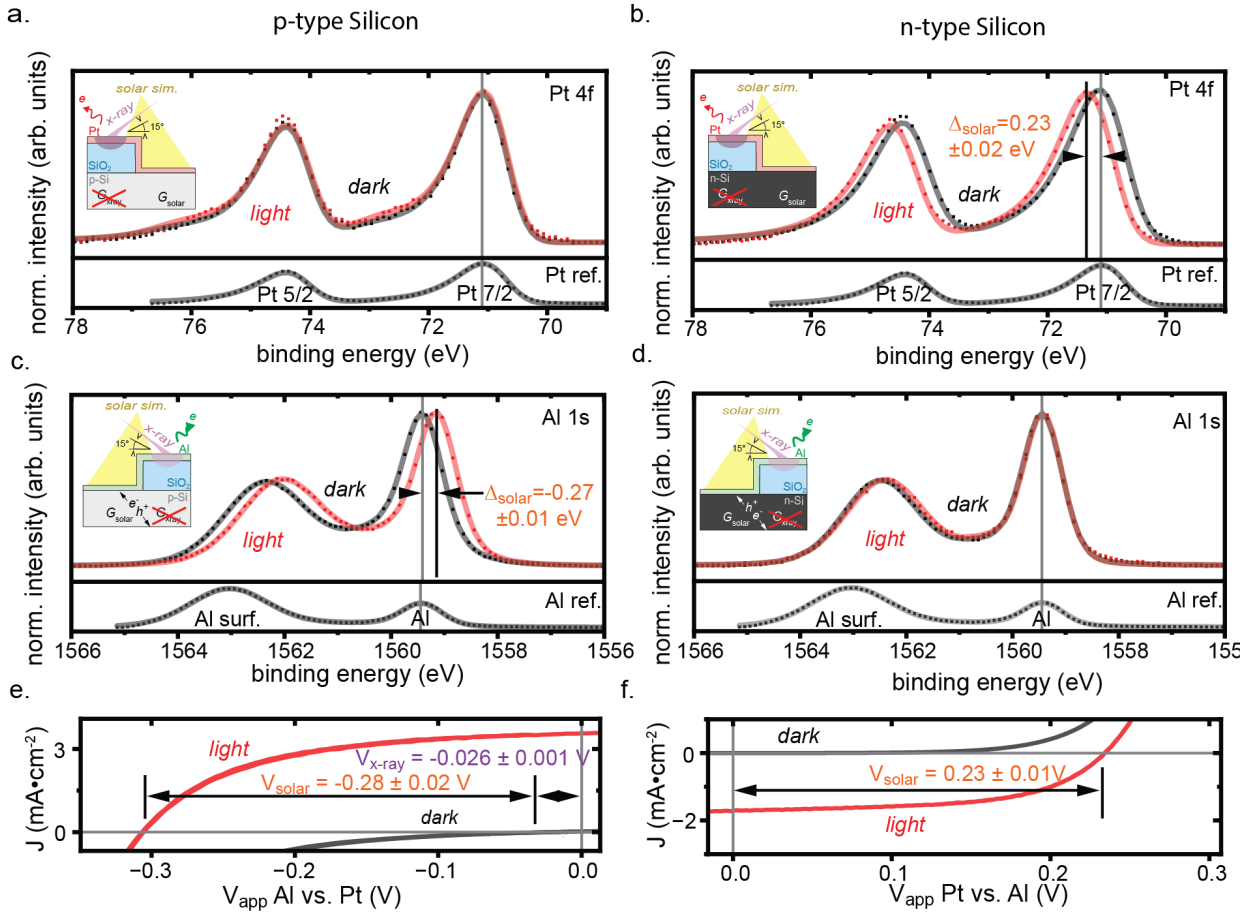

Figure C.4. Electron and hole selective contacts with blocked x-rays. A diagram for p-type (left (a.)) n-type (right(b)) silicon with platinum and aluminum interdigitated contacts under illumination with x-ray probe. XPS spectra of Al 1s and Pt 4f spectra collected in the dark (with x-rays on) and under 0.1 sun illumination in vacuum, spectra were acquired from the contact pads where the generation due to x-rays was blocked (c-f). In-Situ J/V curves taken before xps spectra were taken with x-rays on in the dark and under 0.1 sun illumination. Panel (g) shows a small amount of x-ray induced voltage in the dark, therefore the light vs dark open circuit voltage was used for appropriate comparison.

Let's remove $G_{x\text{-}ray}$ entirely by attenuating it through a metal contact and the thick AR SiO2 coating. Here, most of the induced shift in core levels should be due to the influence of the solar simulator. For this class of experiments, the standard incidence of 15 degrees was used, however each metal contact was independently measured by moving the x-ray probe to the contact bar. For p-type silicon, Pt served as an ohmic contact, while Al acted as a barrier contact. Illumination induced quasi-Fermi level splitting, reflected as a -0.27 V shift in the Al 1s binding energy, consistent with in-situ electrical measurements of open-circuit voltage (Voc). The Pt 4f

spectra remained static under illumination, corroborating its role as a non-selective ohmic contact.

Conversely, for n-type silicon, Al functioned as the ohmic contact, while Pt formed the Schottky barrier. Solar illumination caused a 0.23 V shift in Pt 4f to higher binding energy, while the Al 1s spectra remained unaffected. A Schottky barrier on n-type Silicon will selectively collect holes, shifting its core levels to higher binding energies, like electrochemical oxidation. Complementary behaviors validate the role of metal core-level shifts as robust indicators of interfacial charge dynamics and highlight the versatility of AP-XPS in characterizing diverse contact configurations. These measurements, derived from the model system, are directly applicable to understanding PEC device behavior and the direction electron and hole selective contacts should shift under solar illumination.

The dual role of x-rays as both a probe and a source of carrier generation introduces challenges in isolating photogenerated effects. Inadequate management of x-ray flux can result in significant artifacts, such as spurious quasi-Fermi level splitting measurements or artificially enhanced binding energy shifts. These issues are particularly severe in systems with low photoconversion efficiencies (proportionately low G_{solar}), where x-ray contributions may dominate. Additionally, alignment of the sample with respect to the x-ray source can exacerbate these artifacts by introducing non-uniform carrier generation, as the x-ray flux at the sample varies with incidence angle, complicating data interpretation. Overlooking these factors risks misattributing x-ray-induced phenomena to genuine photo-induced effects, undermining the validity of the measurements. As illustrated in Figure C.5 however, wireless XPS photovoltage mapping is possible by understanding of influence x-ray generated free carriers.

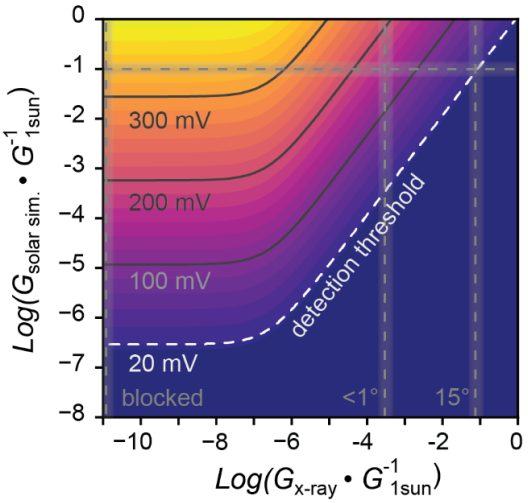

Figure C.5. Detection criteria. The theoretical shift due to the solar simulator alone as a function of the generation rate from solar simulator and probing x-rays relative to that produced under an ideal 1 sun illumination. The vertical dashed lines indicate the x-ray generation rates observed in this study and the horizontal dashed line is the generation rate of the solar simulator. The voltage detection threshold, labeled detection threshold in the diagram, is an approximation for high resolution synchrotron based XPS systems.

To address the challenges induced by the x-ray probe, this study employed grazing-incidence x-rays to minimize the carrier generation rate from the x-ray beam. Systematic modulation of x-ray intensity and precise sample alignment ensured that x-ray-induced artifacts were effectively suppressed, summarized in figure 5. Furthermore, alternating light and dark cycles allowed for direct comparison of solar illumination effects against baseline x-ray contributions, enhancing the reliability of the results without the need for an additional reference. The clean Schottky cell model system underscores how these mitigation strategies can be effectively applied to PEC devices.

Conclusion:

This study establishes the feasibility and utility of wireless photovoltage measurements via chemically specific AP-XPS analysis of interfacial phenomena while addressing critical challenges associated with x-ray-induced artifacts. By correlating core-level shifts with in-situ electrical data and implementing robust mitigation strategies, this work sets a benchmark for reliable photovoltage studies in PEC systems. The Schottky solar cells used serve as a clean model system to highlight parallels to PEC devices, identifying challenges and capabilities of AP-XPS. Future research will extend these methodologies to complex heterojunctions, tandem structures, and particulate photoelectrochemical systems, broadening the applicability of AP-XPS in advanced energy science. These advancements promise to deepen our understanding of interfacial charge dynamics and drive innovations in device design.

Paper D: APXPS Photovoltage Measurement Through a Heterojunction on Pt|InOx|p-InP Photocathode

Aaron J. Kaufman, Ethan J. Crumlin & Shannon W. Boettcher.

This chapter contains co-authored work [unpublished], the intended journal of submission was {*ACS Applied Materials & Interfaces (Letters Section)*}. Aaron J. Kaufman and Shannon W. Boettcher. conceived the experiments and led the project with support from Ethan J. Crumlin. Aaron J. Kaufman conducted all experiments at the Advanced Light Source at Lawrence Berkeley National Lab (LBL) and fabricated the devices used in this study at the University of Oregon. The AP-XPS studies within this work were collected as part of Aaron J. Kaufman's DOE-SCGSR fellowship at LBL. Aaron J. Kaufman, Ethan J. Crumlin, and Shannon W. Boettcher analyzed the data and wrote the manuscript with input from all authors.

Introduction:

Photovoltaic and photoelectrochemical (PEC) systems rely on efficient charge separation at semiconductor-liquid and semiconductor-metal interfaces to drive energy conversion processes. Understanding interfacial charge dynamics in these heterostructures is critical for optimizing performance. Ambient pressure X-ray photoelectron spectroscopy (APXPS) provides an in-situ method to probe the electronic structure and photovoltage effects in these systems, particularly under realistic operating conditions such as exposure to water vapor.

In this work, we use APXPS at to measure photovoltage generation in a Pt|InOx|p-InP photocathode under water vapor conditions. We analyze the binding energy shifts of core-level

peaks from InP, InOx, and Pt at a photon energy of 4keV at extreme grazing incidence (<0.5°) to extract photovoltage behavior through the heterojunction. Our findings provide direct insights into band bending and charge separation at the Pt|InOx|p-InP interface and the role each material specific component plays.

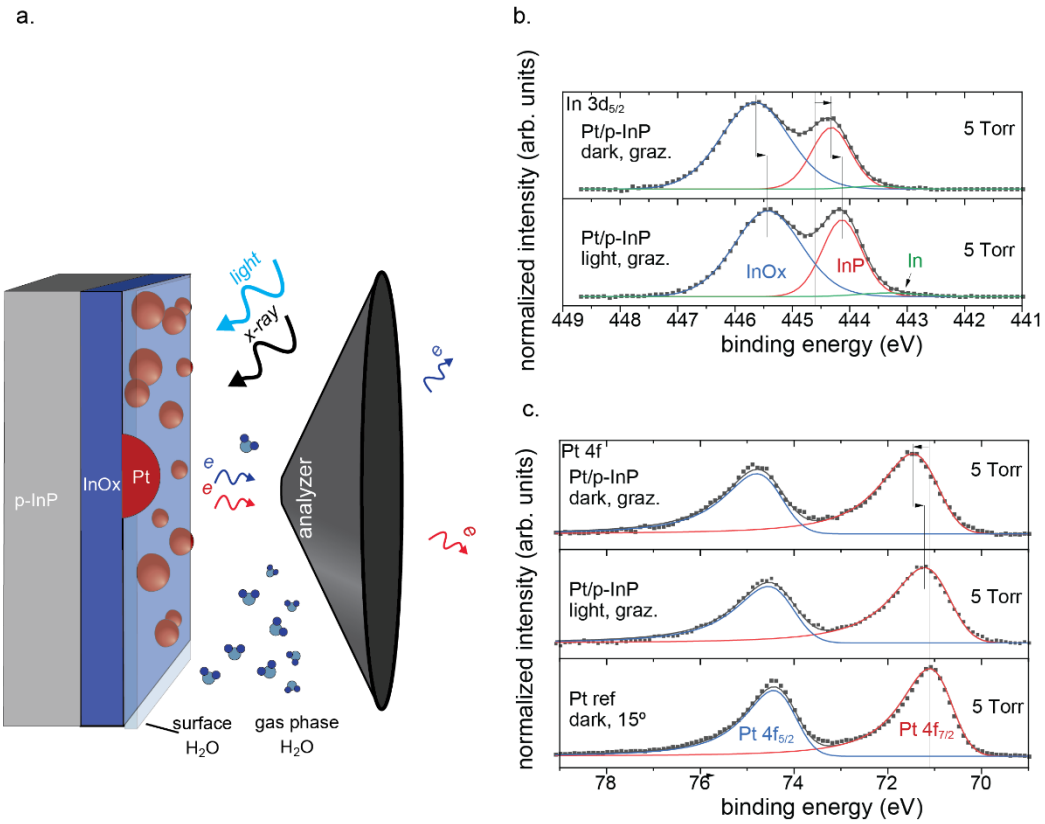

Figure D.1. Experimental configuration and AP-XPS spectra. (a.) experimental scheme for measuring wireless photovoltage in the Pt/p-InP photocathode system in vapor phase water with surface adsorbed water. Panels b and c depict data collected at 5 Torr water vapor with and without illumination for In $3d_{5/2}$ (b) and Pt 4f (c).

Results and Discussion:

Photovoltage Induced Core-Level Shifts: Figure 1b displays the In $3d_{5/2}$ core-level spectrum under dark and illuminated conditions. The binding energy shifts observed in these spectra indicate band bending at the semiconductor surface, suggesting photovoltage generation at the p-InP|InOx interface where light assisted electrodeposited Pt nanoparticles only make up a small amount. Under illumination, a shift toward lower binding energy is observed, consistent with an

upward shift of the conduction band energy in the p-type semiconductor due to charge separation and local accumulation of electrons.

Similarly, Figure 1c shows the Pt 4f core-level spectrum. An equal shift in the Pt $4f_{7/2}$ and $4f_{5/2}$ peaks suggests a change in the local electrostatic environment by the p-InP|InOx interface, confirming that photovoltage extends through the InOx layer and into the Pt nanoparticles. The initial shift observed in the Pt 4f spectra is attributed to the locally hole selective barrier formed at its interface with the degenerate n-InOx. Largely, the shift observed at the InOx|Pt junction is not affected by solar simulated light and only the x-ray probe. We propose that this "backwards photovoltage" is solely influenced by x-rays, as long-lived solar-generated carriers in InOx are not expected. Furthermore, if InOx is ionically permeable, the barrier is likely to be screened. These shifts corroborate charge redistribution across the heterojunction where the p-InP|InOx established the total photovoltage observed in PEC measurements.

Simulated Band Bending and Experimental Validation: To further interpret the photovoltage-induced shifts, we performed COMSOL simulations of the conduction band profile in the Pt|InOx|p-InP system (Figure 2). Figure 2(a) presents the conduction band edge (E_C) of p-InP and InOx under dark and illuminated conditions, along with the Pt Fermi level ($E_{f,m}$). The simulated band bending shows a depletion region in the p-InP with charge extracted from the n-InOx layer with significant photovoltage formation under illumination while InOx|Pt is modeled to be ohmic. As seen in Figure 1c, the InOx|Pt interface is expected to be more complex but remains unaffected by solar-generated carriers.

Figure 2(b) compares the calculated electrostatic potential (difference between illuminated and dark conduction bands) with the experimentally observed core-level shifts. The experimental binding energy shifts align well with the simulated potential, confirming that APXPS accurately

captures the interfacial photovoltage response. Notably, the open-circle data point at -5 nm represents a true "dark" measurement extrapolated to zero X-ray intensity to isolate the true photovoltage effect from X-ray-induced generated carriers[1].

Implications for Photocathode Performance: The observed photovoltage shifts provide key insights into charge dynamics at the Pt|InOx|p-InP interface. The magnitude of the photovoltage suggests efficient band alignment, promoting charge extraction from the p-InP substrate to the Pt overlayer with the presence of electron selective interlayer, n-InOx. These findings have implications for designing optimized photocathodes for PEC applications, where oxides grow on the native semiconductor under operation, crucial for carrier selective transport and photovoltage generation[2-5].

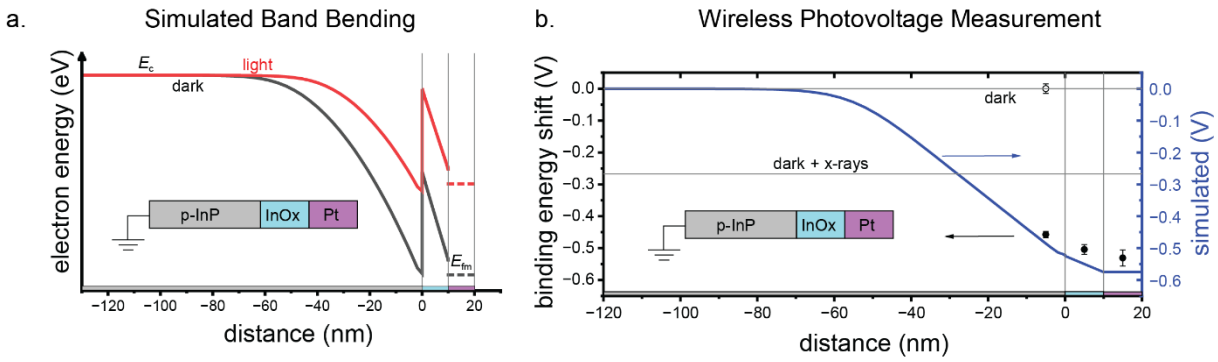

Figure D.2. Simulation and experimental wireless photovoltage. Pt|InOx|p-InP heterojunction photovoltage, simulation and wireless measurement. a. Conduction band edge (E_c) of p-type Indium Phosphide (gray) and Indium Oxide (blue) and the Fermi level of Pt (E_{fm}) simulated with COMSOL in the dark and under illumination. (b.) electrostatic potential calculated from panel a. by subtracting the light from the dark conduction band edges and Pt Fermi level superimposed with the measured core level binding energy shifts in from InP, InOx and Pt under the same light intensity. The dark InP (open circle at -5 nm) measurement was calculated from extrapolation to zero x-ray intensity from a attenuated x-ray probe study using increasing thickness of Al foil to neglect its influence.

Conclusion:

Using APXPS, we have directly measured photovoltage formation across a Pt|InOx|p-InP photocathode under water vapor conditions. Core-level binding energy shifts in InP, InOx, and Pt

confirm band bending and charge redistribution across the heterojunction under illumination. COMSOL simulations support these observations, demonstrating the consistency between experimental and theoretical electrostatic potential profiles. These results highlight the potential of APXPS as a powerful tool for probing photovoltage effects in complex heterojunctions, aiding in the design of and fundamental understanding in charge transport in advanced photoelectrochemical systems.

Chapter 4: CHARGE SELECTIVE MECHANISMS IN OVERALL WATER SPLITTING SYSTEMS

Paper E: Cooperatively Adaptive Junctions on Single Crystal $SrTiO_3$

Aaron J. Kaufman, Ethan J. Crumlin & Shannon W. Boettcher.

This chapter contains co-authored work [unpublished], the intended journal of submission was {*Nature Materials*}. Aaron J. Kaufman and Shannon W. Boettcher. conceived the experiments and led the project with support from Ethan J. Crumlin. Aaron J. Kaufman conducted all experiments at the University of Oregon and the Advanced Light Source at Lawrence Berkeley National Lab (LBL) and fabricated the samples used in this study at the University of Oregon. The AP-XPS studies within this work were collected as part of Aaron J. Kaufman's DOE-SCGSR fellowship at LBL. Aaron J. Kaufman, Ethan J. Crumlin, and Shannon W. Boettcher analyzed the data and wrote the manuscript with input from all authors.

Introduction:

$SrTiO_3$ (STO) has been widely studied as a model photocatalyst for overall water splitting due to its ability to achieve exceptionally high external quantum efficiencies, with reported values reaching 96% under ultraviolet (UV) light irradiation.[1] However, despite its impressive performance under UV light, STO exhibits poor solar-to-hydrogen conversion efficiencies,

primarily due to its wide bandgap of 3.2 eV, which limits its absorption to a small fraction of the solar spectrum. This fundamental limitation has driven extensive research efforts into bandgap engineering, such as cation substitution, aimed at improving solar absorption.[2-5] While these approaches have achieved modest gains in absorption, they have yet to translate into substantial improvements in overall solar-to-hydrogen conversion efficiency.

Beyond STO, other perovskite-like oxides with narrower bandgaps, such as $BiVO_4$, Fe_2O_3, and TaON, have been explored for photocatalytic applications.[6-8] These materials exhibit improved solar absorption compared to STO due to their smaller bandgaps, but their solar-to-hydrogen conversion efficiencies remain low. For instance, $BiVO_4$ has shown promise for water oxidation under visible light, and Fe_2O_3 is known for its stability and visible light absorption capabilities.[6,8] Similarly, TaON demonstrates significant photocatalytic activity due to its narrower bandgap and stability.[7] However, the inability of these systems to achieve high efficiency underscores a critical gap in understanding the mechanisms that govern charge separation and carrier selectivity, key parameters for efficient solar-driven water splitting. We propose that the formation of effective carrier-selective contacts is the primary bottleneck in these systems, and addressing this challenge is crucial for advancing photocatalyst performance.

The influence of crystal facet termination on photocatalytic activity has garnered significant attention, with several studies reporting enhanced hydrogen evolution reaction (HER) and oxygen evolution reaction (OER) rates when specific facets are exposed. For instance, positioning of HER and OER catalysts on their respective carrier-selective facets significantly improved water-splitting efficiency.[1,7,9,10] At the nanoscale, tungsten nanoprobe measurements

by Huang et al. (2017) showed asymmetry in exposed crystal facets on nanoparticles, while macroscopic single-crystal studies of STO revealed similar asymmetries.[11-13] However, we argue that while such asymmetries are measurable, they are insufficient to drive overall water splitting in isolation. Given that each single crystal shares the same bulk, the voltage developed across opposing crystal facets (selective contacts) must exceed 1.23 V- the minimum free energy required to split water. Thus, facet asymmetry alone cannot fully account for the observed performance in these photocatalytic systems. As seen on STO with mixed redox reactions, the kinetics of electron transfer at the semiconductor (sem) | electrocatalyst (cat) interface are governed by factors beyond the idealized photoelectrode equations, beyond the Lewis and Gerischer models. Experimental observations suggest that interfacial charge transfer is not solely dictated by equilibrium energy alignment but also by dynamic kinetic constraints[14,15].

$$J_{jxn,buried} = k_p\left(p'_s - p_s\right) - k_n(n'_s - n_s) \tag{1.1}$$

$$J_{jxn,adapt} = k_p\left(p'_s - p_s e^{\frac{qV_{cat}}{kT}}\right) - k_n\left(n'_s - n_s e^{\frac{-qV_{cat}}{kT}}\right) \tag{1.2}$$

$$J_{cat} = j_{0,cat}\left(e^{\frac{qV_{cat}}{2kT}} - e^{\frac{-qV_{cat}}{2kT}}\right) \tag{1.3}$$

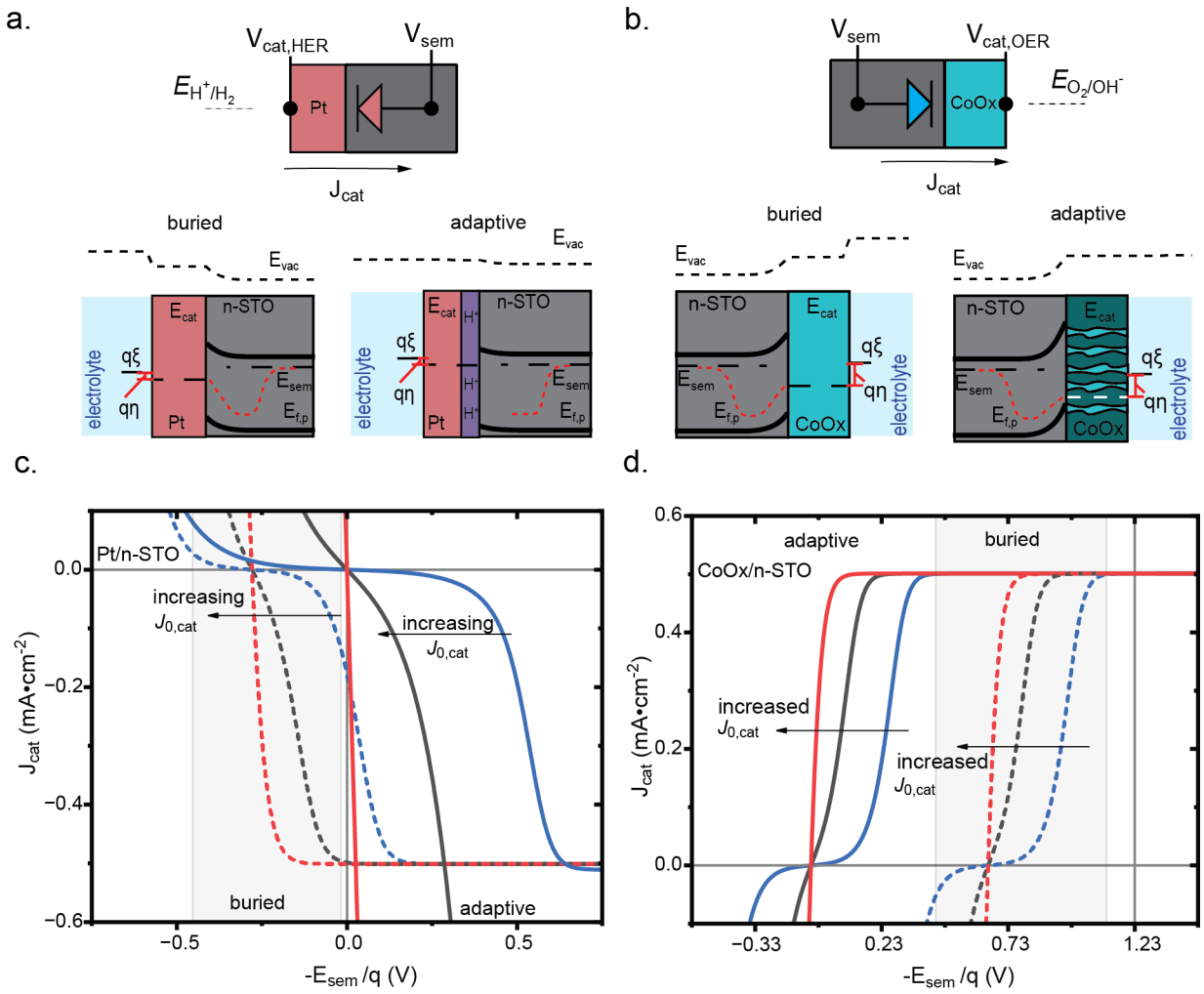

Figure E.1. Adaptive junctions
Platinum (a) and Cobalt oxide|n-STO (b) buried and adaptive junctions schematic and band bending diagram. Figures c and d display currents from equations 1.1, 1.2 and 1.3 solved numerically by SciPy's fsolve function. This function uses Newton's method and a scaled gradient approach to iteratively solve systems of nonlinear equations, requiring an initial guess and assuming local differentiability. The photocurrent was fixed to produce 0.5 mA•cm^{-2} , near what is experimentally measured for STO. $J_{0,cat}$ was swept from 1 to 1E-3 mA•cm^{-2} to highlight fast and slow kinetic reactions.

To generate any significant photovoltage, carrier-selective junctions are essential for separating charge carriers and enabling effective redox reactions. In a conventional two-metal contact system, the maximum achievable open-circuit voltage (Voc) is determined by the work function difference between the two metals[16]. During operation, where the catalysts electrochemical potential changes to drive a reaction, so can its chemistry by either undergoing its own redox event or by ion insertion. As the catalyst's chemistry changes while driving

electrochemistry, so does the sem | cat junction properties in some systems. Adaptive junctions, where the chemical potential and barrier height can dynamically adjust to match the redox potentials, play a pivotal role in improving photocatalytic performance. These adaptive carrier-selective junctions could provide the additional driving force needed to achieve efficient overall water splitting. Figure 1 compares the adaptive and non-adaptive junctions using equation 1.1 and 1.2. Simplified Butler-Volmer kinetics, 1.3, was used to measure the fraction of the potential dropped in the electrolyte[17]. The adaptive junction generated larger photovoltages at the OER catalyst compared to its buried junction and a decreased photovoltage at the HER catalyst as its behaves more like an ohmic contact. They offer ion permeable catalysts, improved electrode kinetics and free energy produced and can likely be extended two electrocatalyst systems, like those employed in STO overall water splitting particles.

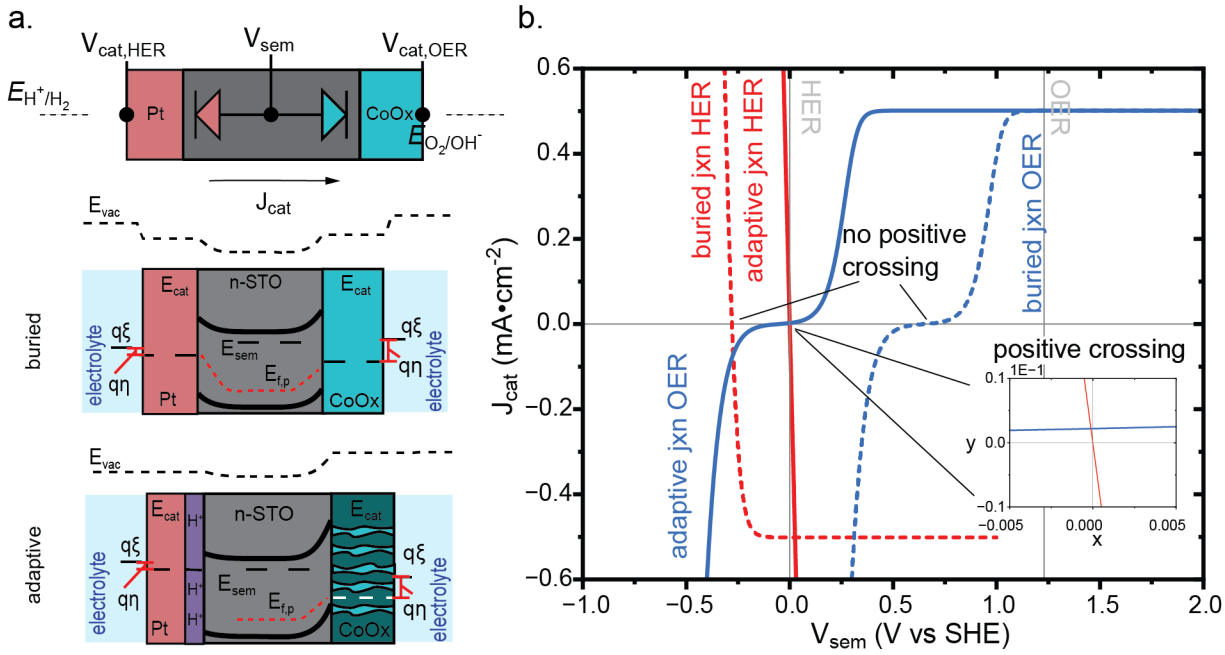

Figure E.2. Dual adaptive junctions
Platinum and Cobalt oxide|n-STO (a) buried and adaptive junctions schematic and band bending diagrams. Figures b display currents from equations 1.1 and 1.2 solved numerically by SciPy's fsolve function for each junction individually. In figure (b), the results of buried and adaptive junctions using $J_{0,cat}$ =1 and 1e-3 mA•cm^{-2} for Pt and CoOx driving the HER and OER respectively. There must exist a shared current density (J_{HER} and J_{OER} must cross) for this system to theoretically drive water splitting[11]. Buried junctions were not observed to develop enough free energy to drive water splitting nor does alternating combinations of buried and adaptive junctions. However, the dual adaptive junctions in this idealized simulation, (at the

thermodynamic limit with a symmetric charge transfer coefficient) with modest effective barrier heights of (-0.4 and -1.9 V) is observed to theoretically drive overall water splitting.

Together with the asymmetry in crystal facets, we propose that two adaptive junctions loaded on their desired carrier selective facets act to cooperative adapt, minimizing the kenetic overpotential and enabling photovoltages large enough to drive overall water splitting. The simulated data presented in figure 2 compares the performance of complimentary buried junctions and an adaptive junctions. The non-adaptive buried system shows a limited Voc constrained by the static work function difference of the metal contacts, resulting in the inability to for that system to sustain OWS. In contrast, the adaptive junction demonstrates a dynamic increase in Voc as the electrocatalysts adjust their work functions, driving enhanced charge separation enabling OWS. The cooperation of the two adaptive junctions atop respective charge selective crystal facets offers a possible explanation for how small asymmetries in photovoltage at specific crystal facets can initiate photovoltages large enough to drive overall water splitting.

AP-XPS measurement of cooperative adaptive junction

In this study, we revisit STO as a nearly ideal model system to explore the role of carrier-selective contacts in photocatalysis. By employing single-crystal planar electrodes, we aim to directly examine the interplay between crystal facet termination and adaptive electrocatalyst behavior. As a precursor to our results, Wagner and Somorjai (1980) demonstrated that overall water splitting on single crystal STO <111> and was highly sensitive to surface composition, OH concentration specifically[18,19]. The reduced single crystal surface demonstrated heterogeneous carrier selectivity across an otherwise homogeneous surface. We began by revisiting the Wagner

system but this time with chemically trackable HER and OER sites, Pt and CoOx respectively, much like a planar analog to the overall water splitting particles. Similar to the Rh|n-STO|CoOx particle system, the Pt|n-STO|CoOx system also facilitates overall water splitting[9,20,21]. However, the work function difference between Pt and CoOx is expected to be less than 1.23 V, primarily due to platinum's inherently high work function. A singular accepted value of CoOx's work function is challenging to define, as it strongly depends on its composition and oxidation state. This raises questions about whether additional factors, such as interfacial energetics or reaction kinetics, contribute to sustaining the water-splitting process in this system.

Tracking material specific potentials across heterogenous surfaces is difficult with standard electrochemical techniques, particularly when complementary half reaction occur across the same surface, like in STO <111>[18]. Ambient pressure x-ray photoelectron spectroscopy (APXPS) can provide rich chemical and electrostatic surface information, even through a thin electrolyte layer[22-25]. We use commercially available epi-polished $SrTiO_3$ single crystals reduced in H_2 atmosphere at 1000°C for 6 hours to form oxygen vacancies and increase conductivity. Our results suggest that while facet asymmetry provides an initial driving force for charge separation, the cooperative adaptation of electrocatalysts significantly enhances selectivity and drives the overall water-splitting reaction. These findings provide critical insights into the mechanisms underlying photocatalytic performance and offer a framework for improving the efficiency of solar-to-hydrogen conversion in STO and other perovskite-like systems.

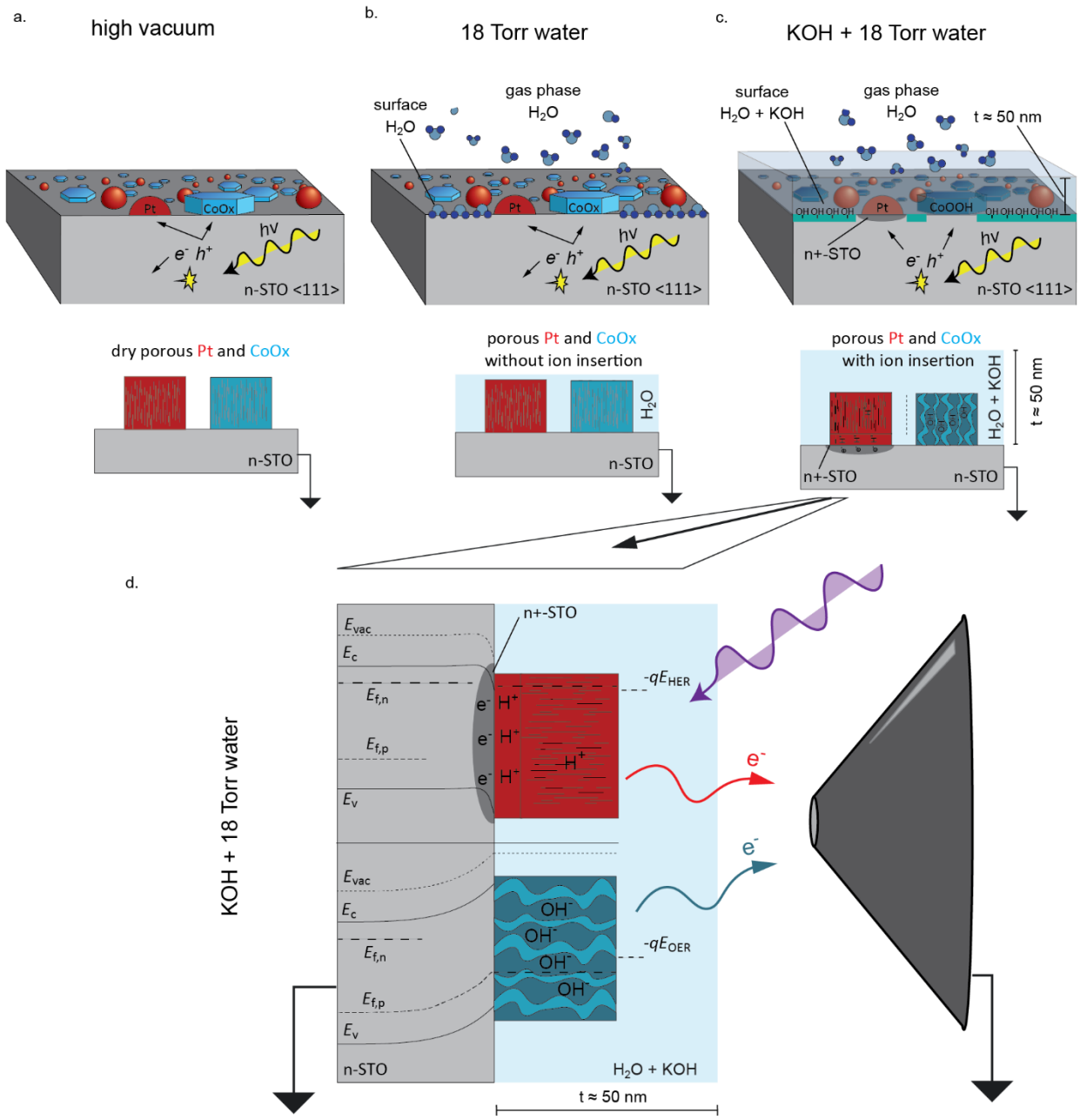

Figure E.3. Deliquescent AP-XPS

(a-c) depict three conditions of sample environments studied in this work. In each case, Pt was photodeposited onto reduced STO from 20 µl of 1 mM H2PtCl6 followed by CoOx from 5.41 mM Co(II) (NO3)2 for 5 min each under 1 sun illumination in 100% humidity and subsequently vigorously rinsed. For the KOH deliquescent sample, 20uL 0.0133 M KOH was dried at 80°C for 10 min to form a solid crust just before entering the AP-XPS chamber. Panel d depicts a band diagram hypothesis for cooperatively adaptive Pt/n-STO and CoOx/n-STO junctions measured in AP-XPS.

The APXPS measurements conducted at BL 9.3.1 reveal significant changes in the electronic states of STO systems under different environmental conditions. For reduced STO <111> single crystals, like those used in Wagner's study where electron and hole selective sites were observed to be produced on the same single crystal surface by the generation of stoichiometric Hydrogen and Oxygen. Catalyzed samples were observed to produce electron and hole selective contacts at the Pt and CoOx respectively under similar conditions. Electrocatalysts were sequentially deposited under 100% humidity, Pt then CoOx from H_2PtCl_6 and $CoCl_2$ respectively. To observe light induced effects, all viewports were covered except for the solar simulator's quartz viewport and extreme grazing incidence (<1°) was used to decrease the x-ray flux (the solar simulator's light output measured at the sample was measured to be approximately 0.1 sun or 10 mW/cm^2). Between each atmospheric condition a fresh location was chosen, each comparative spectra had a similar amount of beam exposure.

In high vacuum, with a relatively free surface, no significant light induced changes were observed in the Pt 4f and Co 2p 3/2 spectra. All Pt features (metallic and two oxides) were observed be electrostatically shifted oxidatively to higher binding energies compared to their expected positions, indicating selective hole collection from x-ray generated carriers. Cobalt oxide was observed to have strong Co^{2+} character, with the presence of a large Co^{2+} satellite feature.

Next, the sample was exposed to 18 Torr water vapor, saturated at room temperature. Still, with surface adsorbed water, no dominant changes were observed in the Pt 4f and Co 2p spectra between light and dark cycling of the solar simulator. The Co^{2+} satellite feature was observed to decrease in intensity compared to the high vacuum atmosphere, likely due to increased coordination of CoOx with surface adsorbed water. The platinum spectra contained

proportionally more metallic Pt^0. All Pt features were still observed to be hole collecting. This agrees with Wagner's study where water splitting was not observed in water vapor alone, nor in neutral salts.

However, under 18 Torr water vapor with KOH, notable transitions occur. The Pt 4f spectra were observed to lose their highest oxidation peak and the Pt^0 peak shifted to lower binding energies under solar simulator illumination. This shift indicates that Pt now functions as an electron collector. The metallic Pt 4f peak under solar simulated light aligns with both the accepted literature value and the internal metal reference. This suggests a reduction in the electron barrier, making the contact more ohmic. These shifts were observed to be reproducible under further dark/light cycling. In contrast, the Co 2p spectra show a transition to an oxidized state, shifting from Co^{2+} to Co^{3+}, as evidenced by the attenuation of the strong Co^{2+} satellite feature at between 785-787 eV. This indicates that Co serves as a hole collector under these conditions. These observations demonstrate that the combination of KOH and water vapor enhances charge separation and carrier selectivity, critical for improving photocatalytic performance in adaptive junction systems.

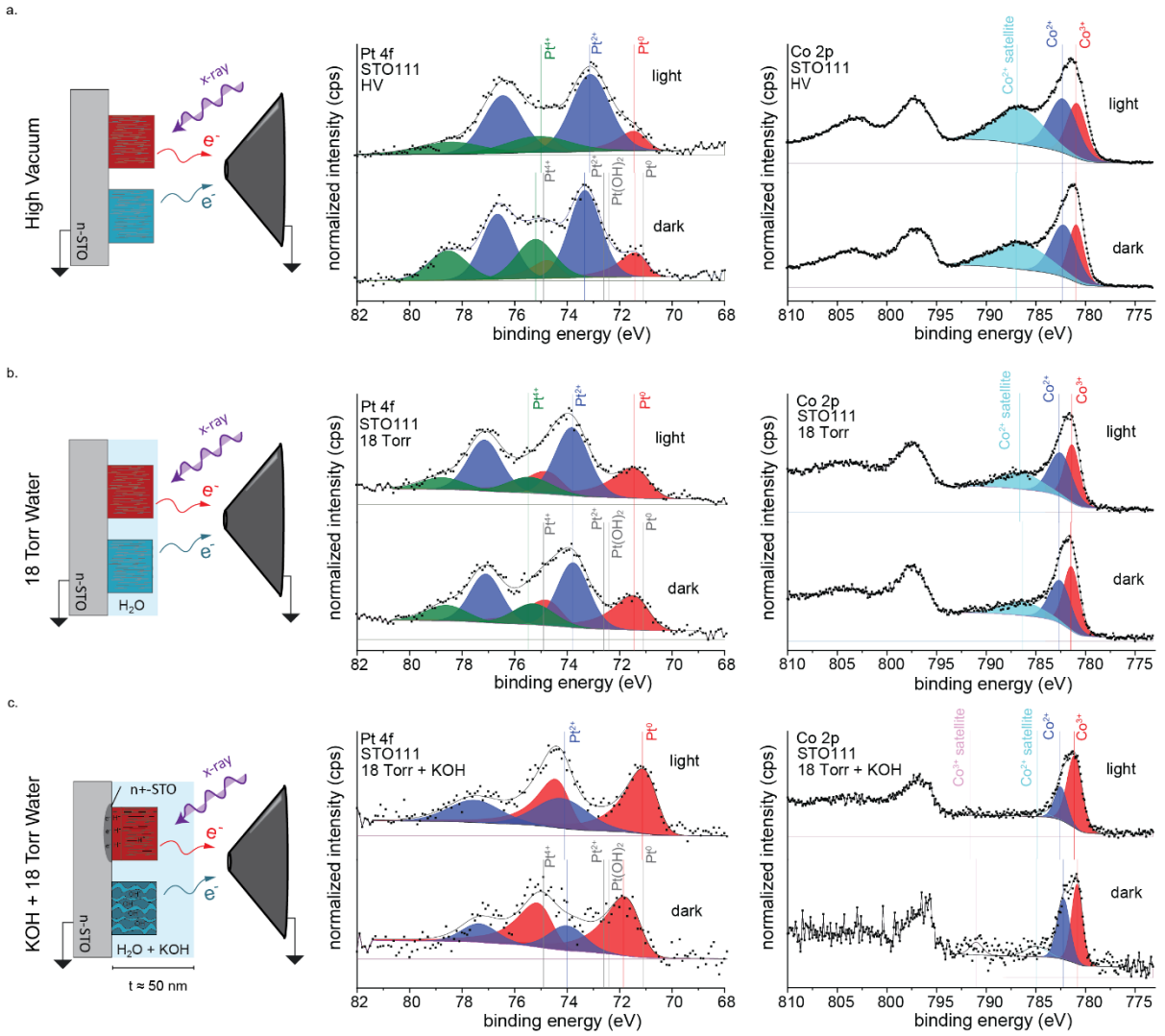

Figure E.4. Adaptive junctions by AP-XPS
the three diagrams at the left of the figure indicate the three environmental conditions APXPS conditions, high vacuum, 18 Torr water vapor, and 20uL 0.0133 M deliquescent KOH in 18 Torr water vapor collected at 4keV photon energy under grazing incidence (<1°). Internal gold foil was used as an energy reference for all respective atmospheric conditions. The analyzer was shorted to the Au refence and the ohmic back contact of the STO samples established with GaInEu enclosed in vacuum compatible epoxy.

Both electrocatalysts appear to be adaptive under illumination and in KOH by AP-XPS. Platinum, normally forming a large Schottky barrier contact with n-type STO was observed to collect electrons while $Co(OH)_2$ was observed to collect holes and become CoOOH with KOH surface electrolyte under dark/light cycles. First, both electrocatalyst were photodeposited onto

single crystals without external electrical biasing. Instead, upon illumination, Pt was reduced and CoOx deposited from their salt precursors, indicating inherent electron and hole selective sites on predicted homogeneous single crystal surfaces. This likely proceeded at reconstructed surface defect sites, commonly observed at all dominant single crystal terminations of STO.[26-29] Second, Pt^0 shifting to lower binding energies in the Pt 4f spectra was only observed coupled with an oxidation of the $Co(OH)_2$ to CoOOH. We hypothesize that local, within the diffusion length, electron and hole adaptive contacts enable the collection and conversion of the electrocatalyst to a highly active phase for their intended redox reactions, in a positive feedback loop.

Dual working electrode single crystals with dominant facet terminations <100> and <110>

We then ask if Co and Pt can cooperatively adapt on the dominant crystal facets exposed on STO nanoparticles, <100> and <110>. Cobalt has been observed to chemically change from Co(OH)2 to CoOOH as it drives OER[30-32]. Furthermore, CoOx is anticipated to form an adaptive junction as it both undergoes a its own redox chemistry near the OER and is ionically porous[31,32]. This agrees with the chemical change observed in CoOx in Figure 4. Platinum however, while likely porous and amorphous at the scales used in particulate photocatalysts, is not expected to undergo its own bulk redox chemistry as it drives the HER. Although Pt hydroxide formation is expected at the electrode surface during HER and has been observed in small amounts via operando AP-XPS in KOH[33], we argue that the dramatic shift to lower binding energies seen in Figure 4 is not indicative of Pt-H formation but rather signifies the Pt/n-STO interface becoming ohmic. This is largely because the drastic chemical transformation required for substantial Pt-H conversion, as identified by AP-XPS, has not been observed in more controlled studies of Pt undergoing the HER in KOH[33]. Instead, we hypothesize that as ionically porous Pt is driven

towards the HER, protons diffuse to n-STO/Pt interface, lowering its usually large barrier height enabling photovoltage for overall water splitting. To verify that both CoOx and Pt are cooperatively adaptive on n-STO—where the CoOx|n-STO junction increases its barrier height (increasing hole selectivity) and the Pt|n-STO junction decreases its barrier height (increasing electron conductivity)—the dual working electrode technique was used to investigate each cat|sem interface.

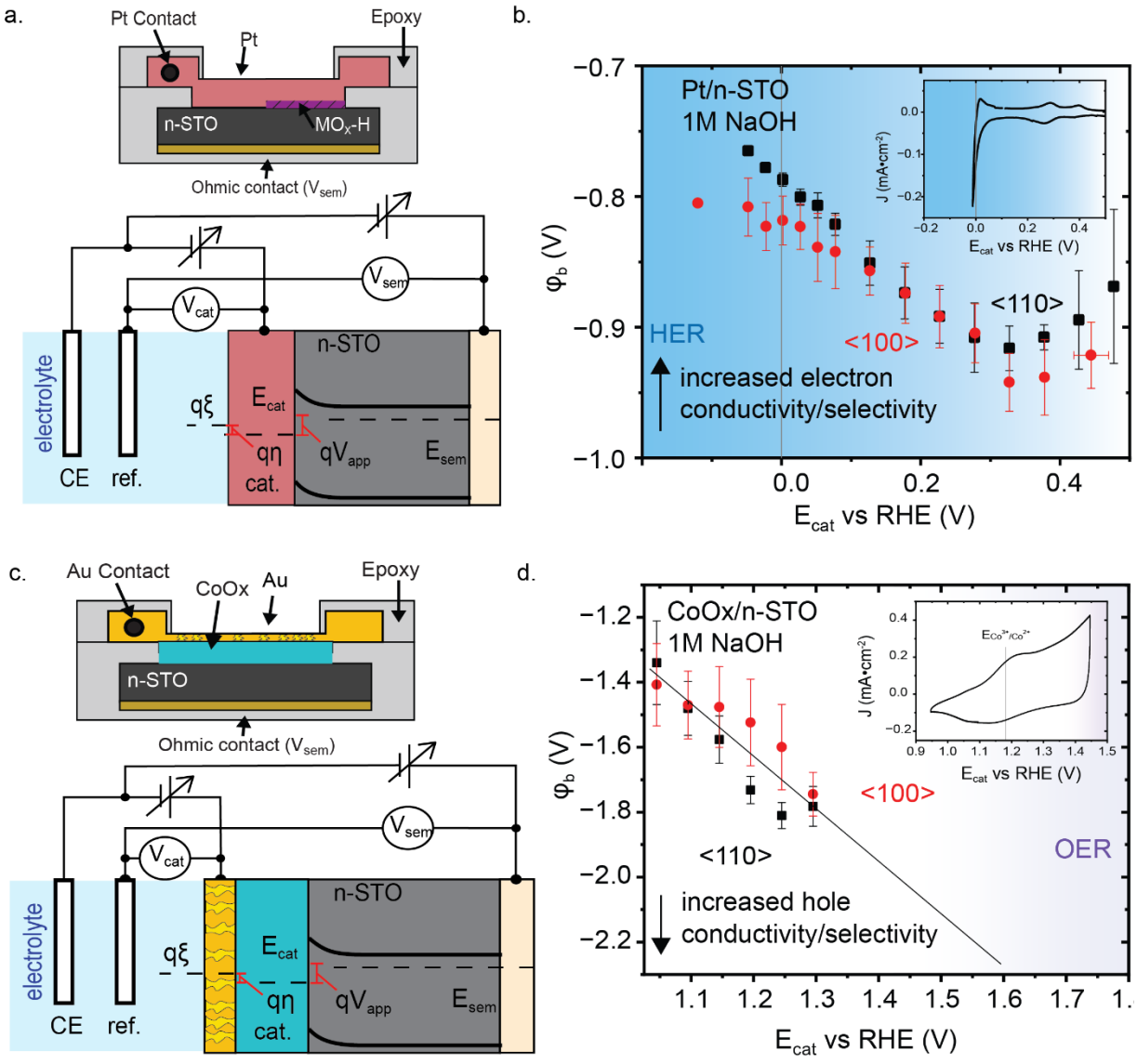

Figure E.5. Adaptive junctions by DWE. a and c display the device geometry used for the dual working electrode for the Pt/nSTO and CoOx/nSTO junctions respectively for both <100> (red circles) and <110> (black squares) terminated single crystals. Both configurations used a GaIn-Eutectic ohmic back contact and were encased in epoxy to expose only the polished single crystal surface. Panel b shows the electron barrier height from the Pt/nSTO junctions and panel d shows the electron barrier height from the CoOx/nSTO junctions calculated from the JV curves where the total current through the junction was measured vs the potential across that junction (Vapp) at various catalyst potentials (Ecat) in 1M NaOH. Ecat Potentials beyond 1.3 V in the CoOx/nSTO experiments caused the thin film to break up.In both panels b and d, the data points are the average of 3 separate experiments and the error bars indicate the standard error.

Both platinum and cobalt oxides deposited on single crystals of STO were observed to be adaptive regardless of crystal facet orientation. In 1 M NaOH, the magnitude of the large barrier height for Pt on n-STO was observed to decrease at the potential for under-potential-deposition (UPD) of hydrogen, as seen in the Pt cyclic voltammogram in Figure 5b (inset). As Pt drives the HER its junction properties become more ohmic and less selective to holes. This is likely due to the accumulation of protons at the Pt | n-STO interface, where hydrogen dissociates on Pt, generating protons that migrate to the metal oxide surface, further supported by apparent barrier height lowering at the Pt | n-STO interface in H_2 gas (Figure S7). This process alters the free-charge density in the semiconductor, forming the basis for solid-state hydrogen gas sensors. Proton migration occurs because protons are unstable in bulk Pt due to their low solubility, whereas the oxide provides favorable binding sites through defect interactions and surface states[34-36]. These observations highlight how proton accumulation and interfacial charge modulation influence the junction properties of Pt on n-STO, a behavior that extends to cobalt oxides (CoO_x), where similar adaptive junction behavior increases the junction's selectivity to holes.

Cobalt oxide was also observed to be adaptive by the DWE as it's potential approaches that required for the OER. We observed the opposite effect on CoOx as in Pt where the

magnitude of the CoOx|n-STO barrier height increased, becoming more selective to holes as it collected holes (figure 5c). The ion permeable CoOx enables OH^- to migrate throughout itself, compensating for the positively charged holes. This effectively modifies the chemical potential of the CoOx as the electrostatic component is screened and establishes a new effective and larger barrier height as compared to its dense equivalent, a buried junction.

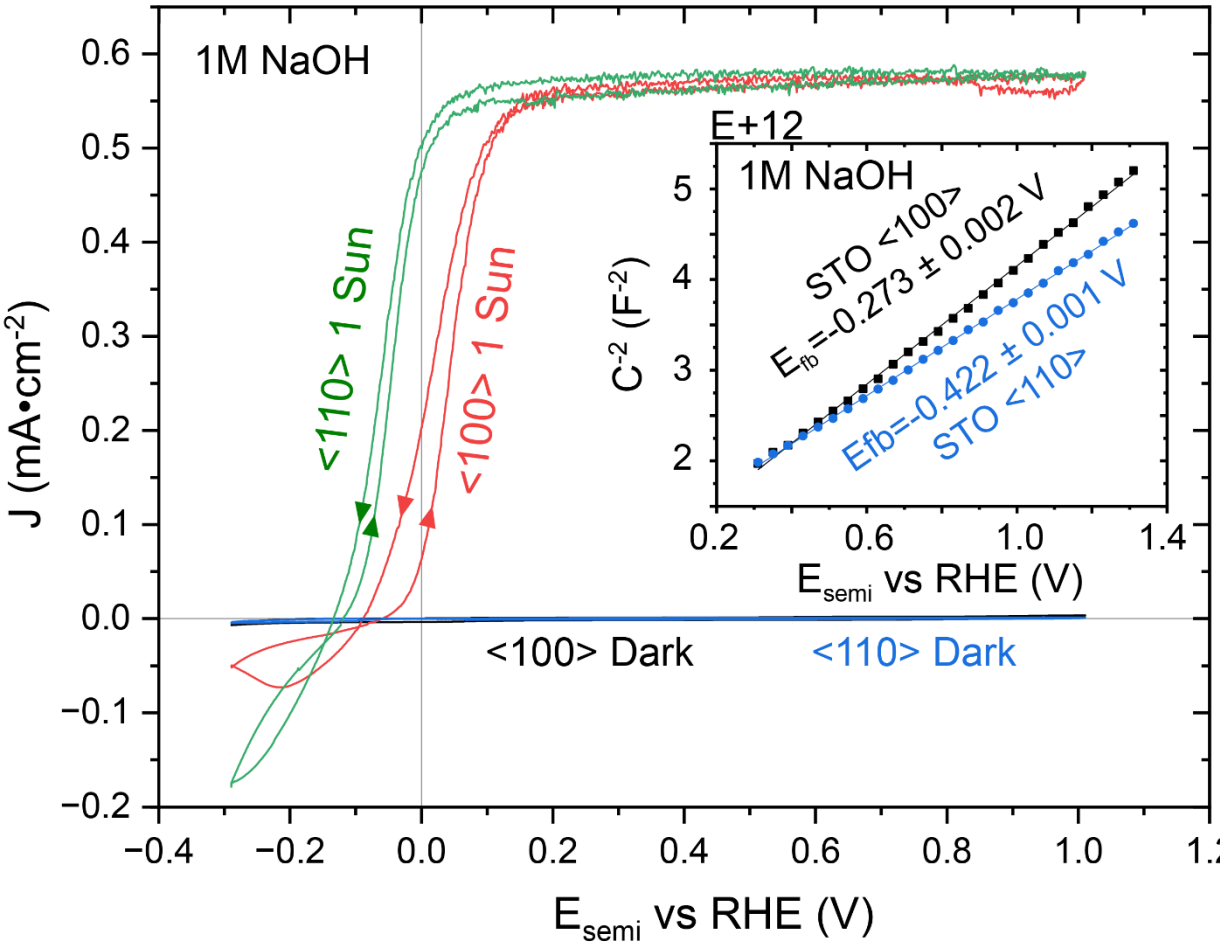

Figure E.6. Crysal facet comparison. Dark and light CV's of n-STO in 1M NaOH. Inset shows Mott-Schottky analysis in the same electrolyte under dark conditions. Both results highlight the small crystal facet termination asymmetry however, not large enough alone to drive overall water splitting.

Crysal facet asymmetry

So what role does the crystal facet termination play in charge selectivity? Numerous research efforts have shown there to be differences between the dominant <100> and <110> facets[1,9,11,13,37]. Slightly larger flat band potentials have been observed at the <110> terminated facet over the <100> facet with a hexacyanoferrate ferri/ferro-cyanide redox couple[13]. Illuminated cyclic voltammetry also indicates slightly larger photovoltages as photoanodes, also seen within this work[13], but to complete OWS the system must drive both half reactions, the HER and the OER. At the nanoparticle scale, catalyst loading on specific crystal facets, Pt on the <100> and CoOx on <110> has correlated to improved quantum efficiency[1,9,10,38]. Even prior to the OWS activity studies, appropriate electrocatalysts are selectively deposited onto specific crystal facets by photodeposition, often called photolabeling[9,38]. When shorted together, bare electrodes of termination <100> and <110> did not display photocurrent corresponding to OWS (Figure E.S8). Photocurrent was observed only before and shortly after the onset of nitrogen sparging, likely due to oxygen reduction at the cathode (<100>) and hydroxide oxidation at the anode (<110>), indicating a regenerative electrochemical process rather than a photosynthetic one.[39] Crystal facet asymmetry alone cannot account for the overall photovoltage and free energy required to drive water splitting. We argue that the crystal facet asymmetry plays a crucial role in setting up a positive feedback loop. Electron selective electrocatalysts are reduced preferentially where there is a higher concentration of photogenerated electrons, conversely cobalt oxide is oxidized at locations of high hole concentrations. This is the essence the cooperatively adaptive junctions, which only further increase their selectivity for their respective carrier as they drive the HER or the OER.

Uncatalyzed single crystals of n-STO used throughout this work exhibit small differences in their open-circuit voltage (OCV) and flat band potentials in 1M NaOH. Although they are the

same underlying material, Figure E.6 shows that n-STO <110> has a more negative OCV and flat band potential than <100> in 1M NaOH. To minimize variations in dopant density, these commercially purchased, cut, and epi-polished single crystals were reduced together in the same batch. The Mott-Schottky plot in the inset of Figure E.6 confirms that both crystals have similar dopant densities based on their nearly identical slopes. Since the OCV of these single-crystal electrodes differs by only ~100 mV, shorting them together would not generate sufficient potential to drive overall water splitting solely due to facet asymmetry, seen in Figure S8.

Nanoscale junction properties

The Schottky barrier heights of Pt nanoparticles deposited via electron beam lithography (EBL) and electrodeposition (eDep) on $SrTiO_3$ (STO) were analyzed to investigate nanoscale interfacial behavior. On STO <100>, EBL-deposited Pt exhibited lower barrier heights on average compared to electrodeposited Pt, which may be attributed to differences in particle morphology and footprint. EBL tends to produce more delocalized Pt structures with larger contact areas, reducing sensitivity to local variations in the underlying crystal, like surface defects. This suggests that the electronic properties of EBL-patterned contacts are largely dictated by the Pt itself rather than substrate inhomogeneities, this agrees with macroscopic barrier heights from thin films measured by the DWE technique in figure E.5b. In contrast, electrodeposited Pt nanoparticles on both n-STO <100> and <110> were highly localized, preferentially forming at kinetically favorable defect sites. This localization enhances interactions with underlying electronic states, leading to variations in barrier heights across different measurement locations.

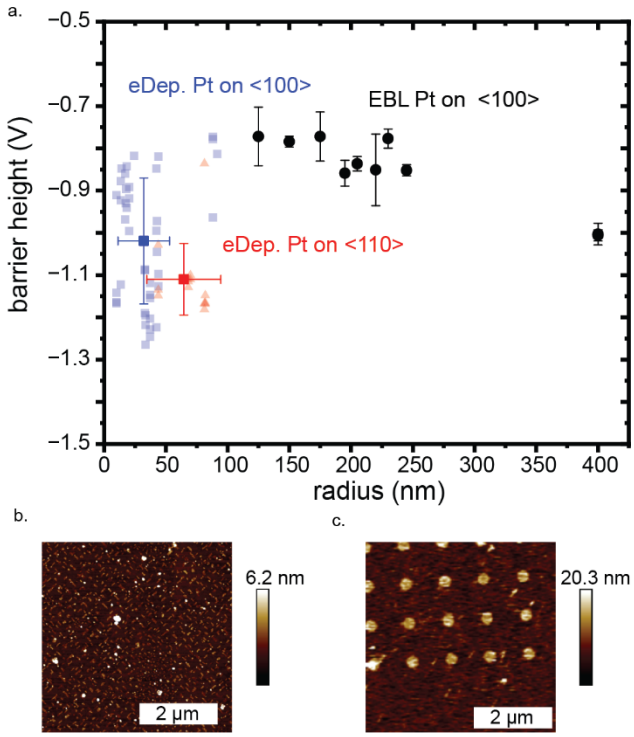

Figure E.7. Conductive AFM Pt/n-STO barrier heights. Schottky barrier heights calculated from c-AFM measured Pt nanoparticles deposited by electron beam lithography on STO <100> (black circles) and deposited by electrodeposition from dilute H2PtCl6 on STO <100> (faded blue squares) and STO <110> (faded red triangles). The solid blue square and solid red square indicate the mean barrier height for electrodeposited Pt nanoparticles on STO <100> and STO <110> respectively. AFM images illustrate electro deposited Pt and electron beam lithography Pt on STO <100>, the scale bar indicates 2 um.

The broad distribution of barrier heights observed for both n-STO <100> and <110> surfaces indicate significant site heterogeneity, which may arise from variations in defect densities, local band bending, and surface reconstructions. Notably, Pt on n-STO <110> exhibited a larger average Schottky barrier height than on n-STO <100> although these averages are within the variance of one another. This trend is consistent with prior work on oxide surfaces, where anisotropic surface dipoles and differing electronic polarizations between crystallographic facets influence charge transport at the interface. The increased barrier height on n-STO <110> suggests a slightly larger degree of band bending at the interface, likely due to differences in the intrinsic electronic structure and dipole formation at the <110> termination. These findings

underscore the importance of nanoscale surface interactions in controlling charge injection and extraction at perovskite interfaces and have direct implications for optimizing catalytic and electronic device applications involving n-STO-based heterostructures.

Conclusion:

This study demonstrates that cooperative adaptive junctions are essential for achieving efficient overall water splitting on STO. While previous models emphasized intrinsic crystal facet asymmetry, our findings show that electrocatalyst adaptation at the semiconductor interface plays a critical role in charge separation. Using AP-XPS, we observed that Pt and CoOx dynamically adjust their electronic structure under illumination and in the presence of alkaline electrolyte, with Pt acting as an electron collector and CoOx as a hole collector. These operando observations of changes in chemistry (work function) and barrier height form a self-reinforcing charge-separation mechanism beyond the buried Schottky junction model[40,41].

DWE measurements reveal that as Pt drives the HER, its barrier height decreases, making the interface more ohmic, while CoOx exhibits increased hole selectivity under OER conditions. This contrasts with buried junctions, which lack the adaptability needed to sustain the photovoltage required for water splitting. Conductive AFM further shows that barrier heights vary at the nanoscale, with electrodeposited Pt likely preferentially nucleating at surface defect sites but are on average equal across each crystal facet, reinforcing that charge separation is not dictated by facet orientation alone but by the local evolution of interfacial chemistry.

These results establish key engineering principles for PEC systems: (1) carrier-selective junctions should be designed with ionically porous adaptive catalysts; (2) ionic transport at the

semiconductor-electrocatalyst interface must be explicitly considered, as proton and hydroxide motion directly impacts charge separation; and (3) facet-selective catalyst deposition should be leveraged to trigger positive feedback loops in interfacial carrier selectivity, increasing photovoltage generation.

By revisiting STO as a model system, we provide a framework for designing adaptive photocatalytic systems beyond perovskites. Future work should explore ion transport dynamics in catalytic layers, quantify real-time electrocatalyst adaptation, and extend these principles to lower-bandgap oxides and particulate photocatalysts to advance fundamental PEC science.

Chapter 5: CONCLUSIONS

Section A. Summary of Findings

This dissertation has explored fundamental mechanisms governing charge selectivity in photoelectrochemical (PEC) systems, particularly in the context of catalyst-semiconductor interfaces. Through a combination of experimental techniques—including dual-working-electrode (DWE) measurements, conductive atomic force microscopy (c-AFM), ambient pressure X-ray photoelectron spectroscopy (AP-XPS), and electrochemical characterization—this work has demonstrated that charge-selective contacts arise from a range of interfacial mechanisms. These mechanisms include heterojunction formation, the pinch-off effect, buried junctions, adaptive junctions, and cooperatively adaptive junctions, each contributing uniquely to the efficiency and stability of PEC devices.

The findings of this work can be summarized as follows:

Pt|p-InP Photocathodes: The charge selectivity at Pt|p-InP interfaces is predominantly governed by the formation of an interfacial InOx heterojunction rather than hydrogen alloying effects. The pinch-off effect, observed at the nanoscale, plays a role in early junction formation but is ultimately dominated by oxide formation during electrochemical operation. These results challenge conventional Schottky junction models for noble metal contacts on III-V semiconductors and highlight the necessity of considering interfacial oxides when designing efficient photocathodes.

Wireless Photovoltage Mapping via AP-XPS: A new approach to measuring photovoltages wirelessly was developed, enabling direct observation of interfacial potential differences across chemically distinct sites. This technique was validated using interdigitated Schottky contact solar cells and then applied to PEC systems. The results demonstrated the capability of AP-XPS to measure photovoltages at buried interfaces, particularly in complex semiconductor-electrocatalyst architectures.

Adaptive and Cooperatively Adaptive Junctions on $SrTiO_3$: Single-crystal SrTiO3 served as a model system for studying charge separation at photocatalyst interfaces. The results demonstrated that adaptive junctions, where the electrocatalyst dynamically modifies its work function in response to electrochemical potential shifts, can significantly enhance charge selectivity. Furthermore, when both the HER and OER electrocatalysts exhibit adaptive behavior, they cooperate to form a self-reinforcing charge-separation mechanism, a phenomenon described as cooperative adaptation. This insight provides a framework for understanding the exceptionally high quantum efficiencies of $SrTiO_3$-based overall water splitting systems.

Section B. Implications for PEC Systems

The mechanisms elucidated in this dissertation provide crucial insights into the actionable design principle for PEC devices. By identifying the key factors that govern charge selectivity, this work informs strategies for improving the efficiency, stability, and scalability of PEC systems:

Interfacial Engineering: The discovery of oxide-mediated heterojunctions highlights the importance of precisely controlling interfacial chemistry. Future research should explore ways to engineer these junctions intentionally, either through surface treatments or controlled oxide growth, to enhance charge selectivity.

Wireless Characterization Techniques: The development of wireless photovoltage mapping using AP-XPS opens new possibilities for studying buried interfaces in PEC and photovoltaic systems. Future studies should extend this technique to complex multi-junction architectures and in operando conditions.

Catalyst Adaptability: The role of adaptive junctions in carrier selectivity suggests that electrocatalysts should not be treated as static components but rather as dynamic interfaces that respond to local chemical and electrostatic conditions. Designing catalysts that exhibit controlled adaptation could lead to more efficient and durable PEC systems.

Section C. Future Directions

While this work has addressed key questions in charge selectivity in PEC devices, several open challenges remain:

Expansion of Wireless Photovoltage Mapping: The AP-XPS approach should be extended to study a wider range of PEC materials, including tandem junctions and particulate photocatalysts. Additionally, incorporating time-resolved AP-XPS could provide insights into transient charge dynamics.

Beyond Water Splitting: The concepts of adaptive and cooperative junctions may apply to other photoelectrochemical reactions, such as CO2 reduction and nitrogen fixation. Future studies should explore how these mechanisms influence selectivity in multi-electron transfer reactions. Material Systems and Scalability: Applying these findings to emerging material systems, such as perovskite oxides and hybrid organic-inorganic PEC materials, could reveal new strategies for designing scalable and economically viable solar-to-chemical technologies.

Section D. Concluding Remarks

The research presented in this dissertation advances our understanding of charge-selective mechanisms in PEC systems and provides a foundation for designing more efficient photoelectrodes. By integrating interfacial characterization techniques with operando measurements, this work bridges the gap between fundamental semiconductor physics and applied materials science. Moving forward, leveraging these insights to develop practical, and relevant PEC devices will be critical for the realization of sustainable solar fuel production and more broadly, solar chemical conversion.

The findings of this work underscore the importance of thinking beyond simple band-alignment models and embracing the dynamic nature of semiconductor-electrocatalyst interfaces. As PEC technologies continue to evolve, understanding and harnessing these mechanisms will be essential for overcoming efficiency and stability limitations, bringing us closer to a future powered by solar-driven chemical transformations.

APPENDICES

Appendix A. Supporting Information for Paper A

Table A.S1. Symbols and definitions for paper A

Term	Symbol	Unit	Brief definition
Elementary charge	q	C	Magnitude of charge on a single electron (F/N_A)
Stoichiometric number	ν_i	Unitless	Number of species i in a balanced equation
Signed charge number	z_i	Unitless	Signed charge number of species i (for example, +2, +1, 0, −1, −2)
Avogadro's constant	N_A	mol^{-1}	Number of entities in 1 mol of a given substance
Faraday constant	F	$C\ mol^{-1}$	Magnitude of charge per mole of protons
Electron-transfer rate constant	$k_{rxn,et}, k'_{rxn,et}$	$cm^4\ s^{-1}$	Electron-transfer (et) rate constant for a second-order heterogeneous surface reaction; the prime indicates the reverse reaction
Hole-transfer rate constant	$k_{rxn,ht}, k'_{rxn,ht}$	$cm^4\ s^{-1}$	Hole-transfer (ht) rate constant for a second-order heterogeneous surface reaction; the prime indicates the reverse reaction
Electron concentration	$n,\ n_{rxn,s},\ n^{eq}_{rxn,s}$	cm^{-3}	Concentration of electrons in the conduction band (n), the surface concentration is denoted by subscript s and eq indicates the equilibrium value
Hole concentration	$p,\ p_{rxn,s},\ p^{eq}_{rxn,s}$	cm^{-3}	Concentration of holes in the valence band (p), the surface concentration is denoted by subscript s and eq indicates the equilibrium value
Activity	a_i^{α}	Unitless	The activity of species i in phase α is defined by $a_i^{\alpha}=\gamma_i^{\alpha}C_i^{\alpha}/C_i^{0,\alpha}$, where, γ_i^{α} is the activity coefficient, C_i^{α} is the concentration and $C_i^{0,\alpha}$is a reference concentration, usually taken to be 1 M for soluble species
Electrostatic potential	ϕ	V	Electrical work needed to move a test charge to a specific point in space from a reference point (often at infinite distance) divided by the value of the charge
Reduction potential	ε	V	Free-energy change divided by the electron charge associated with moving an electron (and any associated ion/solvent movement/rearrangement) from a reference

Term	Symbol	Unit	Brief definition
			state (often a reference electrode) into the bulk of a solution via a redox reaction
Formal reduction potential	$\varepsilon^{\circ\prime}$	V	Potential measured for a reduction reaction with a standard-state concentration for each species
Effective conduction and valence band density of states	N_C and N_V	cm^{-3}	The number per volume of thermally accessible electron and hole states at E_c and E_v, respectively
Charge density	ρ	$C\ cm^{-3}$	The amount of electric charge per unit volume
Debye length	λ	cm	A characteristic length over which mobile charge carriers screen an electric field, which decreases with mobile carrier density
Depletion width	w	cm	Length over which mobile carriers are depleted at a doped semiconductor surface or junction
Donor and acceptor density	N_D and N_A	cm^{-3}	Number density of electrons and holes donated to the conduction and valence band, respectively, by impurity atoms
Vacuum energy level	E_{vac}	eV	Energy of a free stationary electron outside of a material, typically defined to be zero
Conduction and valence band edge	E_c and E_v	eV	Energies analogous to the LUMO and HOMO for semiconductor solids (often referenced to the vacuum energy level)
Bandgap	E_g	eV	Energy separation between E_c and E_v
Electrochemical potential	$\bar{\mu}_i^{\alpha}$	$J\ mol^{-1}$	Partial molar Gibbs free energy of a given species i in phase α, which defines the criteria for equilibrium
Chemical potential	μ_i^{α}	$J\ mol^{-1}$	Partial molar Gibbs free energy, ignoring long-range electrostatic contributions
Fermi level	E_f, E_{fp}, E_{fn}	eV	Electrochemical potential ($\bar{\mu}_e^{\alpha}$) of electrons in phase α; the subscripts p and n denote carriers only in the valence or conduction band, respectively
Gibbs free energy	G	J	Thermodynamic potential used to calculate the maximum amount of non-pressure-volume work that may be performed at constant temperature and pressure

Term	Symbol	Unit	Brief definition
Open-circuit voltage	V_{oc}	V	The difference in the electron electrochemical potential (divided by charge) between two contacts with no external current flow
Partial current density	$J_n(x)$, $J_p(x)$	C s^{-1} cm^{-2}	The amount of electrical charge passed by electrons (n) or holes (p) per unit time per unit area at position *x*, which sum to the total charge density
Equilibrium exchange current density	J_{0n}^{x}, J_{0p}^{x}	C s^{-1} cm^{-2}	The partial current density at position *x* for electrons (n) or holes (p) at equilibrium
Temperature	T	K	Absolute temperature
Pressure	P	Pa	Force exerted per unit area
Ideal gas constant	R	J K^{-1} mol^{-1}	Avogadro's number multiplied by the Boltzmann constant
Differential capacitance	C_{sem}, C_{edl}	F cm^{-2}	Differential capacitance of the semiconductor, differential capacitance of the electrical double layer
Number of species in a phase	N_i	Number	The number of particles of the species *i*.

1. rxn, reaction number; LUMO, lowest-unoccupied molecular orbital; HOMO, highest-occupied molecular orbital.

Appendix B. Supporting Information for Paper B

Experimental Section/Methods

Photocathode preparation: All semiconductor substrates used in this study were cut from single-side-polished p-InP (N_a = Zn 4.2 × 10^{17}) from MTI. Ohmic back contacts were fabricated by thermally evaporating Au (20 nm)/Zn (30 nm)/Au (50 nm) on the unpolished p-InP face and annealing at 450 °C for 90 s in air. A small shadow mask was used to create two disconnected backside contacts to ensure ohmic current-voltage response through the backside to the p-InP.

Electrodes were fabricated using a Sn–Cu wire (length ~20 cm, –30 American wire gauge, McMaster Carr) electrically connected to the ohmic back contact by Ag paint (Ted Pella, Inc), fed through a glass tube. All but the active region of the electrode was encapsulated in epoxy. The electrodes were pretreated with HCl (concentrated HCl (Fisher Chemical) until rapid gas evolution was observed) or H_2O_2/HCl (5 min etch 0.25 M H_2O_2 (Fisher Chemical)/1 M HCl followed by a 15 sec etch in 2 M HCl), rinsed with water (18.2 MΩ cm) and dried with and N_2 gas stream.

A Bio-Logic SP300 potentiostat was used to electrodeposit Pt on the p-InP electrodes. A solution of 0.5 M Na_2SO_4/4 mM H_2PtCl_6 in water (18.2 MΩ cm) was used for electrodeposition. Pt was deposited at -0.15 V vs. SCE (Standard Calomel Electrode, Accumet) with a Pt wire coil counter electrode under illumination of 100 mW cm^{-2} solar simulated light (Abet Technologies, 10500) until the predetermined amount of charge had passed. Prior to insertion of the photocathode, the deposition solution was sparged with N_2 for 15 min to remove dissolved O_2. The deposition time was controlled by integrated current density, 5, 30, 100 mC cm^{-2} to create various particle densities. The electrodes were rinsed with water (18.2 MΩ cm) and dried with N_2. For some electrodes, instead 40 nm of Pt was deposited by physical vapor deposition (AMOD, Angstrom Engineering).

Electrochemical measurements: A Bio-Logic SP300 potentiostat was used to measure the electrochemical behavior of the photocathodes. The electrolyte was aq. 1 M $HClO_4$ (JT Baker Chemical Co.)saturated with H_2 by bubbling. Illuminated cyclic voltammograms, with a ramp rate of 20 mV/s, were carried out in an electrochemical cell with an SCE reference electrode and an Pt wire coil counter electrode in a separate chamber separated by a glass frit. The electrolyte was

rapidly stirred to remove H_2 bubble formation. The photocathode was illuminated with ~100 mW cm^{-2} of solar simulation, measured by a photodiode (ThorLabs UDT UV-005). Current densities were calculated from the total active region of each electrode determined using a calibrated digital scanner.

Dual-working-electrode (DWE) measurements used the second channel on the SP300 potentiostat, fitted with an ultra-low current module, to control the second working electrode attached to the catalyst layer. Both channels reference electrode leads were shorted to the same SCE electrode in the 1 M $HClO_4$. Similarly, the counter-electrode leads were also shorted to the same Pt-wire-coil counter electrode.

The fabrication procedure for the DWE electrodes follows that detailed above, except Pt was deposited by PVD after electrode preparation. Sn–Cu wire was electrically connected to this film by Ag paint and all but the active area was encased in epoxy to avoid shorts and to precisely define the geometric active area.

Electron Beam Lithography and AFM measurements: Effective removal of the native oxide was critical for EBL prepared samples. The samples were rinsed with acetone, isopropyl alcohol, and H_2O while mounted the spin coater (Headway Research), and spun dry after each step (3000 rpm for 60 s). A solution of 0.25 M H_2O_2 / 1 M HCl was placed on the substrate for a 5 min etch followed by a 15 s etch in 2 M HCl, and then spun to dry after each step.

The electron-beam resist (CSAR AR-P-6200.4, Allresist) was pulled into a syringe and warmed to room temperature prior to deposition. The resist was then dropped on the substrate to cover the sample completely and spun at 3000 rpm for 60 s. A soft bake at 150 °C was performed for 1 min to solidify the tacky film. This procedure produced resist films of 100 nm in thickness, measured by stylus profilometry (Veeco Dektak 6M).

EBL patterns were coded in NPGS (JC Nabity) and written using a ThermoFisher Apreo S2 SEM. The nanodisks were written at 5 kV with a beam current 50 pA (43.1 pA measured) to increase scattering events inside the resist. Point exposures ranging from 1 to 50 fC was used to define dots with 1 um center to center pitch

The exposed samples were developed in AR 600-548 at 0 °C in an ice bath for 1 min. The samples were promptly rinsed with water (18.2 MΩ cm) and dried with N_2. The developed samples were metalized with 5 nm or 8 nm of Pt, deposited at 0.5 Å/s by electron-beam deposition. Lift-

off was performed with dichloromethane (DCM, Sigma Aldrich) by soaking for 5 min. Agitation was performed during the soak by jets of DCM with a needle and syringe to facilitate liftoff.

A Bruker Dimension ICON with ScanAsyst was used for topographical AFM and C-AFM measurements, using the onboard SMU. SCM-PIT-V2 probes were used for all measurements. Both electrodeposited Pt nanoparticles and EBL-defined Pt nanodisks were analyzed by the C-AFM.

*XPS and TEM***:** All samples analyzed by X-ray photoelectron spectroscopy (XPS) used an ESCALAB 250 (ThermoScientific) and an Al Kα monochromated source (20 eV pass energy), 500 μm spot size). The samples were charge-neutralized using an in-lens electron source. Spectra were analyzed using ThermoScientific Avantage 4.88 software. The adventitious C 1s signal at 284.8 eV was used to calibrate the binding energy scale.

A FEI TITAN 80-200 TEM/STEM with ChemiSTEM was used for collecting the data at 200 kV in Figure 5. TEM Lamella was prepared on a dual-beam FEI Helios and milled with Ga ions. The selected areas were coated with 100 nm of electron-beam-deposited carbon and then 1000 nm of ion-beam-deposited carbon to protect the interface during imaging.

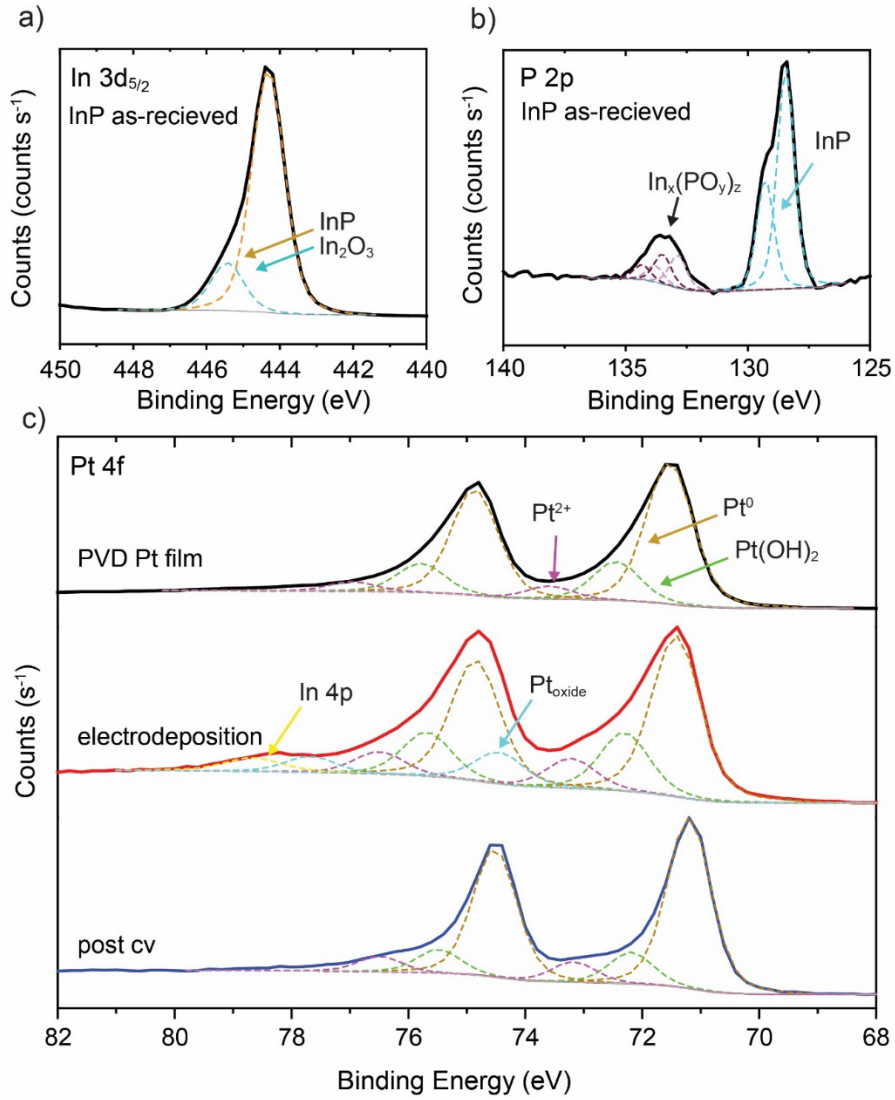

Figure B.S1. a,b) XPS spectra of In $3d_{5/2}$ and P 2p of "as-received" InP. c) Pt 4f XPS spectra of an as-deposited 40-nm-thick Pt film on p-InP (top), electrodeposited Pt atop an H_2O_2/HCl pretreated p-InP surface (middle), and electrodeposited Pt after electrochemical cycling (one dark cycle and five illuminated cycled in 1 M $HClO_4$) All Pt 4f spectra were fit with sets of doublets except for the electrodeposited Pt sample where a singlet corresponding to In 4p state was added at 78.7 eV to account for the overlap in energy between Pt 4f and In 4p.

Table B.S1. In $3d_{5/2}$ spectra peak positions for all samples in the manuscript.

Source	**In $3d_{5/2}$ (eV)**					
	InP	InO_x	$InPO_x$	$In(PO_3)_3$	$In(PO_3)$	$InPO_4$
Literature	444.3[1-5]	444.9[1-4]	/	445.4[1-4]	445.5[3]	445.7[1-2, 5]
H_2O_2/HCl etch	444.5	445.3	/	/	/	/
eDep Pt	445	445.8	446.4	/	/	/
eDep Pt, CV	444.9	445.8	/	/	/	/

EBL Pt, CV	444.2	445.3	/	/	/	/
As-Received	444.3	445.1	445.7	/	445.7	/

Table B.S2. P 2p spectra peak positions for all samples in the manuscript.

Source	P 2p (eV)					
	InP	InP_{surf}	$In(PO_3)$	$InPO_4$	$In(PO_3)_3$	P_2O_5
Literature	128.8[2-6]	129.06[5]	133.5[3, 6]	133.81[1-2, 4-5]	134.3[1-2, 7]	135.0[1, 3]
H_2O_2/HCl	128.5	129.0	132.1	132.8	/	/
eDep Pt	129.0	129.8	132.6	133.3	133.9	/
eDep Pt, CV	128.9	129.6	132.5	133.2	133.8	/
EBL Pt, CV	128.5	129.2	132.5	133.1	/	/
As-Received	128.4	/	132.8	133.5	/	/

Table B.S3. $In3d_{5/2}$ spectra atomic percent of each species present relative to the total amount of that element in each spectra for all samples in the manuscript.

Source	In $3d_{5/2}$		
	InP	InO_x	$InPO_x$
H_2O_2/HCl	91.0%	9.0%	/
eDep Pt	61.7%	27.6%	10.8%
eDep Pt, CV	86.6%	13.4%	/
EBL Pt, CV	84.0%	16.0%	/
As-Received	76.8%	15.6%	7.6%

Table B.S4. P 2p atomic percent of each species present relative to the total amount of that element in each spectra for all samples in the manuscript from XPS analysis.

Source	P 2p				
	InP	InP_{surf}	$In(PO_3)$	$InPO_4$	$In(PO_3)_3$
H_2O_2/HCl	85.6%	6.5%	3.5%	4.4%	/
eDep	51.1%	2.6%	13.7%	15.8%	16.8%
eDep CV	76.6%	7.1%	4.9%	5.8%	5.7%
EBL CV	72.9%	8.8%	8.1%	10.3%	/
As-Received	77.1%	/	10.8%	12.1%	/

Additional Discussion.

H_2O_2/HCl pretreatment removes phosphorus oxides and In_2O_3 from the as-received sample as is evidenced by comparing InP peaks (substrate) in both the In $3d_{5/2}$ (Table S3) and the P 2p (Table S4) spectra. Physical-vapor-deposited Pt on top of H_2O_2/HCl pretreated p-InP is considered,

within this work, a “pristine” Pt/p-InP junction. This pristine junction was observed to have ohmic (linear) current-voltage response, as simple Schottky-contact models predict (Figure S4). EBL-defined Pt nanodisks were subject to an H_2O_2/HCl pretreatment before electron-beam deposition of Pt, yielding a nearly pristine junction between Pt and p-InP. A thin native oxide is likely to have grown around the nanodisks, however, before dry C-AFM measurements were conducted in air which we hypothesize leads to pinch-off effects.[8-10] After undergoing one dark CV (-0.3 to 0.5 V vs SCE) in 1 M $HClO_4$ and 5 illuminated CV cycles (-0.3 to 0.6 V vs SCE), with one sun equivalent illumination, In and P oxides were observed in a greater degree than in the H_2O_2/HCl pretreated p-InP sample (Figure 1, Table S3 and Table S4). XP Spectra of a sample with a 40 nm Pt film on p-InP displayed in Figure S1c., was shown to match that of the electrodeposited (eDep) Pt after photoelectrochemical cycling in 1 M $HClO_4$, indicating that a permanent change in the composition of Pt is likely not the dominant mechanism for the formation of the charge-selective junction. The presence of oxides in the photoelectrodeposited Pt samples was observed in high percentages immediately after deposition (Table S3 and Table S4). TEM images of the Pt nanodisk ample (Figure 5) after photoelectrochemical cycling (one dark, five light CVs) indicate that the amorphous oxide grew underneath the nanodisk, apparently forming an electrical heterojunction.

Samples containing electrodeposited Pt displayed a binding-energy shift, to lower binding energy, for the peaks in the In $3d_{5/2}$ and P 2p spectra. However, this redshift is not observed in the Pt 4f spectra. Therefore, we propose this redshift is caused by surface charging effects with the presence of electrodeposited Pt. The subsequent species peak identification was appropriately adjusted.

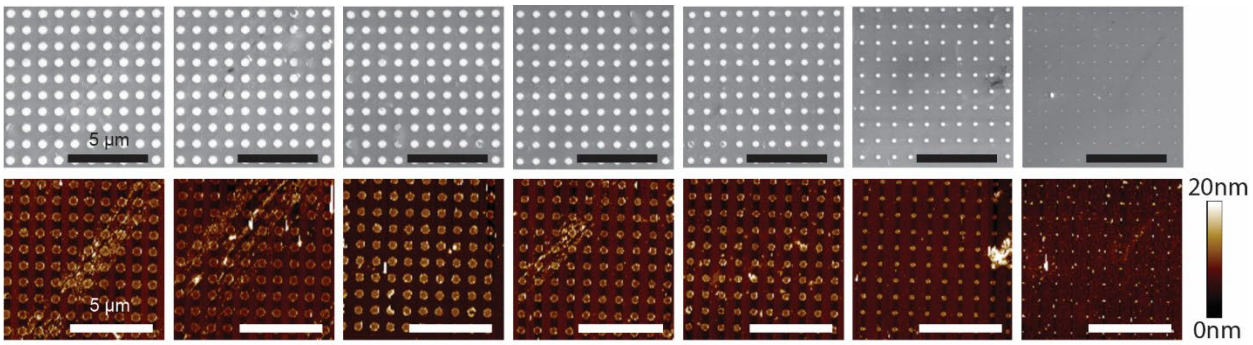

Figure B.S2. Correlated SEM and AFM EBL grid. SEM micrographs (top) and AFM topographical maps (bottom) of the same EBL defined Pt nanodisk arrays (vertically aligned), scale bars indicate 500 nm.

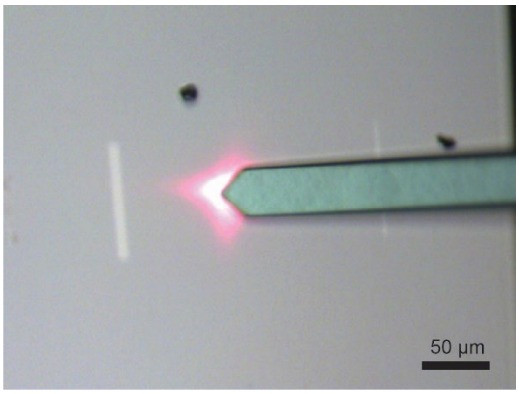

Figure B.S3. AFM Cantilever. Bruker SCM-PIT Pt-Ir coated cantilever engaged with the electrode surface. Illumination for C-AFM experiments was created by the onboard laser light spillover (690 nm) creating ~ 5 sun intensity, estimated with a ThorLabs UDT UV-005 photodiode. Dark C-AFM measurements were conducted with the laser spot located near the aft end of the cantilever, ~400 µm away from the area of interrogation.

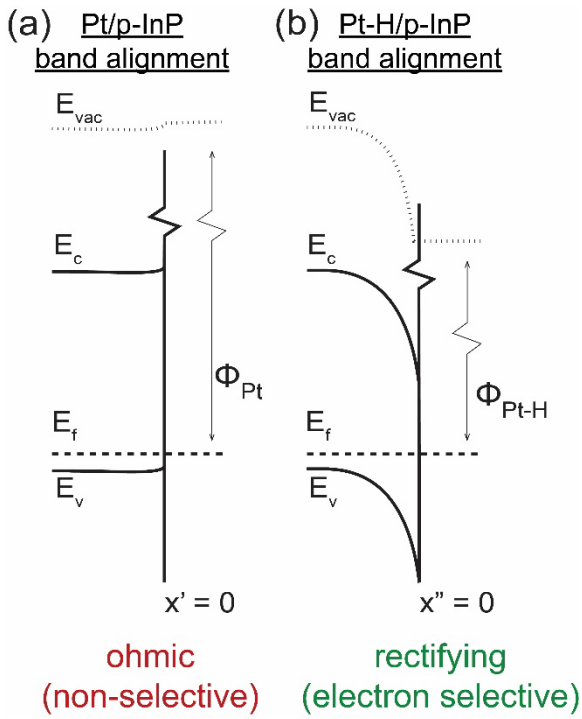

Figure B.S4. p-InP | Pt junction. (a) Schematic band alignment for Pt/p-InP based on convention Schottky-junction models, and (b) hypothesized band alignment and barrier created in the adaptive junction picture (H_2 absorption).

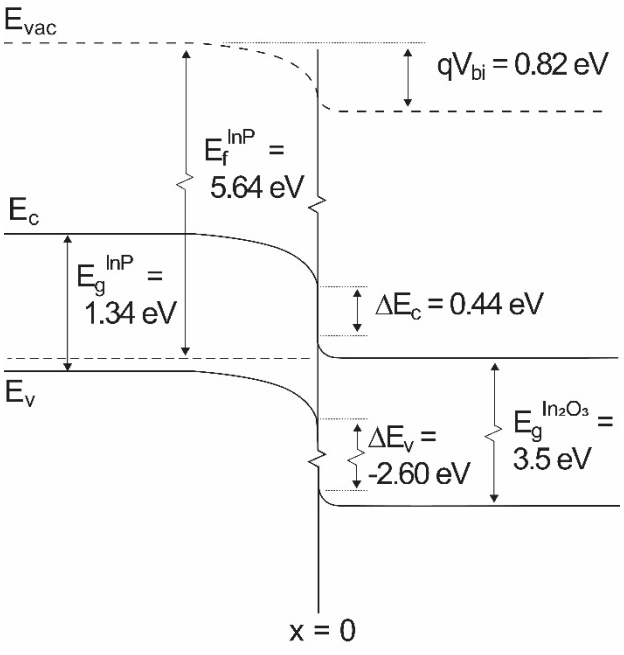

Figure B.S5. p-InP | InOx | Pt junction. Heterojunction band alignment schematic with reported energy values adopted from Leibovitch and modified for the p-InP used in this study.[11] Using 1.1×10^{-21} cm^{-3} as the effective density of states for p-InP, the distance from the valance band maximum (E_v) and the Fermi level (E_f) would be 0.084 eV. Therefore, the expected barrier for this

heterojunction is 0.904 eV. E_c and E_g denote the conduction band energy and the bandgap, respectively.

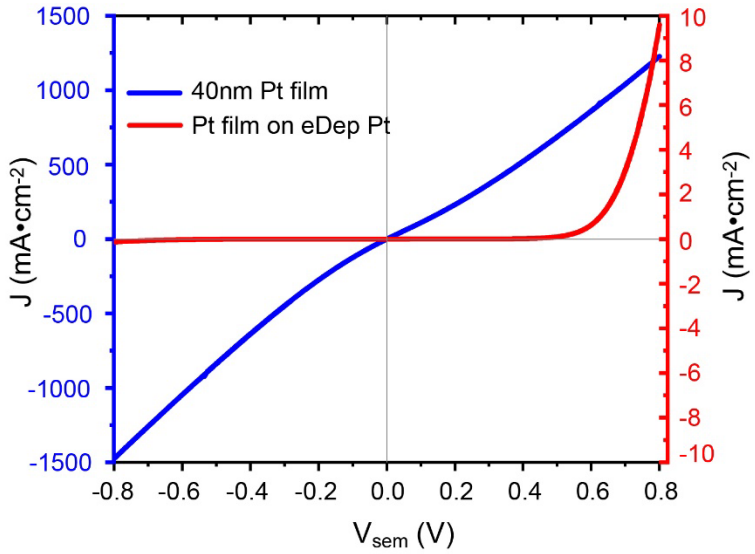

Figure B.S6. Dry *J-V* curves. Dry two-electrode *J-V* curves of 40-nm Pt film on freshly etched InP (blue and left axis) compared with a sample with 40 nm Pt film by PVD deposited on 5 mC cm^{-2} electrodeposited Pt/p-InP. The Pt film on the freshly etched InP displays ohmic behavior whereas the same PVD Pt film on the electrodeposited Pt/p-InP displays rectifying behavior. Forward bias corresponds to positive potentials applied to the semiconductor ohmic back contact relative to the Pt top contact.

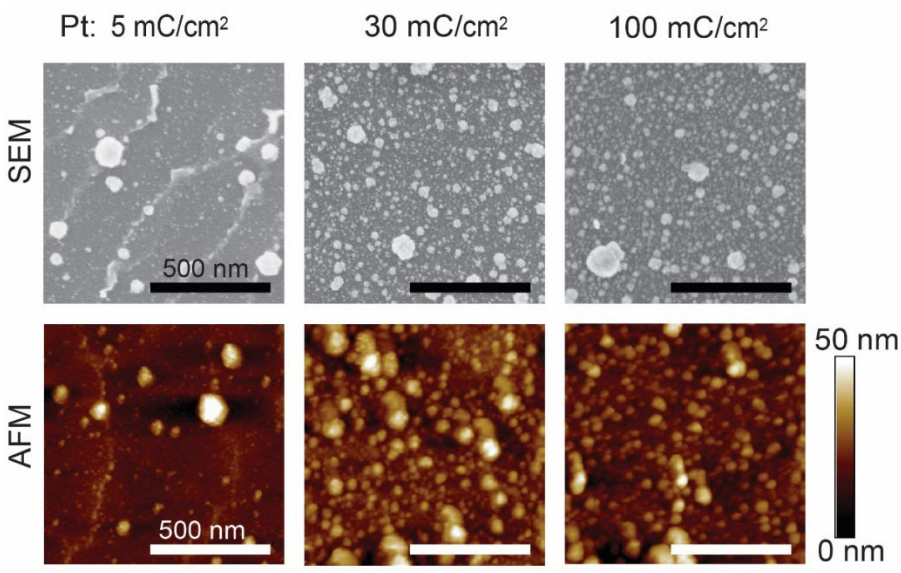

Figure B.S7. Correlated SEM and AFM of electrodeposited Pt. SEM micrographs (top) and AFM topography maps (bottom) of electrodeposited Pt with integrated current densities at 5, 30, and 100 mC cm^{-2}. SEM and AFM maps are vertically aligned with different regions on the same electrode and the scale bars are all the same size.

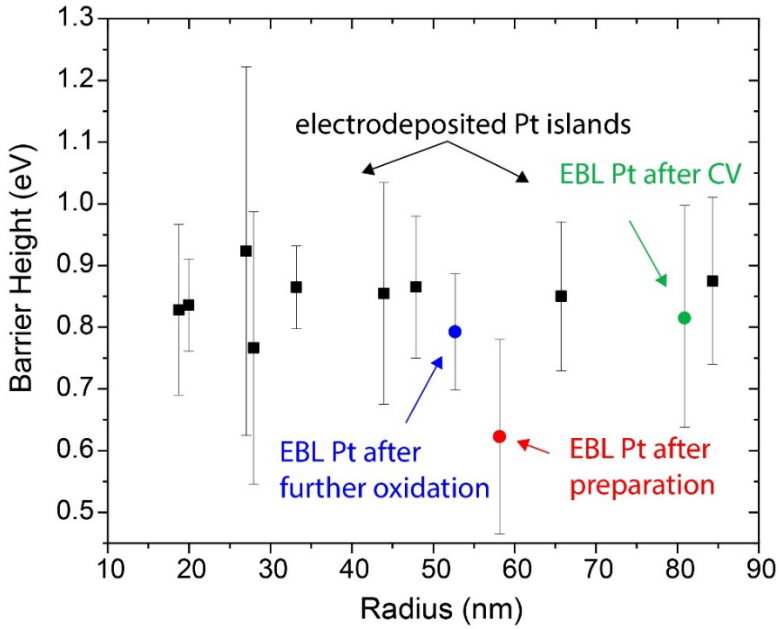

Figure B.S8. Calculated barrier heights across sample type. Barrier height calculations from electrodeposited nanoparticles and EBL-defined Pt nanodisks of comparable size on p-InP.

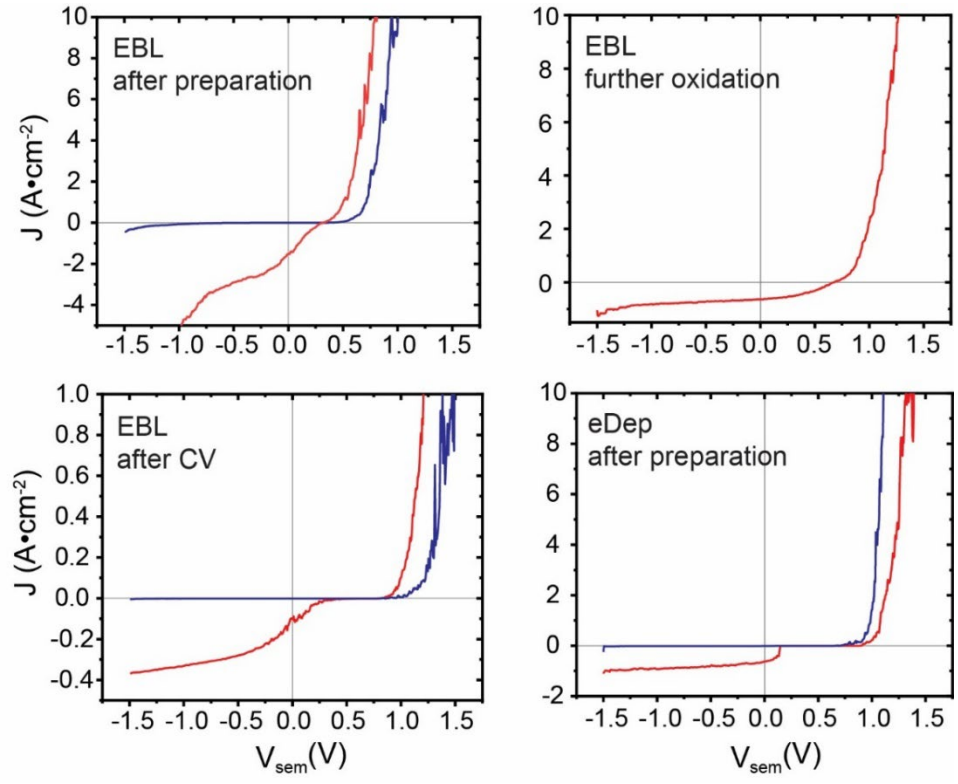

Figure B.S9. Typical C-AFM measurement. Example C-AFM current response to voltage ramps of nanoscale contacts in air under the dark conditions (blue) and under 5 suns equivalent illumination (red) by the onboard 690 nm laser.

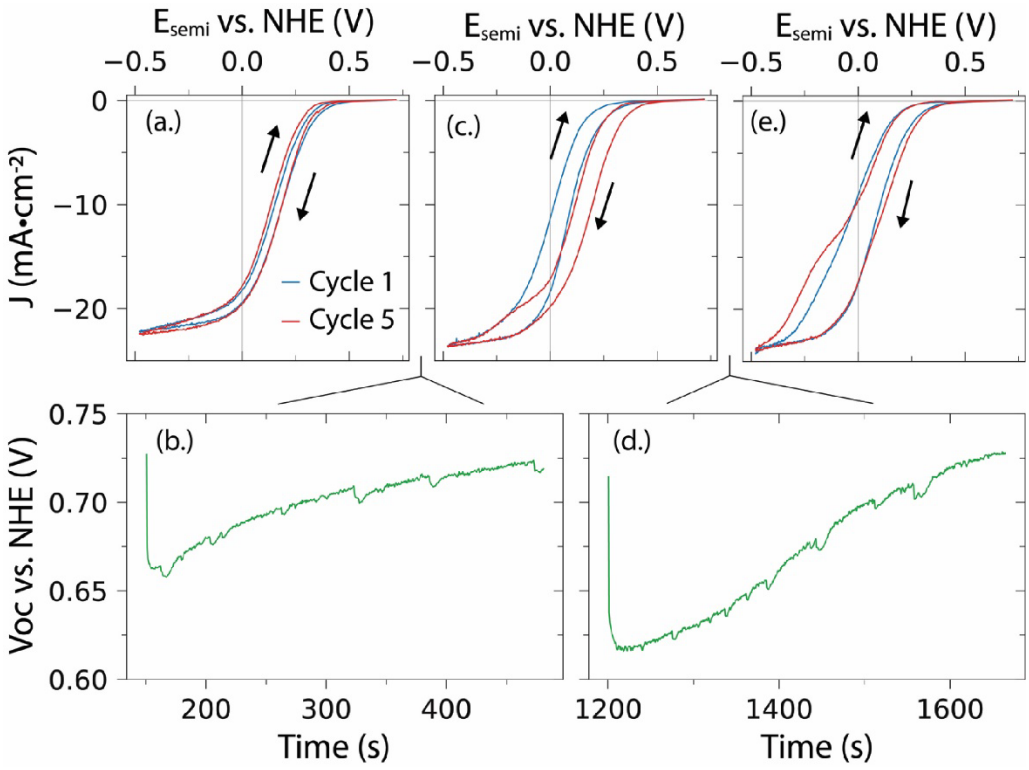

Figure B.S10. Dynamic V_{oc}. Open-circuit voltage (V_{oc}) degradation and recovery. Electrodeposited Pt (30 mC cm^{-2})/p-InP photocathodes were cycled in 1 M $HClO_4$ and illuminated with 1 sun equivalent light intensity. Three CV experiments each of 5 cycles (a,c,e) were sequentially conducted with irradiated open-circuit voltage data collected in between each of the CV experiments (b,d). The first data points in plots (b) and (d) are artifacts from the end of the previous scan, ending at the initial open-circuit voltage. The open-circuit voltage recovery is evident when the sample is sitting at open circuit under illumination, presumably due to the formation/recovery of the interfacial oxide that creates the charge selective heterojunction.

Pinch-off Discussion: A Pt/p-InP "pristine" contact may become pinched-off if the contact's lateral dimension is on the order of the depletion width of a higher-barrier-forming peripheral n-type oxide grown in air.[9-10] In the case of pinched-off particles which begin to grow a thin interfacial oxide, the thin n-type oxide interlayer, fully depleted by Pt, may still display the pinch-off effect albeit to a lesser degree due to shielding. Nonetheless, the electronic transport behavior of such pinched-off contacts can be described by Tung's patch theory, Equation S1.[8-9] This theoretical transport equation resembles that of the familiar Schottky diode equation with a barrier correction

term (C_b, describing the radially inhomogeneous barrier height) and an area correction term (C_a, describing the radially inhomogeneous current densities).

$$\mathrm{I_{patch}} = \mathrm{A^*\ T^2\ C_a} \exp\left(\frac{\phi_b^0}{\mathrm{k_B T}} + C_b\right)\left(\exp\left(\frac{\mathrm{qV_{app}}}{\mathrm{nk_B T}}\right) - 1\right) \quad \text{(S1)}$$

$$C_a = \frac{4\pi k_B T}{9q}\left(\frac{3\Delta r^2}{4}\right)^{\frac{1}{3}}\left(\frac{\epsilon_s}{qN_A V_{bb}}\right)^{2/3} \quad \text{(S2)}$$

$$C_b = \frac{q}{k_B T}\left(\frac{3q\Delta r^2 N_A V_{bb}}{4\epsilon_s}\right)^{1/3} \quad \text{(S3)}$$

Pinch-off is seen on disk (particle) size scales of $\frac{\Delta}{V_{bb}} > \frac{2r}{W}$, where W is the width of the depletion region (given by $\sqrt{\frac{2\epsilon_s V_{bb}}{qN_A}}$ and $V_{bb} = \phi_b^0 - V_n - V_{app}$, Δ is the difference in barrier height between the patch and the periphery ($\phi_b{}^0$) and V_n is the difference between the conduction band minimum and the Fermi level. Since the barrier between Pt and pristine p-InP ($N_A = 4.3\times10^{17}$) is considered to be zero and the peripheral barrier is thought to be 1 eV (In_2O_3/p-InP), $\frac{\Delta}{V_{bb}} \approx 1$.

Illuminated nano contacts which generate photocurrent in turn, develop an open-circuit voltage vs. the ohmic back contact. Solving Equation S1 for the open-circuit voltage yields,

$$qV_{oc} = nk_B T \ln\left(\frac{J_{ph}A\{r\}}{A^* T^2\, C_a\{r\} exp\left(\frac{\phi_b^0}{k_B T} + C_b\{r\}\right)} + 1\right) \quad \text{(S4)}$$

Heterojunction Schottky-like Barrier discussion: Due to the high expected electron concentration In_2O_3, we assume the junction approaches the Mott-Schottky metal/semiconductor limit and can be effectively modeled by the ideal diode equation, Equation S5.

$$J = J_0\left(\exp\left(\frac{qV_{app}}{nk_BT}\right) - 1\right) \quad \text{(S5)}$$

$$J_0 = A^*T^2\exp\left(-\frac{\varphi_b}{k_BT}\right) \quad \text{(S6)}$$

$$qV_{oc} = nk_BT\ln\left(\frac{J_{ph}}{J_0} + 1\right) \quad \text{(S7)}$$

Since $\frac{J_{ph}}{J_0}$ is typically >>1, $qV_{oc} = nk_BT\ln(\mathrm{J_{ph}}) + nk_BT\ln\left(A^*T^2\right)\frac{\varphi_b}{k_BT}$, we can see the relationship of V_{oc} and the junction barrier height. Of course, ln(J_{ph}) also is a function of the barrier height however this parameter influences qV_{oc} to a lesser degree when moderately perturbed from a non-zero φ_b.

Transport properties: A non-selective, ohmic junction, is expected for the pristine Pt and p-InP interface. This was observed for 40-nm Pt films deposited by physical vapor deposition on H_2O_2/HCl pretreated p-InP. Additionally, large radius Pt nanodisks defined by EBL were observed to be non-selective (Figure 4b), in accordance with pinch-off theory.[8-10, 12] Non-selective films were observed to develop a reversible small barrier in Figure 2b when the 40 nm films were exposed to an H_2-rich atmosphere. This behavior has been attributed to the formation of a small interfacial dipole in Pt (and Pd) H_2-gas-sensing devices and measured in Figure 3c to increase the interfacial barrier by ~50 meV.[13-14] An irreversible transformation from ohmic to rectifying was observed in Figures 3c and 4b where a significant energetic barrier was established (~0.93 eV) and (~0.83 eV) after electrochemically cycling under irradiation in 1 M $HClO_4$.

Pt nanoparticles deposited by electrodeposition were observed to immediately be rectifying in Figure S9. Figure S8 shows that electrodeposited particles have a barrier height independent of

the particles' radius. Additionally, energetic barrier heights calculated for the EBL-defined nanodisks, post-electrochemical cycling, and EBL nanodisks, following further oxidation in room temperature air, all display the same barrier height (within one standard error). Barrier heights calculated from the DWE experiment (40 nm Pt film) in the Figure 3b inset, fall within the standard error of ex situ dry barrier heights calculated in Figure S7.

Macroscopic CV scans of electrodeposited Pt nanoparticles display tunnel junction behavior for photoelectrodes with low Pt loading. Smaller particles are more susceptible to the effects of undercutting by a peripheral nonconductive oxide. Increased tunnel junction behavior was observed in Pt/p-InP on electrode particles and in EBL-defined nanodisks after photoelectrochemistry. This behavior can be observed in the illuminated *J-V* curves recorded by C-AFM in Figure S9 where large resistances were observed in the illuminated *J-V* curves at V_{oc}. Transitions in electronic properties and electron densities in the complex oxide and may be attributed to the population and removal of oxygen vacancies along with the chemical transition of the oxide to liberated protons during photo-electrochemistry.[15-18]

Appendix C. Supporting Information for Paper C

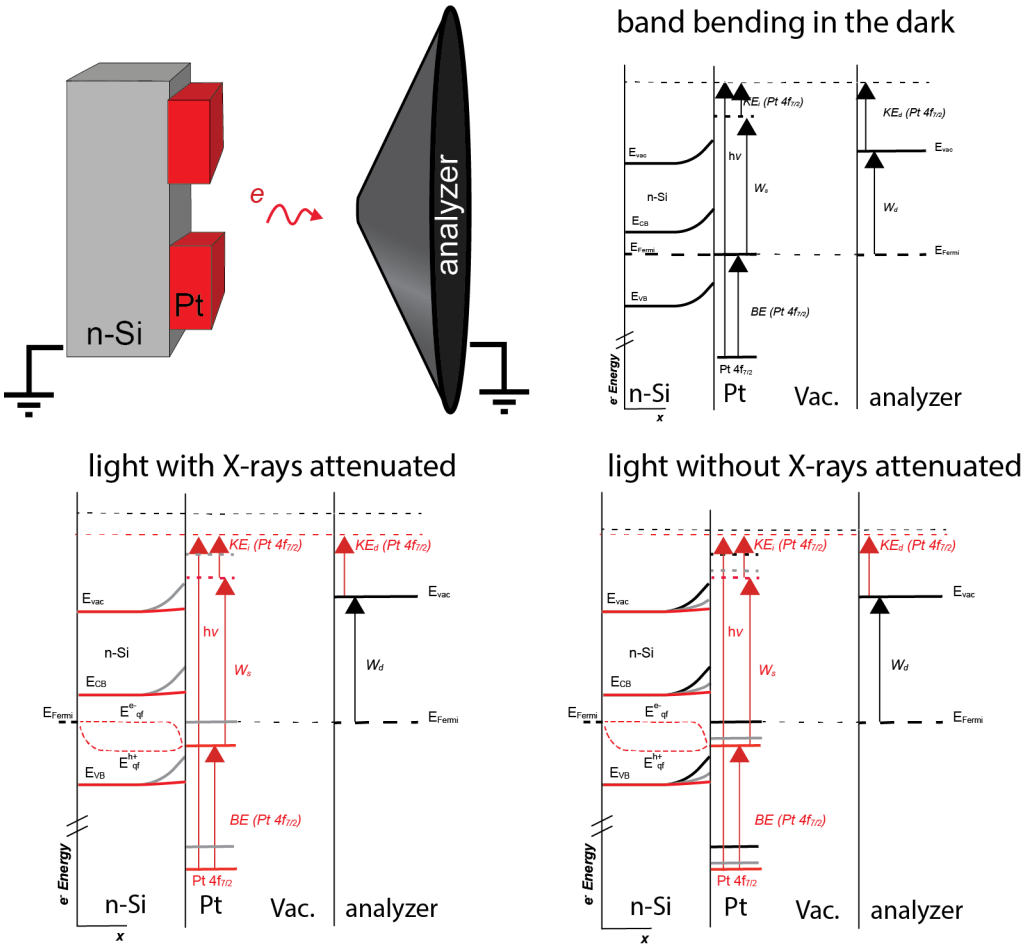

Figure C.S1. Wireless Photovoltage Measurement Diagram. Energy diagram wireless photovoltage measurement for n-type silicon with Pt barrier contact, top left panel illustrates the a diagram of the sample and the analyzer's cone. The panel on the top right illustrates a band diagram for the Pt|n-Si juction with the energies of the detector the analyzer. The panel on the bottom left illustrates a band diagram for the Pt|n-Si juction with the energies of the detector the analyzer with exclusivly solar illumination. The panel on the bottom right illustrates a band diagram for the Pt|n-Si juction with the energies of the detector the analyzer with x-ray generated carriers in quasi-equilibrium and solar illumination. The arrows indicate the energy compoents of the photogenerated carriers.

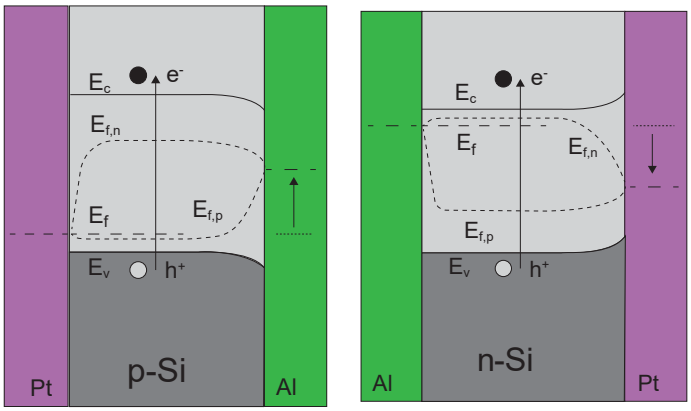

Figure C.S2. Band diagrams for n and p-type Si. Band diagram for n- and p-type Si with Al and Pt contacts, like those used in this study. Al is the the Schottky barrier contact on p-Si where Pt is the Schottky barrier contact for n-Si.

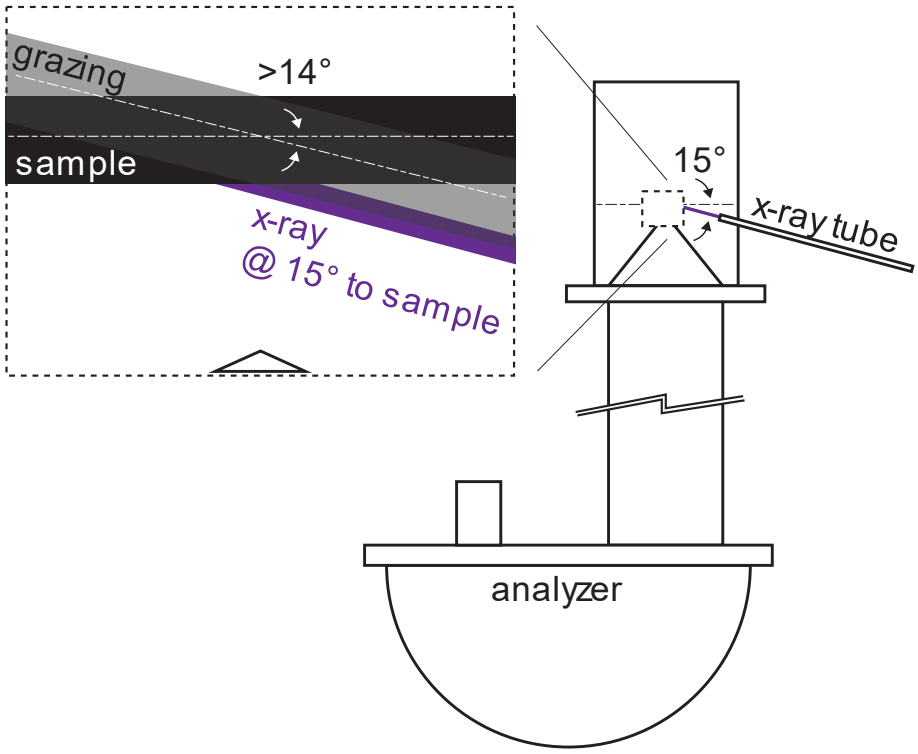

Figure C.S3. 9.3.1 Chamber configuration. BL9.3.1 sample configuration at standard and grazing conditions (>14° tilt, resulting in a <1° grazing angle) with the xrays fixed at 15° to standard surface.

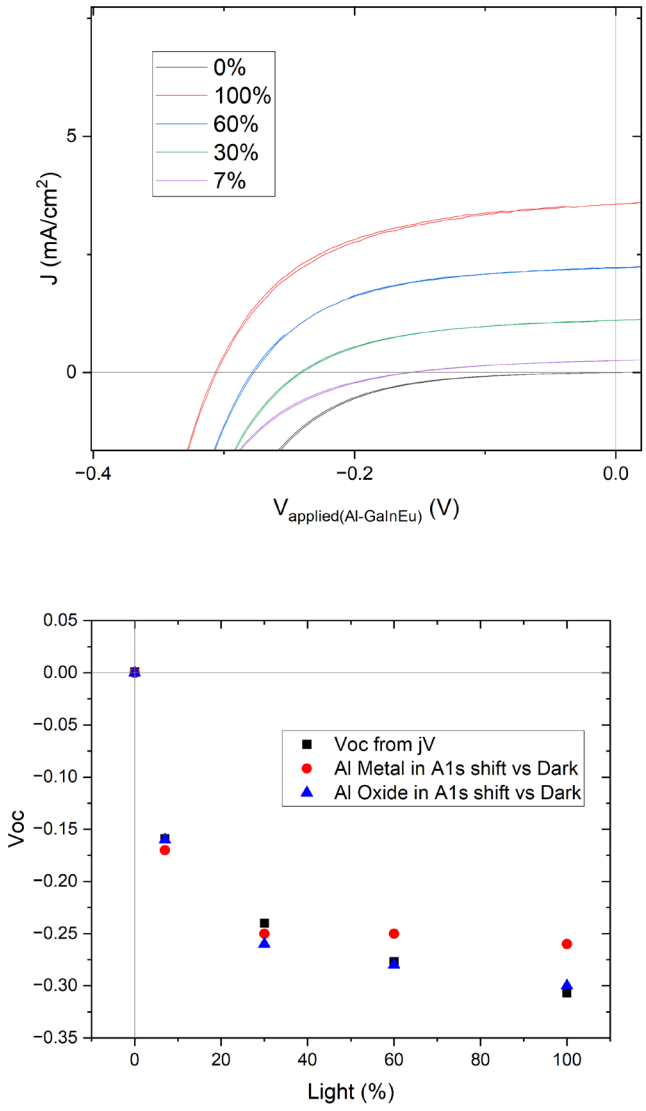

Figure C.S4. V_{oc} study as a function of light intensity. Al barrier contact pad study measured by in-situ j/V characterization (left) and wireless AP-XPS (right) as a function of the solar simulators maximum output, measured at the sample to be 0.1 sun. These data show that similar to electrical characterization, wireless photovoltage by AP-XPS can measure varied photovoltages as a function of light intensity, coupled to material specific core-level features

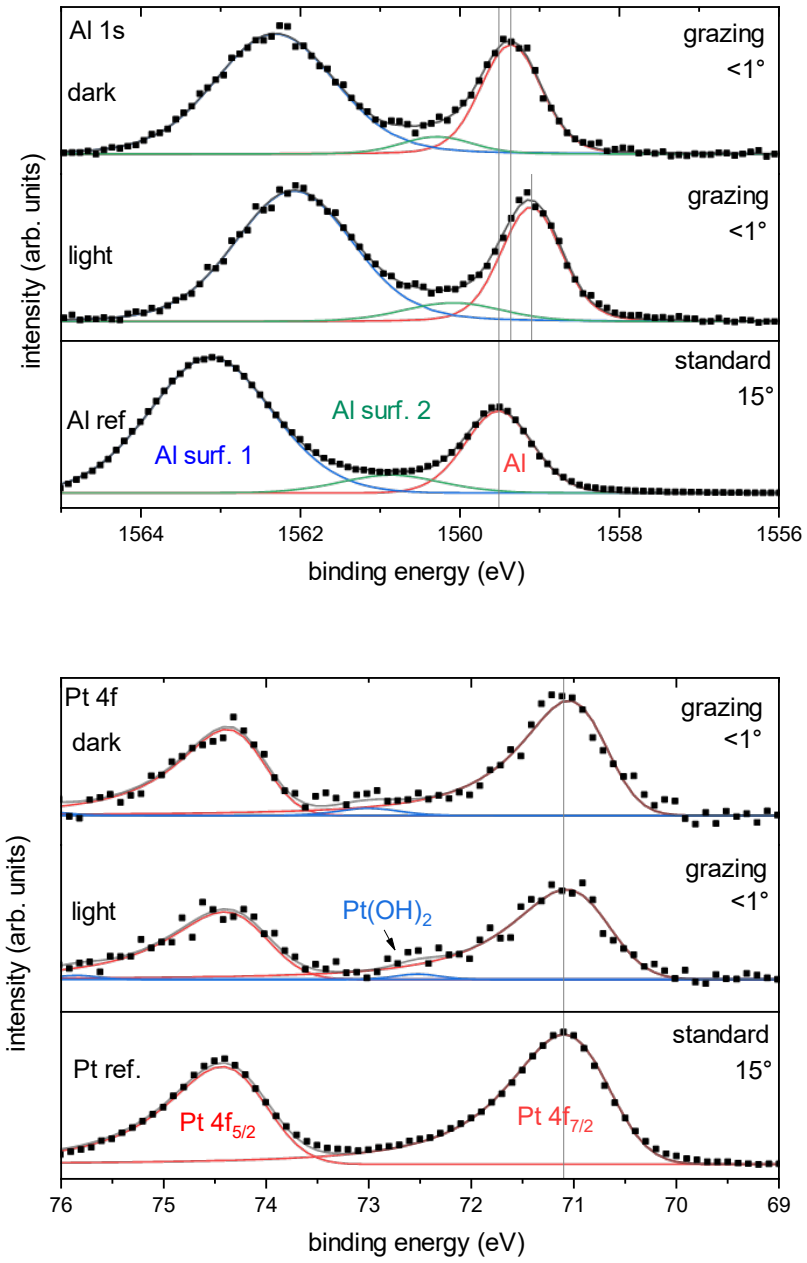

Figure C.S5. Grazing incidence spectra. Fitted spectra of Al 1s and Pt 4f under grazing incidence used in the main text. Al 1s peaks were fit with GL(30) peakshapes in CasaXPS with FWHM constraints where the Pt 4f was fit with asymmetric LA(1.2,85,70) doublets for the metallic Pt0 and GL(30) for the non-metallic $Pt(OH)_2$

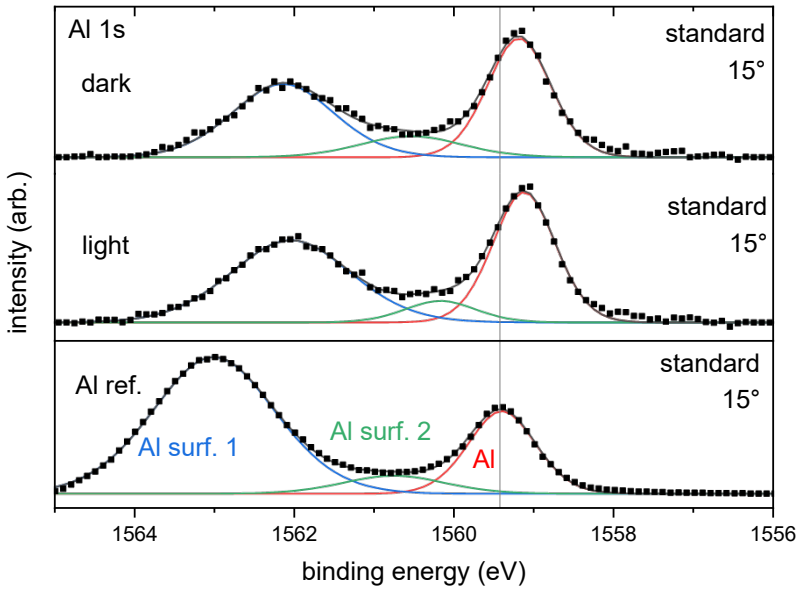

Figure C.S6. Normal incidence Al | p-Si spectra. Fitted spectra of Al 1s standard incidence used in the main text. Al 1s peaks were fit with GL(30) peakshapes in CasaXPS with FWHM constraint.

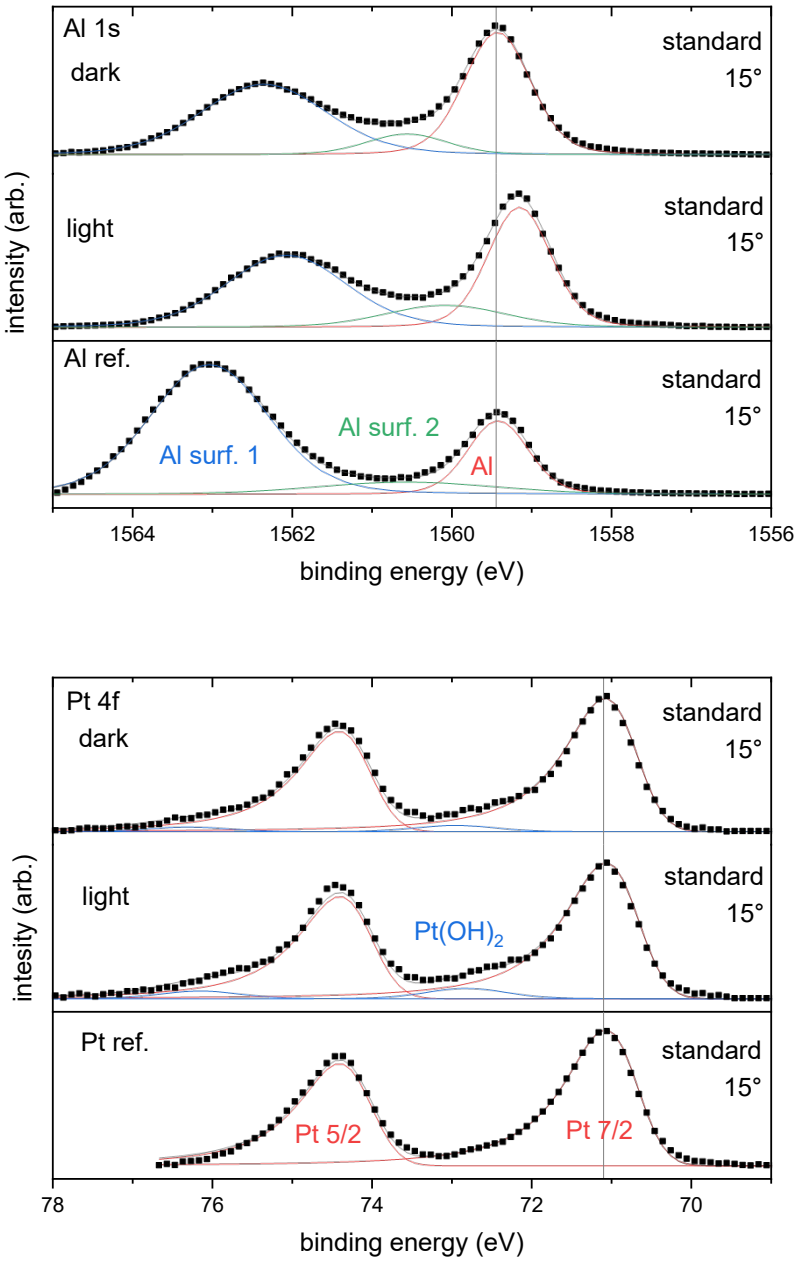

Figure C.S7. Contact pad spectra for p-Si. Fitted spectra of Al 1s and Pt 4f on p-type Si collected at the respective contact pads under standard incidence. Al 1s peaks were fit with GL(30) peakshapes in CasaXPS with FWHM constraints where the Pt 4f was fit with asymmetric LA(1.2,85,70) doublets for the metallic Pt^0 and GL(30) for the non-metallic $Pt(OH)_2$.

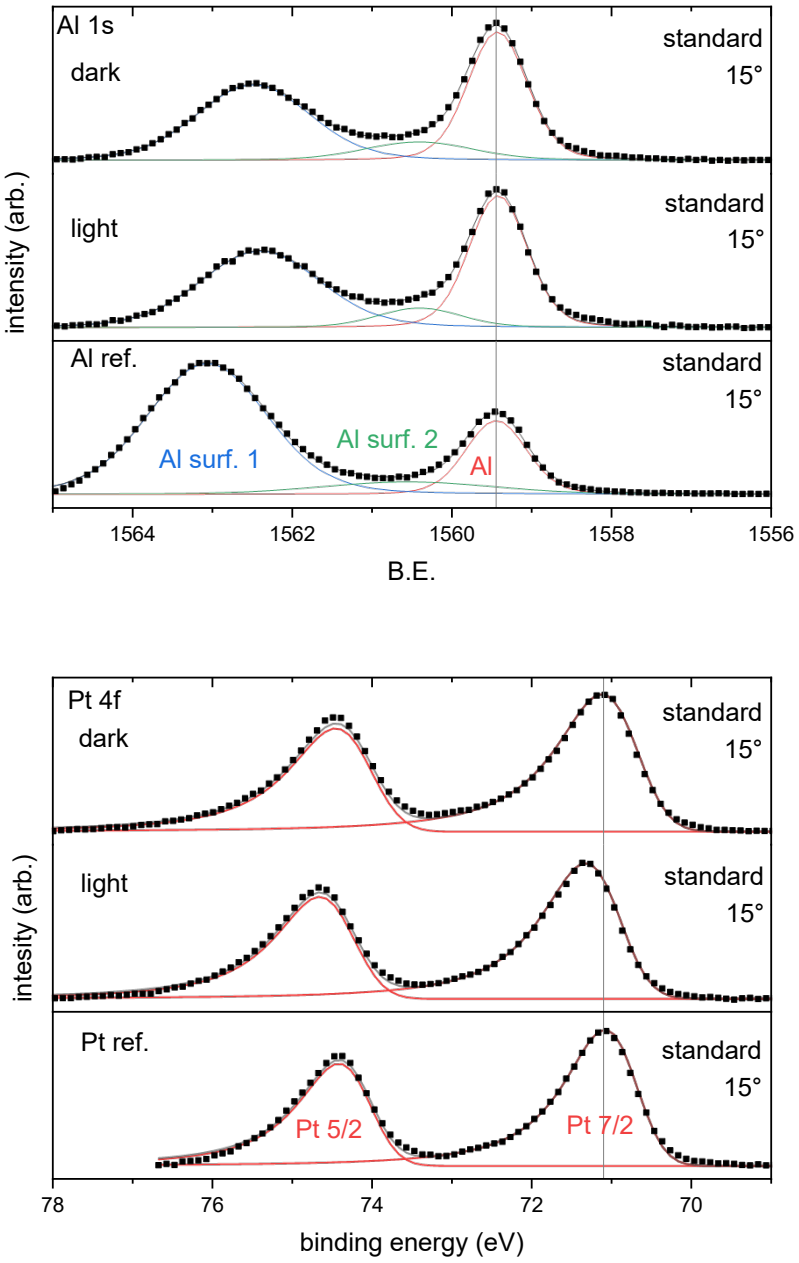

Figure C.S8. Contact pad spectra for n-Si. Fitted spectra of Al 1s and Pt 4f on n-type Si collected at the respective contact pads under standard incidence. Al 1s peaks were fit with GL(30) peakshapes in CasaXPS with FWHM constraints where the Pt 4f was fit with asymmetric LA(1.2,85,70) doublets for the metallic Pt^0 and GL(30) for the non-metallic $Pt(OH)_2$.

Appendix E. Supporting Information for Paper E

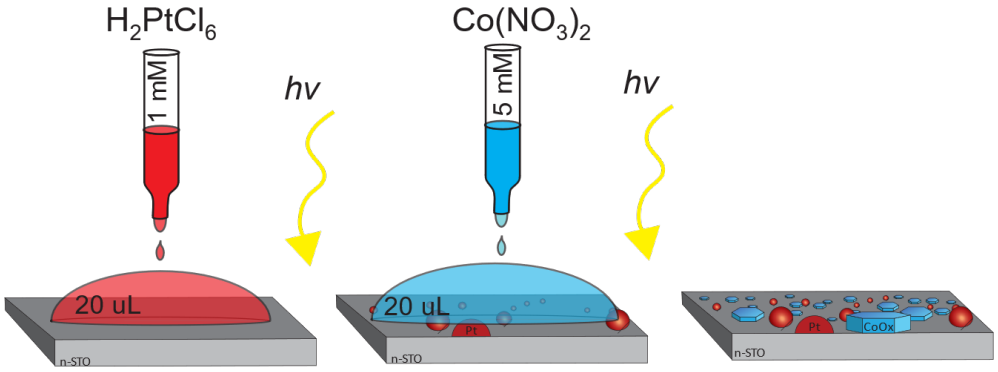

Figure E.S1. Electrocatalyst loading on n-STO. Electrocatalysts of Pt and CoOx were photodeposited from 1 mM H_2PtCl_6 and 5mM $Co(NO_3)_2$ respectively on polished surfaces of reduced STO single crystals in a sequential manner at 100% humidity to prevent the precursors from dying. 1 Sun light intensity from a solar simulator was used to photodeposit each electrocatalyst for 5 min. Following the CoOx deposition, the solution was vigorously rinsed with 18 MΩ water.

Experimental:

$SrTiO_3$ intrinsic single crystals purchased commercially from Crystal Substrates and MTI epi-polished (single side) with offcut's <0.5 Deg. Samples were then reduced in a Hydrogen furnace at 1000°C for 6 hrs. Ohmic contacts were produced by rubbing GaInEu on the unpolished face, then a wire with silver paste was used to make electrical connection. Electrodes were sealed in chemically resistant and vacuum compatible epoxy (Hysol Loctite 9460).

DWE electrode fabrication:

Pt DWE: With the sides of the epoxy masked, 40 nm Pt deposited by ebeam at 0.2 Å/s, a tinned-copper wire was then connected to the Pt thin film on the epoxy with a small amount of silver

paste, then the wire and electrode was encased again in epoxy exposing only the active area of the sample.

Co DWE: With the sides of the epoxy masked, 2 nm Co deposited by ebeam at 0.2 Å/s, Extra Co was photodeposited surface from a 1M CoCl2 buffered to 9.5 pH with K-Borate solution onto the electrode by applying +1 V vs. SCE for 90 s. The electrode was then cycled for 25 cycles at 50 mV/s in the dark then 25 cycles under 1 Sun to fully convert the cobalt film to a redox-active $Co(OH)_2$/CoOOH. A porous 10 nm Au film was then deposited by resistive heating PVD to create an ionically porous top contact and directly control the oxidation state of the catalyst film. A tinned-copper wire was then connected to the Au thin film on the epoxy with a small amount of silver paste, then the wire and electrode were encased again in epoxy exposing only the active area of the sample.

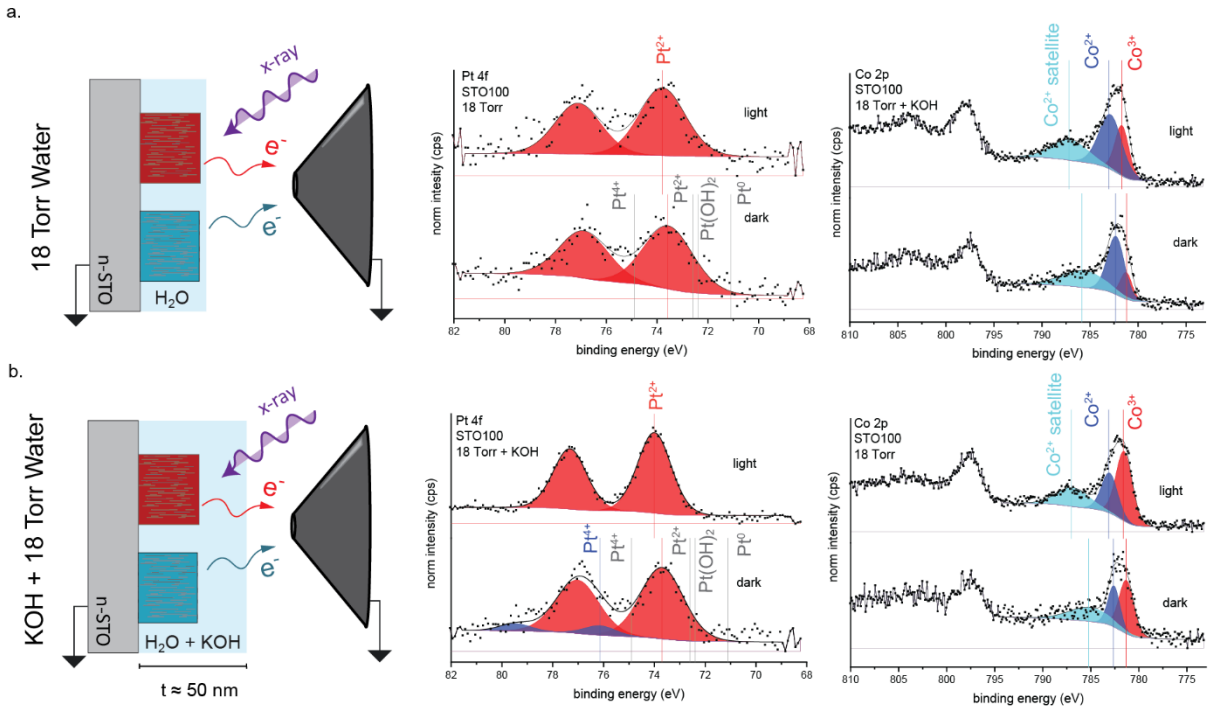

Figure E.S2. AP-XPS $SrTiO_3$ <100>. the twodiagrams at the left of the figure indicate the environmental conditions APXPS conditions 18 Torr water vapor and 20uL 0.0133 M

deliquescent KOH in 18 Torr water vapor collected at 4keV photon energy under grazing incidence (<1°). Internal gold foil was used as an energy reference for all respective atmospheric conditions. The analyzer was shorted to the Au refence and the ohmic back contact of the STO samples established with GaInEu enclosed in vacuum compatible epoxy

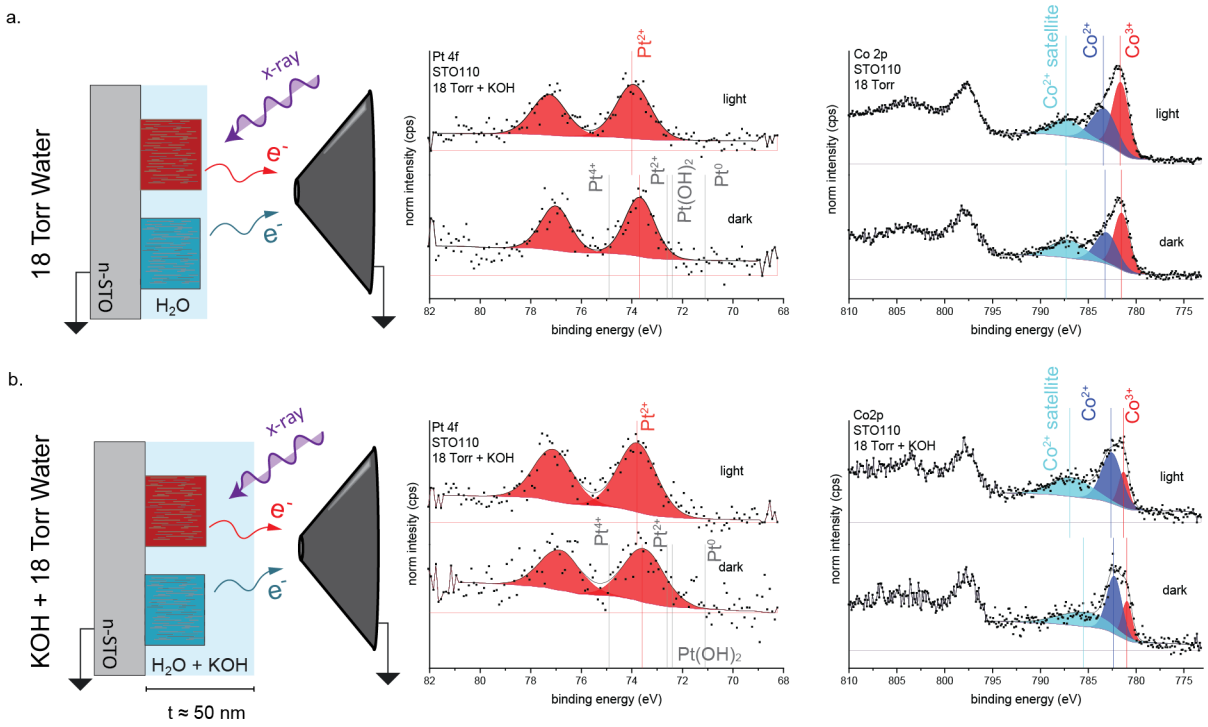

Figure E.S3. AP-XPS $SrTiO_3$ <110>. the twodiagrams at the left of the figure indicate the environmental conditions APXPS conditions 18 Torr water vapor and 20uL 0.0133 M deliquescent KOH in 18 Torr water vapor collected at 4keV photon energy under grazing incidence (<1°). Internal gold foil was used as an energy reference for all respective atmospheric conditions. The analyzer was shorted to the Au refence and the ohmic back contact of the STO samples established with GaInEu enclosed in vacuum compatible epoxy

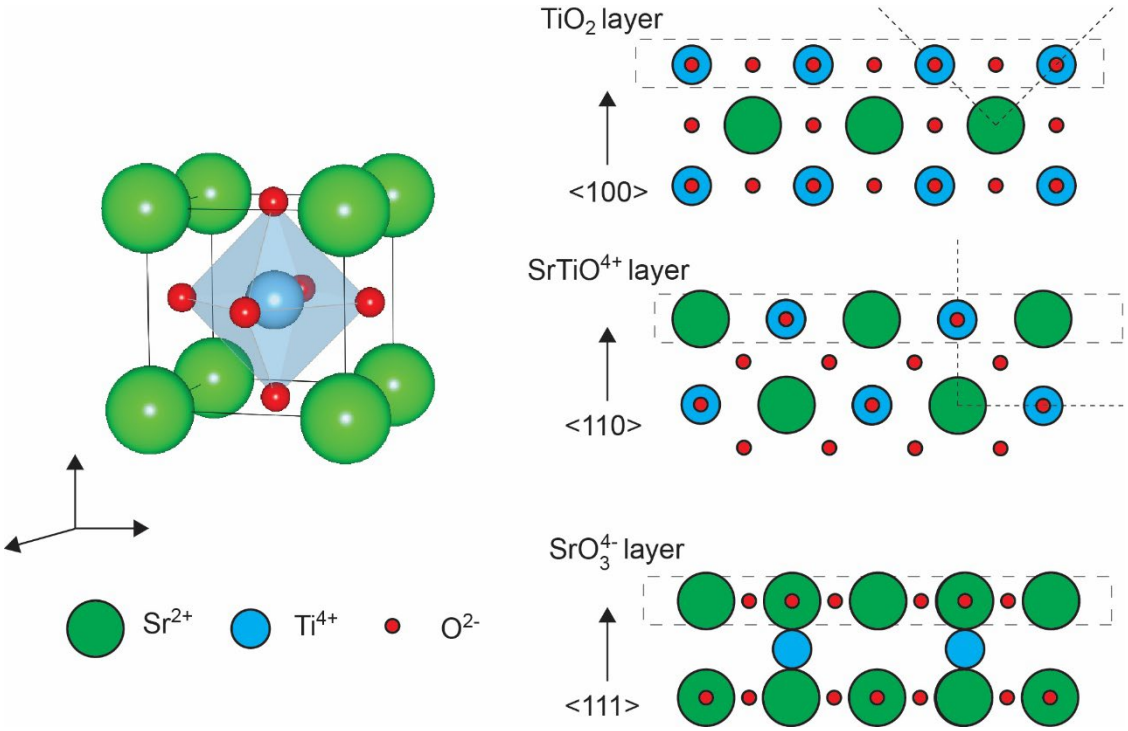

Figure E.S4: $SrTiO_3$ crystal facet termination. Unit cell and dominant crystal facet terminations.

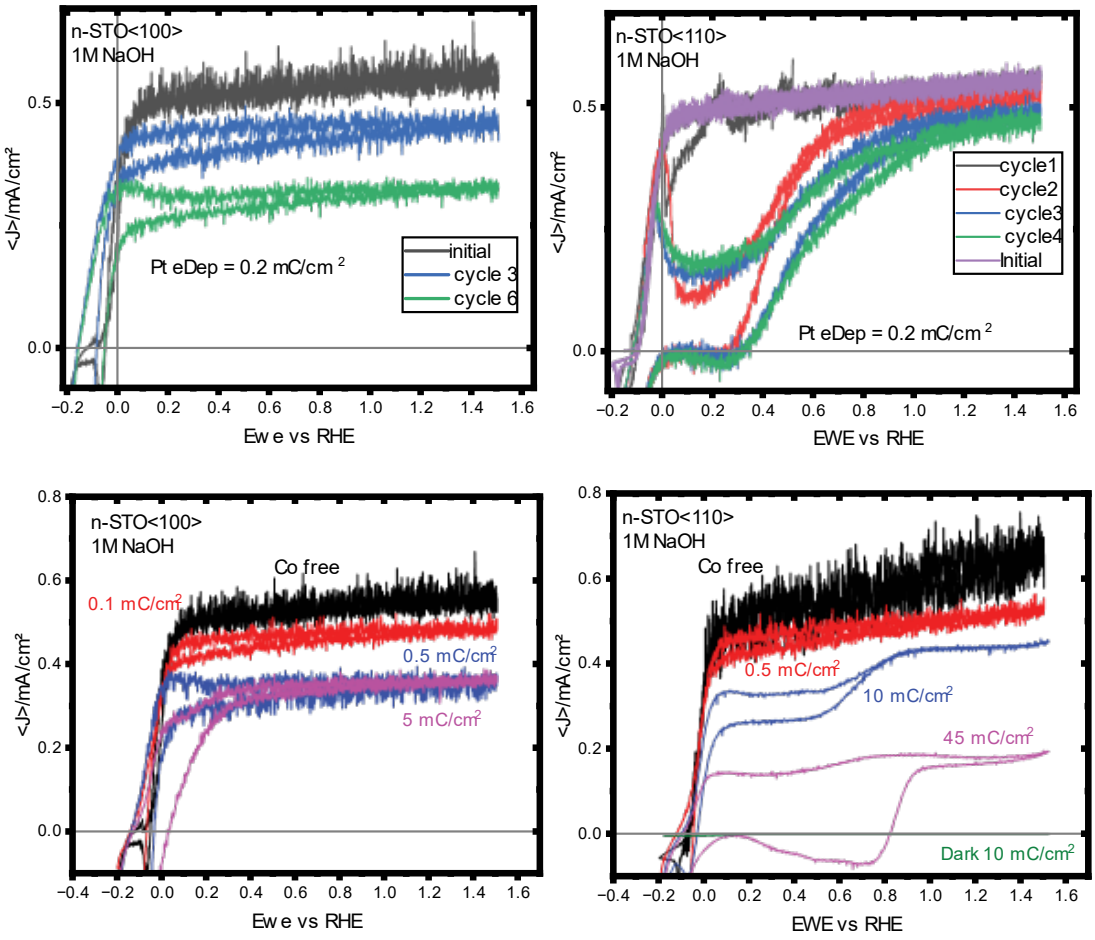

Figure E.S5. $SrTiO_3$ loading study. Reduced STO (n-STO) with crystal facet terminations of <100> and <110> were used to measure the influence of electrodeposition on CV characteristics in 1 M NaOH, sparged with Ag and stirred. (initial = before electrocatalyst deposition). 0.2 mC/cm^2 charge was passed to reduce Pt onto each crystal from a freshly prepared 1 mM H_2PtCl_6 solution. Each crystal shows similar behavior in the early cycles but differ at later cycles. We attribute the changes in the <100> sample to be caused by either an internal shunt (Oxidation and reduction on the same surface, current not measured by the potentiostat) or by electrocatalyst migration and agglomeration causing increased light blocking. For the <110> crystal, a reduction wave is observed to grow in after successive cycling, attributed to the reduction of oxidized platinum. Finally, the Co loading studies, reduced from borate buffered $CoCl_2$ solution deposited increasing amounts of CoOx on the surface, indicated by the charge passed. The plots show the stable CV's, after approximately 5 cycles. With increasing cycle, a partial blocking of the light is observed, in agreement with effective medium theory. Additionally, the effect of two parallel junctions was observed near 0.8 V in the <110> electrode and 0.4 V in the <100> electrode. We propose this illustrates the electrolyte|n-STO interface at lower potentials, and the addition of a CoOx|n-STO interface at more oxidizing potentials.

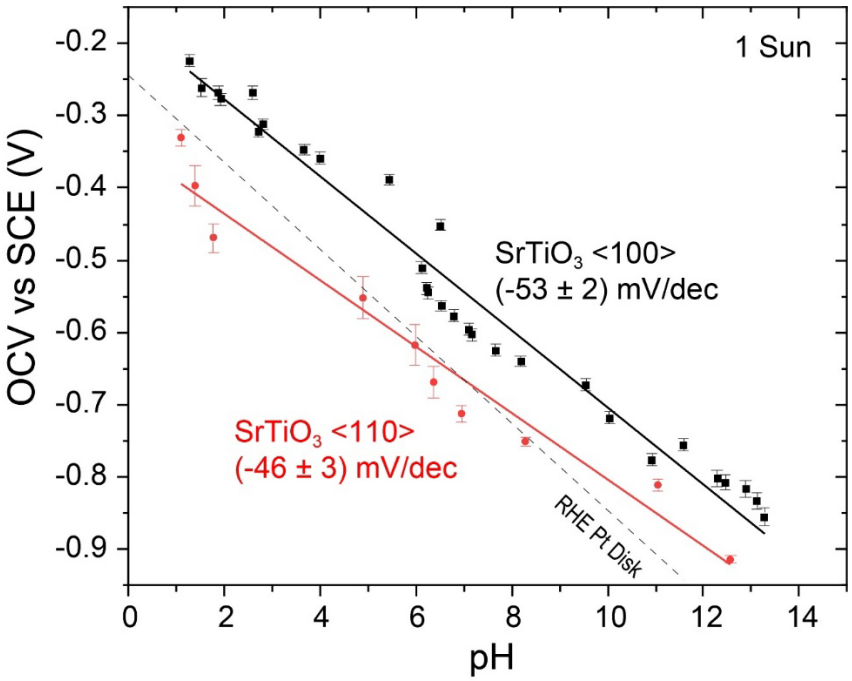

Figure E.S6. n-STO Voc vs pH study. 1M NaOH was titrated into 40 ml of 0.25 M HCl and 0.25 M H_3PO_4 to vary the solution pH. Under solar simulated light, at 1 Sun equivalent intensity, CV's were used to measure the open circuit voltage (OCV) vs the SCE reference electrode.

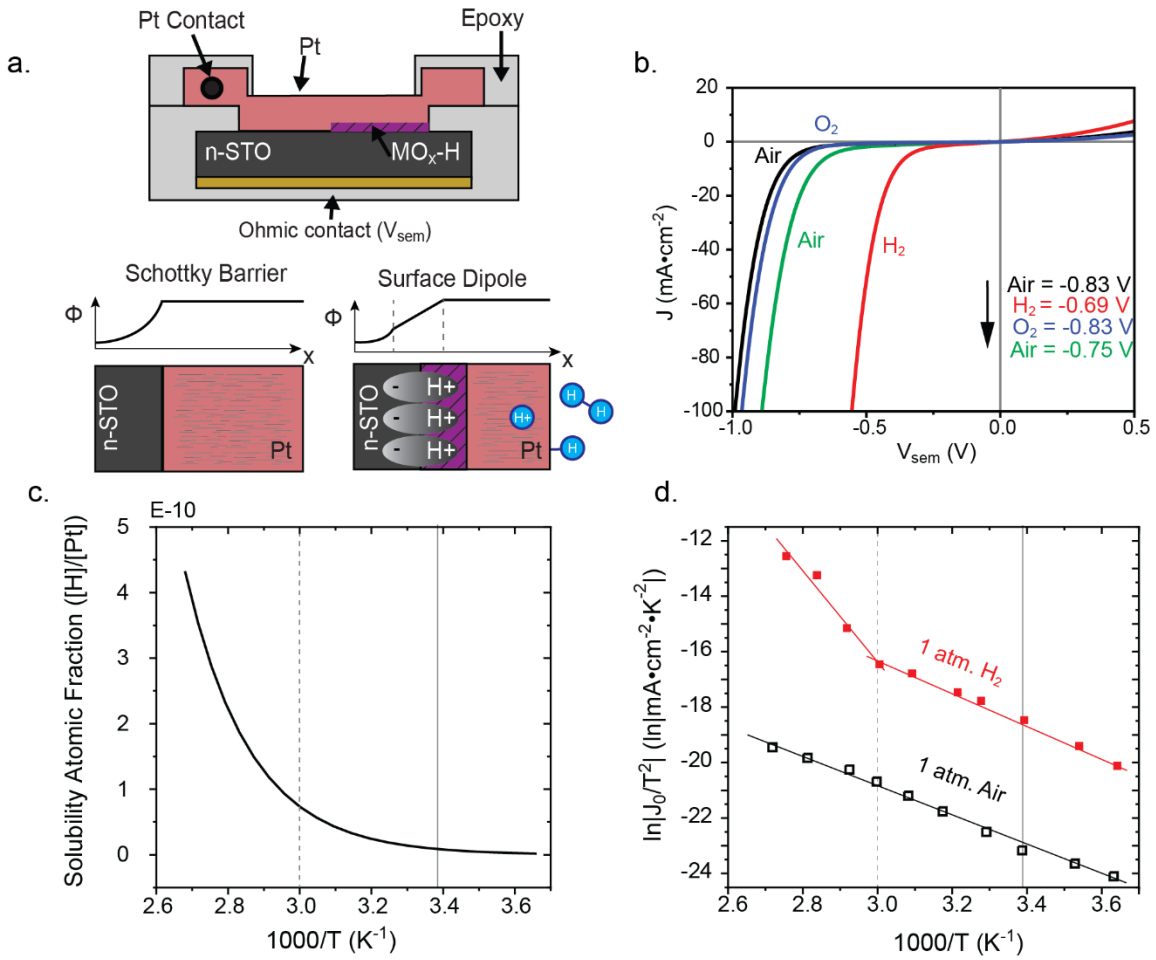

Figure E.S7. Pt|n-STO in hydrogen atmosphere. (a) diagram of the thin film Pt|n-SrTiO3 <100> device and a hypothesis for interfacial barrier lowering due to a surface dipole created from absorbed protons. J/V experiments for the Pt|n-SrTiO3 under various gas atmosphere conditions at room temperature. Richardson plot in 1 atmosphere of hydrogen and in air as a function on 1/T. These data show that at low temperatures In figure b is plotted the solubility atomic fraction of Protons in Pt at temperatures matching that of the Richardson plot (a), solid vertical line indicates room temperature whereas the dashed line indicates a transition temperature in Hydrogen atmosphere.

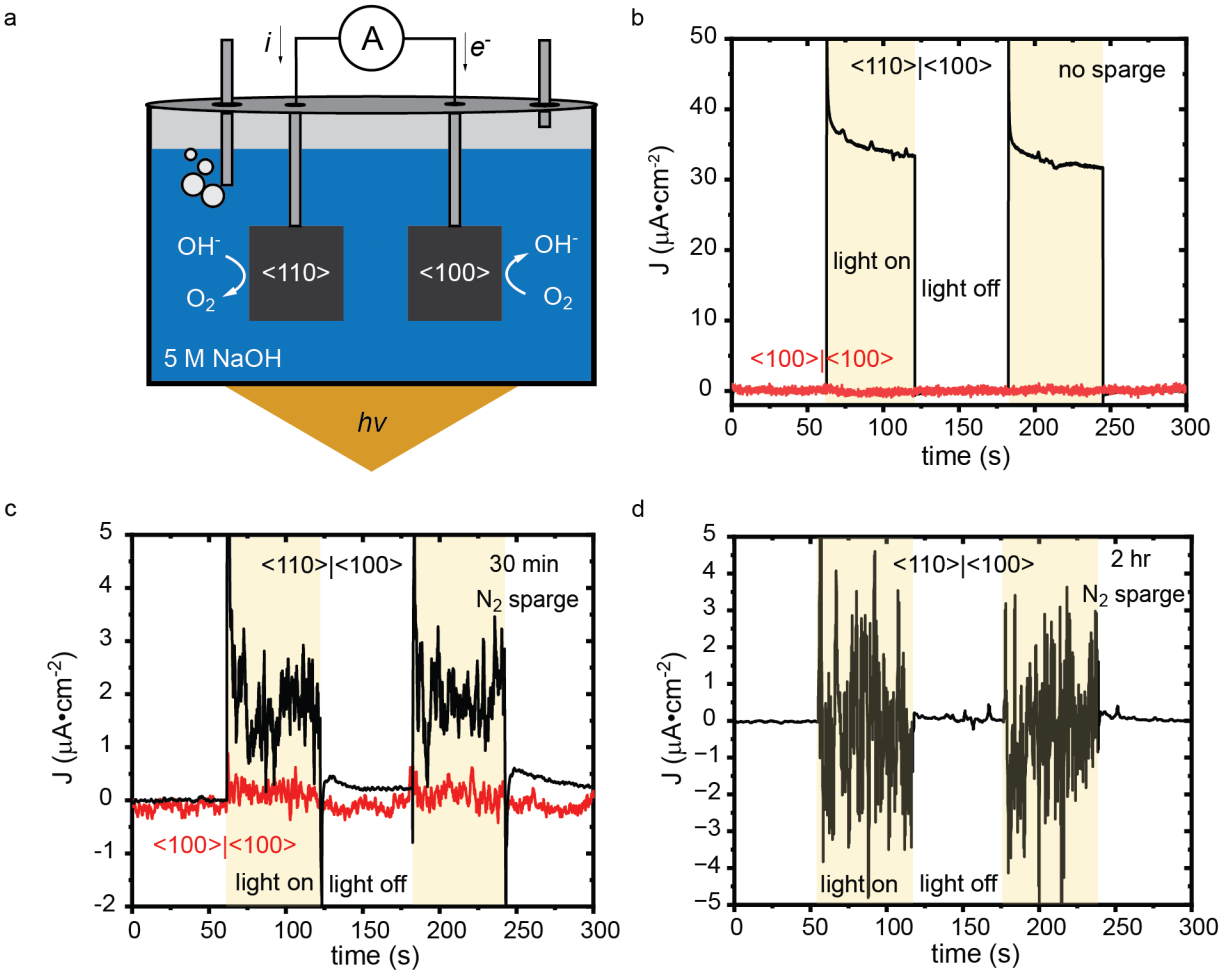

Figure S8: Two electrode crystal facet charge selectivity

Panel A shows a diagram of the experimental set up for the two electrode experiments (n-STO 100 and 110 shown). Reduced single crystals were annealed together and had similar exposed areas after being fabricated into electrodes. Solar simulated light at 1 sun intensity was used in the chopped chronoamperometric studies in 5 M NaOH (b-d) with increasing nitrogen sparging time to remove dissolved gases.

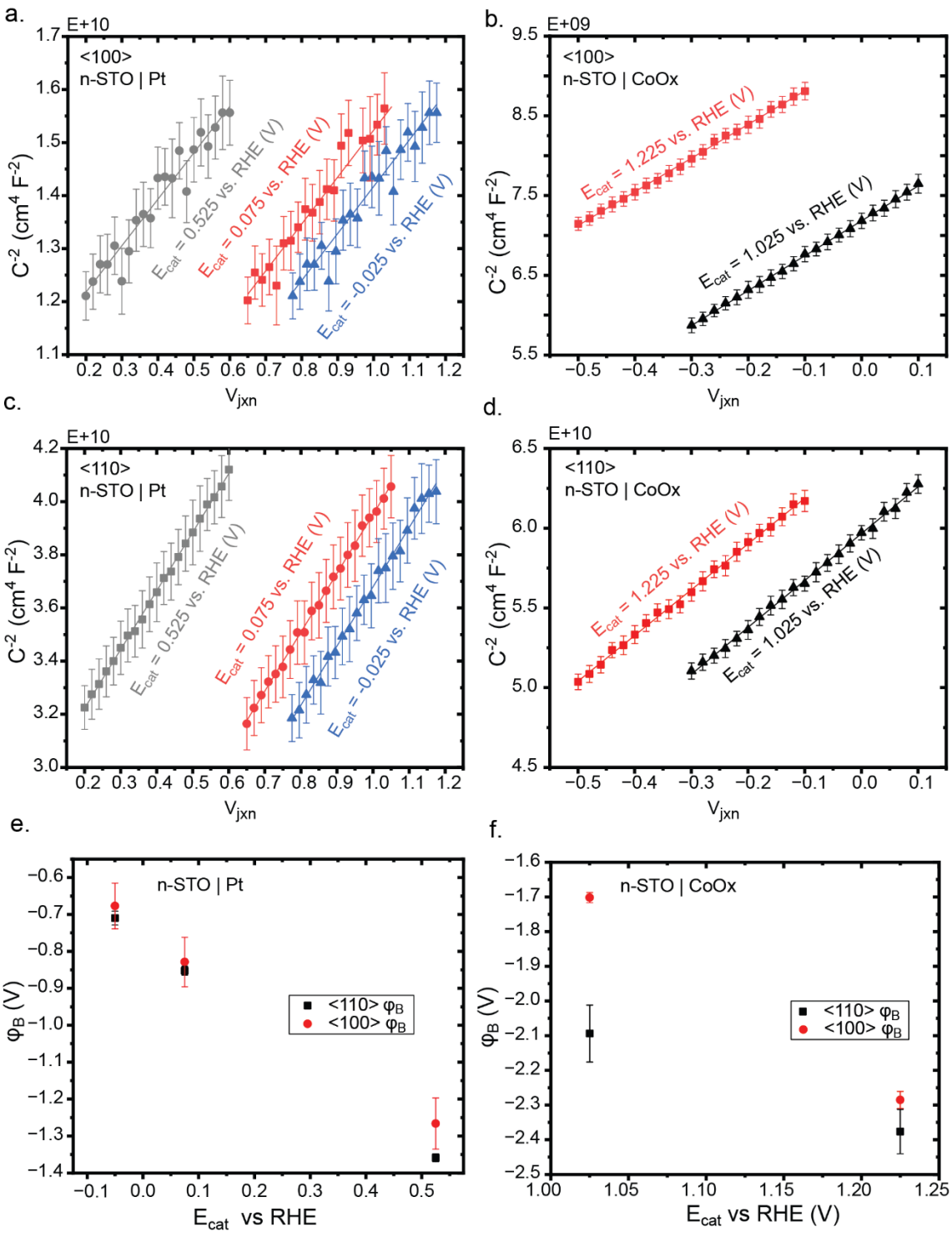

Figure S9: DWE Mott-Schottky results

Panels a - d display Mott-Schottky plots measured in the dual working electrode experiment in 1 M NaOH at 0.525, 0.075 and -0.025 V vs. RHE for the n-STO|Pt junctions (a <100>, c <110>) and at 1.025 and 1.225 V vs. RHE for the n-STO|CoOx junctions (b <100>, d <110>). Panels e and f display the calculated barrier heights for the n-STO|Pt and n-STO|CoOx junctions respectively.

References Cited:

References for Paper A:

Style: Nature Catalysis

1 Li, J. & Wu, N. Semiconductor-based photocatalysts and photoelectrochemical cells for solar fuel generation: a review. *Catalysis Science & Technology* **5**, 1360-1384, doi:10.1039/C4CY00974F (2015).

2 Chen, S., Takata, T. & Domen, K. Particulate photocatalysts for overall water splitting. *Nature Reviews Materials* **2**, 17050, doi:10.1038/natrevmats.2017.50 (2017).

3 Nozik, A. J. Photoelectrochemistry: Applications to Solar Energy Conversion. *Annual Review of Physical Chemistry* **29**, 189-222, doi:10.1146/annurev.pc.29.100178.001201 (1978).

4 Boettcher, S. W. *et al.* Photoelectrochemical Hydrogen Evolution Using Si Microwire Arrays. *Journal of the American Chemical Society* **133**, 1216-1219, doi:10.1021/ja108801m (2011).

5 Weber, M. F. & Dignam, M. J. Efficiency of Splitting Water with Semiconducting Photoelectrodes. *Journal of The Electrochemical Society* **131**, 1258-1265, doi:10.1149/1.2115797 (1984).

6 Marcus, R. A. Chemical and Electrochemical Electron-Transfer Theory. *Annual Review of Physical Chemistry* **15**, 155-196, doi:10.1146/annurev.pc.15.100164.001103 (1964).

7 Marcus, R. A. & Sutin, N. Electron transfers in chemistry and biology. *Biochimica et Biophysica Acta (BBA) - Reviews on Bioenergetics* **811**, 265-322, doi:10.1016/0304-4173(85)90014-X (1985).

8 Fajardo, A. M. & Lewis, N. S. Rate Constants for Charge Transfer Across Semiconductor-Liquid Interfaces. *Science* **274**, 969-972, doi:10.1126/science.274.5289.969 (1996).

9 Lewis, N. S. Chemical Control of Charge Transfer and Recombination at Semiconductor Photoelectrode Surfaces. *Inorg. Chem.* **44**, 6900-6911, doi:10.1021/ic051118p (2005).

10 Memming, R. in *Semiconductor Electrochemistry* 127-168 (Wiley-VCH Verlag GmbH & Co. KGaA, 2015).

11 Moore, C. C. Ergodic theorem, ergodic theory, and statistical mechanics. *Proceedings of the National Academy of Sciences* **112**, 1907-1911, doi:10.1073/pnas.1421798112 (2015).

12 Hisatomi, T., Kubota, J. & Domen, K. Recent advances in semiconductors for photocatalytic and photoelectrochemical water splitting. *Chemical Society Reviews* **43**, 7520-7535, doi:10.1039/C3CS60378D (2014).

13 Ager, J. W., Shaner, M. R., Walczak, K. A., Sharp, I. D. & Ardo, S. Experimental demonstrations of spontaneous, solar-driven photoelectrochemical water splitting. *Energy Environ. Sci.* **8**, 2811-2824, doi:10.1039/C5EE00457H (2015).

14 Chen, Z. *et al.* Accelerating materials development for photoelectrochemical hydrogen production: Standards for methods, definitions, and reporting protocols. *J. Mater. Res.* **25**, 3-16, doi:10.1557/JMR.2010.0020 (2010).
15 Laskowski, F. A. L., Nellist, M. R., Qiu, J. & Boettcher, S. W. Metal Oxide/(oxy)hydroxide Overlayers as Hole Collectors and Oxygen-Evolution Catalysts on Water-Splitting Photoanodes. *Journal of the American Chemical Society* **141**, 1394-1405, doi:10.1021/jacs.8b09449 (2019).
16 Lyon, L. A. & Hupp, J. T. Energetics of the nanocrystalline titanium dioxide/aqueous solution Interface: Approximate conduction band edge variations between $H_0 = -10$ and $H^- = +26$. *J. Phys. Chem. B* **103**, 4623-4628, doi:10.1021/jp9908404 (1999).
17 Lichterman, M. F. *et al.* Direct observation of the energetics at a semiconductor/liquid junction by operando X-ray photoelectron spectroscopy. *Energy & Environmental Science* **8**, 2409-2416, doi:10.1039/c5ee01014d (2015).
18 Peper, J. L., Gentry, N. E., Boudy, B. & Mayer, J. M. Aqueous TiO2 Nanoparticles React by Proton-Coupled Electron Transfer. *Inorg. Chem.* **61**, 767-777, doi:10.1021/acs.inorgchem.1c03125 (2022).
19 Kautek, W. & Gerischer, H. Photoelectrochemical reactions and formation of inversion layers at n-type MoS_2, $MoSe_2$, and WSe_2 electrodes in aprotic solvents. *Ber. Bunsen-Ges. Phys. Chem.* **84**, 645-653, doi:10.1002/bbpc.19800840708 (1980).
20 Jaeger, C. D., Gerischer, H. & Kautek, W. Formation of an Inversion Layer in n-Type MoSe2 Electrodes: Observation in the Presence of Highly Oxidizing Redox Systems. *Berichte der Bunsengesellschaft für physikalische Chemie* **86**, 20-25, doi:10.1002/bbpc.19820860105 (1982).
21 Royea, W. J., Michalak, D. J. & Lewis, N. S. Role of inversion layer formation in producing low effective surface recombination velocities at Si/liquid contacts. *Applied Physics Letters* **77**, 2566-2568, doi:10.1063/1.1318935 (2000).
22 Grimm, R. L. *et al.* Comparison of the Photoelectrochemical Behavior of H-Terminated and Methyl-Terminated Si(111) Surfaces in Contact with a Series of One-Electron, Outer-Sphere Redox Couples in CH3CN. *The Journal of Physical Chemistry C* **116**, 23569-23576, doi:10.1021/jp308461q (2012).
23 Gstrein, F., Michalak, D. J., Knapp, D. W. & Lewis, N. S. Near-Surface Channel Impedance Measurements, Open-Circuit Impedance Spectra, and Differential Capacitance vs Potential Measurements of the Fermi Level Position at Si/CH3CN Contacts. *The Journal of Physical Chemistry C* **111**, 8120-8127, doi:10.1021/jp066226r (2007).
24 Sze, S. M. & Ng, K. K. *Physics of semiconductor devices*. (John Wiley & Sons, Inc., 2006).
25 Park, K.-W. & Kolpak, A. M. Optimal methodology for explicit solvation prediction of band edges of transition metal oxide photocatalysts. *Commun Chem* **2**, 1-10, doi:10.1038/s42004-019-0179-3 (2019).
26 Trasatti, S. The absolute electrode potential: an explanatory note *Pure Appl. Chem.* **58**, 955-966, doi:10.1351/pac198658070955 (1986).
27 Michalak, D. J. & Lewis, N. S. Use of near-surface channel conductance and differential capacitance versus potential measurements to correlate inversion layer formation with low effective surface recombination velocities at *n*-Si/liquid contacts. *Appl. Phys. Lett.* **80**, 4458-4460, doi:10.1063/1.1479456 (2002).

28 Turner, J. A., Manassen, J. & Nozik, A. J. Photoelectrochemistry with *p*-Si electrodes: Effects of inversion. *Appl. Phys. Lett.* **37**, 488-491, doi:10.1063/1.91741 (1980).
29 Keller, N. D. *et al.* Multi-Electron Transfer at H-Terminated p-Si Electrolyte Interfaces: Large Photovoltages under Inversion Conditions. *Journal of the American Chemical Society* **145**, 11282-11292, doi:10.1021/jacs.3c01990 (2023).
30 Bard, A. J., Bocarsly, A. B., Fan, F. R. F., Walton, E. G. & Wrighton, M. S. The concept of Fermi level pinning at semiconductor/liquid junctions. Consequences for energy conversion efficiency and selection of useful solution redox couples in solar devices. *Journal of the American Chemical Society* **102**, 3671-3677, doi:10.1021/ja00531a001 (1980).
31 Bocarsly, A. B., Bookbinder, D. C., Dominey, R. N., Lewis, N. S. & Wrighton, M. S. Photoreduction at illuminated p-type semiconducting silicon photoelectrodes. Evidence for Fermi level pinning. *Journal of the American Chemical Society* **102**, 3683-3688, doi:10.1021/ja00531a003 (1980).
32 Spitler, M. T. Impedance analysis of semiconductor electrodes in the accumulation region. *Sustainable Energy & Fuels*, doi:10.1039/D3SE00786C (2023).
33 Hofstein, S. R. & Warfield, G. Physical limitations on the frequency response of a semiconductor surface inversion layer. *Solid-State Electronics* **8**, 321-341, doi:10.1016/0038-1101(65)90148-6 (1965).
34 Madou, M. J., Loo, B. H., Frese, K. W. & Morrison, S. R. Bulk and surface characterization of the silicon electrode. *Surface Science* **108**, 135-152, doi:10.1016/0039-6028(81)90363-0 (1981).
35 Cooper, G., Turner, J. A. & Nozik, A. J. Mott-Schottky Plots and Flatband Potentials for Single Crystal Rutile Electrodes. *Journal of The Electrochemical Society* **129**, 1973-1977, doi:10.1149/1.2124334 (1982).
36 Thapar, R. & Rajeshwar, K. Mott—Schottky analyses on n- and p-GaAs/room temperature chloroaluminate molten-salt interfaces. *Electrochimica Acta* **28**, 195-198, doi:10.1016/0013-4686(83)85109-3 (1983).
37 Bardwell, J. A., Draper, N. & Schmuki, P. Growth and characterization of anodic oxides on Si(100) formed in 0.1 M hydrochloric acid. *Journal of Applied Physics* **79**, 8761-8769, doi:10.1063/1.362502 (1996).
38 Huygens, I. M. & Strubbe, K. Electrochemical Impedance Study of the Germanium/Electrolyte Interface. *Journal of The Electrochemical Society* **155**, F49, doi:10.1149/1.2837847 (2008).
39 La Mantia, F., Habazaki, H., Santamaria, M. & Di Quarto, F. A critical assessment of the Mott-Schottky analysis for the characterisation of passive film-electrolyte junctions. *Russ J Electrochem* **46**, 1306-1322, doi:10.1134/S102319351011011X (2010).
40 Molto, C., Etcheberry, A., Grand, P. P. & Goncalves, A. M. Study of Photo-Oxidized n-Type Textured Silicon Surface through Electrochemical Impedance Spectroscopy. *Journal of The Electrochemical Society* **167**, 146505, doi:10.1149/1945-7111/abc0a6 (2020).
41 Würfel, P. & Würfel, U. *Physics of solar cells: from basic principles to advanced concepts*. 3rd edition edn, (Wiley-VCH Verlag GmbH & Co. KGaA, 2016).
42 Roe, E. T., Egelhofer, K. E. & Lonergan, M. C. Limits of Contact Selectivity/Recombination on the Open-Circuit Voltage of a Photovoltaic. *ACS Applied Energy Materials* **1**, 1037-1046, doi:10.1021/acsaem.7b00179 (2018).

43 Pan, Z. *et al.* Elucidating charge separation in particulate photocatalysts using nearly intrinsic semiconductors with small asymmetric band bending. *Sustainable Energy & Fuels* **3**, 850-864, doi:10.1039/C9SE00036D (2019).
44 Pan, Z. *et al.* Mutually-dependent kinetics and energetics of photocatalyst/co-catalyst/two-redox liquid junctions. *Energy Environ. Sci.* **13**, 162-173, doi:10.1039/C9EE02910A (2020).
45 Liu, T. *et al.* A general interfacial-energetics-tuning strategy for enhanced artificial photosynthesis. *Nat Commun* **13**, 7783, doi:10.1038/s41467-022-35502-z (2022).
46 Chen, X., Liu, L., Yu, P. Y. & Mao, S. S. Increasing Solar Absorption for Photocatalysis with Black Hydrogenated Titanium Dioxide Nanocrystals. *Science* **331**, 746-750, doi:10.1126/science.1200448 (2011).
47 Gerischer, H. On the stability of semiconductor electrodes against photodecomposition. *Journal of Electroanalytical Chemistry and Interfacial Electrochemistry* **82**, 133-143, doi:10.1016/S0022-0728(77)80253-2 (1977).
48 Yu, W. Understanding the stability of semiconducting photocathodes for solar water splitting. *Current Opinion in Electrochemistry* **39**, 101262, doi:10.1016/j.coelec.2023.101262 (2023).
49 Zhao, T. *et al.* A coating strategy to achieve effective local charge separation for photocatalytic coevolution. *Proceedings of the National Academy of Sciences* **118**, e2023552118, doi:10.1073/pnas.2023552118 (2021).
50 Shen, X. *et al.* Tuning Intermediate Bands of Protective Coatings to Reach the Bulk-Recombination Limit of Stable Water-Oxidation GaP Photoanodes. *Advanced Energy Materials* **12**, 2201314, doi:10.1002/aenm.202201314 (2022).
51 Shen, X. *et al.* Comprehensive Evaluation for Protective Coatings: Optical, Electrical, Photoelectrochemical, and Spectroscopic Characterizations. *Frontiers in Energy Research* **9**, doi:10.3389/fenrg.2021.799776 (2022).

References cited in Paper B:

B.a. Main text:
Style: ACS Energy Letters

1. Heller, A.; Vadimsky, R. G., Efficient Solar to Chemical Conversion: 12% Efficient Photoassisted Electrolysis in the [p-Type InP(Ru)]/HCl-KCl/Pt(Rh) Cell. *Phys. Rev. Lett.* **1981,** *46* (17), 1153-1156.
2. Heller, A.; Aharon-Shalom, E.; Bonner, W. A.; Miller, B., Hydrogen-Evolving Semiconductor Photocathodes: Nature of the Junction and Function of the Platinum Group Metal Catalyst. *J. Am. Chem. Soc.* **1982,** *104* (25), 6942-6948.
3. Aspnes, D. E.; Heller, A., Photoelectrochemical Hydrogen Evolution and Water Photolyzing Semiconductor Suspensions: Properties of Platinum Group Metal Catalyst-Semiconductor Contacts in Air and in Hydrogen. *J. Phys. Chem.* **1983,** *87* (24), 4919-4929.
4. Trasatti, S., Work Function, Electronegativity, and Electrochemical Behaviour of Metals: III. Electrolytic Hydrogen Evolution in Acid Solutions. *Journal of Electroanalytical Chemistry and Interfacial Electrochemistry* **1972,** *39* (1), 163-184.
5. Sze, S. M.; Ng, K. K., *Physics of Semiconductor Devices: Sze/Physics*. John Wiley & Sons, Inc.: Hoboken, NJ, USA, 2006.
6. Lewerenz, H. J., Semiconductor Surface Transformations for Photoelectrochemical Energy Conversion. *J. Electrochem. Soc.* **2014,** *161* (13), H3117.
7. Lee, M. H.; Takei, K.; Zhang, J.; Kapadia, R.; Zheng, M.; Chen, Y. Z.; Nah, J.; Matthews, T. S.; Chueh, Y. L.; Ager, J. W.; Javey, A., P-Type InP Nanopillar Photocathodes for Efficient Solar-Driven Hydrogen Production. *Angew. Chem. Int. Ed.* **2012,** *51* (43), 10760-10764.
8. Nunez, P.; Cabán-Acevedo, M.; Yu, W.; Richter, M. H.; Kennedy, K.; Villarino, A. M.; Brunschwig, B. S.; Lewis, N. S., Origin of the Electrical Barrier in Electrolessly Deposited Platinum Nanoparticles on P-Si Surfaces. *J. Phys. Chem. C* **2021,** *125* (32), 17660-17670.
9. Hollinger, G.; Bergignat, E.; Joseph, J.; Robach, Y., On the Nature of Oxides on InP Surfaces. *Journal of Vacuum Science & Technology A* **1985,** *3* (6), 2082-2088.
10. Hofmann, A.; Streubel, P.; Meisel, A., XPS Investigation of Oxide Films on InP(100). *Surf. Interface Anal.* **1988,** *12* (5), 315-319.
11. Faur, M.; Faur, M.; Jayne, D. T.; Goradia, M.; Goradia, C., XPS Investigation of Anodic Oxides Grown on P-Type InP. *Surface and Interface Analysis* **1990,** *15* (11), 641-650.
12. Pakes, A.; Skeldon, P.; Thompson, G. E.; Hussey, R. J.; Moisa, S.; Sproule, G. I.; Landheer, D.; Graham, M. J., Composition and Growth of Anodic and Thermal Oxides on InP and GaAs. *Surface and Interface Analysis* **2002,** *34* (1), 481-484.
13. van Dorp, D. H.; Cuypers, D.; Arnauts, S.; Moussa, A.; Rodriguez, L.; De Gendt, S., Wet Chemical Etching of InP for Cleaning Applications: II. Oxide Removal. *ECS J. Solid State Sci. Technol.* **2013,** *2* (4), P190.
14. Goryachev, A.; Gao, L.; van Veldhoven, R. P. J.; Haverkort, J. E. M.; Hofmann, J. P.; Hensen, E. J. M., On the Origin of the Photocurrent of Electrochemically Passivated P-InP(100) Photoelectrodes. *Phys. Chem. Chem. Phys.* **2018,** *20* (20), 14242-14250.

15. Hussey, R. J.; Sproule, G. I.; McCaffrey, J. P.; Graham, M. J., Characterization of Oxides Formed on InP, InGaAs, InAlAs, and InGaAs/InAlAs Heterostructures at 300–500°C. *Oxidation of Metals* **2002,** *57* (5), 427-447.
16. Wurfel, U.; Cuevas, A.; Wurfel, P., Charge Carrier Separation in Solar Cells. *IEEE J. Photovoltaics* **2015,** *5* (1), 461-469.
17. Leibovitch, M.; Kronik, L.; Fefer, E.; Korobov, V.; Shapira, Y., Constructing Band Diagrams of Semiconductor Heterojunctions. *Appl. Phys. Lett.* **1995,** *66* (4), 457-459.
18. Laskowski, F. A. L.; Oener, S. Z.; Nellist, M. R.; Gordon, A. M.; Bain, D. C.; Fehrs, J. L.; Boettcher, S. W., Nanoscale Semiconductor/Catalyst Interfaces in Photoelectrochemistry. *Nature Mater* **2020,** *19* (1), 69-76.
19. Tung, R. T., Electron Transport of Inhomogeneous Schottky Barriers. *Appl. Phys. Lett.* **1991,** *58* (24), 2821-2823.
20. Tung, R. T., Electron Transport at Metal-Semiconductor Interfaces: General Theory. *Phys. Rev. B* **1992,** *45* (23), 13509-13523.
21. Tung, R. T., The Physics and Chemistry of the Schottky Barrier Height. *Applied Physics Reviews* **2014,** *1* (1), 011304.
22. Khaselev, O.; Turner, J. A., A Monolithic Photovoltaic-Photoelectrochemical Device for Hydrogen Production via Water Splitting. *Science* **1998,** *280* (5362), 425-427.
23. Young, J. L.; Steiner, M. A.; Döscher, H.; France, R. M.; Turner, J. A.; Deutsch, T. G., Direct Solar-to-Hydrogen Conversion via Inverted Metamorphic Multi-Junction Semiconductor Architectures. *Nature Energy* **2017,** *2* (4), 1-8.
24. Takata, T.; et al., Photocatalytic water splitting with a quantum efficiency of almost unity. *Nature* **2020,** *581*, 411-414.
25. Yu, W.; Richter, M. H.; Buabthong, P.; Moreno-Hernandez, I. A.; Read, C. G.; Simonoff, E.; Brunschwig, B. S.; Lewis, N. S., Investigations of the Stability of Etched or Platinized P-InP(100) Photocathodes for Solar-Driven Hydrogen Evolution in Acidic or Alkaline Aqueous Electrolytes. *Energy & Environmental Science* **2021**.
26. Nishiyama, H.; Yamada, T.; Nakabayashi, M.; Maehara, Y.; Yamaguchi, M.; Kuromiya, Y.; Nagatsuma, Y.; Tokudome, H.; Akiyama, S.; Watanabe, T.; Narushima, R.; Okunaka, S.; Shibata, N.; Takata, T.; Hisatomi, T.; Domen, K., Photocatalytic Solar Hydrogen Production from Water on a 100-m2 Scale. *Nature* **2021,** *598* (7880), 304-307.
27. Roe, E. T.; Egelhofer, K. E.; Lonergan, M. C., Limits of Contact Selectivity/Recombination on the Open-Circuit Voltage of a Photovoltaic. *ACS Applied Energy Materials* **2018,** *1*, 1037-1046.
28. Oener, S. Z.; Cavalli, A.; Sun, H.; Haverkort, J. E. M.; Bakkers, E. P. A. M.; Garnett, E. C., Charge Carrier-Selective Contacts for Nanowire Solar Cells. *Nat Commun* **2018,** *9* (1), 3248.
29. Hussey, R. J.; Sproule, G. I.; McCaffrey, J. P.; Graham, M. J., Characterization of Oxides Formed on InP, InGaAs, InAlAs, and InGaAs{/}InAlAs Heterostructures at 300–500°C. *Oxidation of Metals* **2002,** *57* (5/6), 427-447.
30. Lundström, I.; DiStefano, T., Hydrogen Induced Interfacial Polarization at Pd-SiO2 Interfaces. *Surface Science* **1976,** *59* (1), 23-32.
31. Lundström, I., Hydrogen Sensitive MOS-Structures. *Sensors and Actuators* **1981,** *1*, 403-426.
32. Armgarth, M.; Söderberg, D.; Lundström, I., Palladium and Platinum Gate Metal-oxide-semiconductor Capacitors in Hydrogen and Oxygen Mixtures. *Appl. Phys. Lett.* **1982,** *41* (7), 654-655.

33. Nellist, M. R.; Laskowski, F. A. L.; Lin, F.; Mills, T. J.; Boettcher, S. W., Semiconductor–Electrocatalyst Interfaces: Theory, Experiment, and Applications in Photoelectrochemical Water Splitting. *Acc. Chem. Res.* **2016,** *49* (4), 733-740.
34. Laskowski, F. A. L.; Nellist, M. R.; Venkatkarthick, R.; Boettcher, S. W., Junction Behavior of N-Si Photoanodes Protected by Thin Ni Elucidated from Dual Working Electrode Photoelectrochemistry. *Energy Environ. Sci.* **2017,** *10* (2), 570-579.
35. Van de Walle, C. G.; Neugebauer, J., Universal Alignment of Hydrogen Levels in Semiconductors, Insulators and Solutions. *Nature* **2003,** *423* (6940), 626-628.
36. Kumar, M.; Chatterjee, R.; Milikisiyants, S.; Kanjilal, A.; Voelskow, M.; Grambole, D.; Lakshmi, K. V.; Singh, J. P., Investigating the Role of Hydrogen in Indium Oxide Tubular Nanostructures as a Donor or Oxygen Vacancy Passivation Center. *Appl. Phys. Lett.* **2009,** *95* (1), 013102.
37. King, P. D. C.; Lichti, R. L.; Celebi, Y. G.; Gil, J. M.; Vilão, R. C.; Alberto, H. V.; Piroto Duarte, J.; Payne, D. J.; Egdell, R. G.; McKenzie, I.; McConville, C. F.; Cox, S. F. J.; Veal, T. D., Shallow Donor State of Hydrogen in In2O3 and SnO2: Implications for Conductivity in Transparent Conducting Oxides. *Phys. Rev. B* **2009,** *80* (8), 081201.
38. Meléndez, J. J.; Wierzbowska, M., In2O3 Doped with Hydrogen: Electronic Structure and Optical Properties from the Pseudopotential Self-Interaction Corrected Density Functional Theory and the Random Phase Approximation. *J. Phys. Chem. C* **2016,** *120* (7), 4007-4015.
39. Gu, Z.; Zhang, L.; Wen, B.; An, X.; Lan, H.; Liu, L. M.; Chen, T.; Zhang, J.; Cao, X.; Tang, J.; Liu, H.; Qu, J., Efficient Design Principle for Interfacial Charge Separation in Hydrogen-Intercalated Nonstoichiometric Oxides. *Nano Energy* **2018,** *53*, 887-897.
40. Karim, W.; Spreafico, C.; Kleibert, A.; Gobrecht, J.; VandeVondele, J.; Ekinci, Y.; van Bokhoven, J. A., Catalyst Support Effects on Hydrogen Spillover. *Nature* **2017,** *541* (7635), 68-71.
41. Kao, Y. C.; Chou, H. M.; Hsu, S. C.; Lin, A.; Lin, C. C.; Shih, Z. H.; Chang, C. L.; Hong, H. F.; Horng, R. H., Performance Comparison of III–V//Si and III–V//InGaAs Multi-Junction Solar Cells Fabricated by the Combination of Mechanical Stacking and Wire Bonding. *Scientific Reports* **2019,** *9* (1), 4308.
42. Lin, J.; Wang, W.; Li, G., Modulating Surface/Interface Structure of Emerging InGaN Nanowires for Efficient Photoelectrochemical Water Splitting. *Adv. Funct. Mater.* **2020,** *30* (52), 2005677.
43. Cooper, J. K.; Scott, S. B.; Ling, Y.; Yang, J.; Hao, S.; Li, Y.; Toma, F. M.; Stutzmann, M.; Lakshmi, K. V.; Sharp, I. D., Role of Hydrogen in Defining the N-Type Character of BiVO4 Photoanodes. *Chem. Mater.* **2016,** *28* (16), 5761-5771.
44. Filippone, F.; Mattioli, G.; Polimeni, A.; Felici, M.; Bonapasta, A. A., Opposite Hydrogen Behaviors in GaAsN and InAsN Alloys: Band Gap Opening Versus Donor Doping. *J. Phys. Chem. C* **2020,** *124* (35), 19240-19251.

B.b. Supplemental
Style: ACS Energy Letters

1. Hollinger, G.; Bergignat, E.; Joseph, J.; Robach, Y., On the Nature of Oxides on InP Surfaces. *Journal of Vacuum Science & Technology A* **1985,** *3* (6), 2082-2088.
2. Faur, M.; Faur, M.; Jayne, D. T.; Goradia, M.; Goradia, C., XPS Investigation of Anodic Oxides Grown on P-Type InP. *Surface and Interface Analysis* **1990,** *15* (11), 641-650.
3. Hussey, R. J.; Sproule, G. I.; McCaffrey, J. P.; Graham, M. J., Characterization of Oxides Formed on InP, InGaAs, InAlAs, and InGaAs{/}InAlAs Heterostructures at 300–500°C. *Oxidation of Metals* **2002,** *57* (5/6), 427-447.
4. Muñoz, A. G.; Heine, C.; Lublow, M.; Klemm, H. W.; Szabó, N.; Hannappel, T.; Lewerenz, H. J., Photoelectrochemical Conditioning of MOVPE P-InP Films for Light-Induced Hydrogen Evolution: Chemical, Electronic and Optical Properties. *ECS J. Solid State Sci. Technol.* **2013,** *2* (4), Q51-Q58.
5. Cuypers, D.; van Dorp, D. H.; Tallarida, M.; Brizzi, S.; Conard, T.; Rodriguez, L. N. J.; Mees, M.; Arnauts, S.; Schmeisser, D.; Adelmann, C.; De Gendt, S., Study of InP Surfaces after Wet Chemical Treatments. *ECS J. Solid State Sci. Technol.* **2014,** *3* (1), N3016-N3022.
6. Hofmann, A.; Streubel, P.; Meisel, A., XPS Investigation of Oxide Films on InP(100). *Surf. Interface Anal.* **1988,** *12* (5), 315-319.
7. Faur, M.; Faur, M.; Jenkins, P.; Goradia, M.; Bailey, S.; Jayne, D.; Weinberg, I.; Goradia, C., Study of Surface Passivation of InP. *Surf. Interface Anal.* **1990,** *15* (12), 745-750.
8. Tung, R. T., Electron Transport of Inhomogeneous Schottky Barriers. *Appl. Phys. Lett.* **1991,** *58* (24), 2821-2823.
9. Tung, R. T., Electron Transport at Metal-Semiconductor Interfaces: General Theory. *Phys. Rev. B* **1992,** *45* (23), 13509-13523.
10. Laskowski, F. A. L.; Oener, S. Z.; Nellist, M. R.; Gordon, A. M.; Bain, D. C.; Fehrs, J. L.; Boettcher, S. W., Nanoscale Semiconductor/Catalyst Interfaces in Photoelectrochemistry. *Nature Mater* **2020,** *19* (1), 69-76.
11. Leibovitch, M.; Kronik, L.; Fefer, E.; Korobov, V.; Shapira, Y., Constructing Band Diagrams of Semiconductor Heterojunctions. *Appl. Phys. Lett.* **1995,** *66* (4), 457-459.
12. Tung, R. T., The Physics and Chemistry of the Schottky Barrier Height. *Applied Physics Reviews* **2014,** *1* (1), 011304.
13. Lundström, I.; DiStefano, T., Hydrogen Induced Interfacial Polarization at Pd-SiO2 Interfaces. *Surface Science* **1976,** *59* (1), 23-32.
14. Armgarth, M.; Söderberg, D.; Lundström, I., Palladium and Platinum Gate Metal-oxide-semiconductor Capacitors in Hydrogen and Oxygen Mixtures. *Appl. Phys. Lett.* **1982,** *41* (7), 654-655.
15. Van de Walle, C. G.; Neugebauer, J., Universal Alignment of Hydrogen Levels in Semiconductors, Insulators and Solutions. *Nature* **2003,** *423* (6940), 626-628.

16. Kumar, M.; Chatterjee, R.; Milikisiyants, S.; Kanjilal, A.; Voelskow, M.; Grambole, D.; Lakshmi, K. V.; Singh, J. P., Investigating the Role of Hydrogen in Indium Oxide Tubular Nanostructures as a Donor or Oxygen Vacancy Passivation Center. *Appl. Phys. Lett.* **2009,** *95* (1), 013102.
17. King, P. D. C.; Lichti, R. L.; Celebi, Y. G.; Gil, J. M.; Vilão, R. C.; Alberto, H. V.; Piroto Duarte, J.; Payne, D. J.; Egdell, R. G.; McKenzie, I.; McConville, C. F.; Cox, S. F. J.; Veal, T. D., Shallow Donor State of Hydrogen in In2O3 and SnO2: Implications for Conductivity in Transparent Conducting Oxides. *Phys. Rev. B* **2009,** *80* (8), 081201.
18. Gu, Z.; Zhang, L.; Wen, B.; An, X.; Lan, H.; Liu, L. M.; Chen, T.; Zhang, J.; Cao, X.; Tang, J.; Liu, H.; Qu, J., Efficient Design Principle for Interfacial Charge Separation in Hydrogen-Intercalated Nonstoichiometric Oxides. *Nano Energy* **2018,** *53*, 887-897.

References cited in Paper C:

Style: ACS Energy Letters

1. Lichterman, M. F.; Hu, S.; Richter, M. H.; Crumlin, E. J.; Axnanda, S.; Favaro, M.; Drisdell, W.; Hussain, Z.; Mayer, T.; Brunschwig, B. S.; Lewis, N. S.; Liu, Z.; Lewerenz, H.-J., Direct observation of the energetics at a semiconductor/liquid junction by operando X-ray photoelectron spectroscopy. *Energy & Environmental Science* **2015,** *8* (8), 2409-2416.
2. Axnanda, S.; Crumlin, E. J.; Mao, B.; Rani, S.; Chang, R.; Karlsson, P. G.; Edwards, M. O. M.; Lundqvist, M.; Moberg, R.; Ross, P.; Hussain, Z.; Liu, Z., Using "Tender" X-Ray Ambient Pressure X-Ray Photoelectron Spectroscopy as A Direct Probe of Solid-Liquid Interface. *Sci. Rep.* **2015,** *5* (1), 9788.
3. Lichterman, M. F.; Richter, M. H.; Hu, S.; Crumlin, E. J.; Axnanda, S.; Favaro, M.; Drisdell, W.; Hussain, Z.; Brunschwig, B. S.; Lewis, N. S.; Liu, Z.; Lewerenz, H. J., An Electrochemical, Microtopographical and Ambient Pressure X-Ray Photoelectron Spectroscopic Investigation of Si/TiO2/Ni/Electrolyte Interfaces. *J. Electrochem. Soc.* **2015,** *163* (2), H139.
4. Starr, D. E.; Favaro, M.; Abdi, F. F.; Bluhm, H.; Crumlin, E. J.; van de Krol, R., Combined Soft and Hard X-Ray Ambient Pressure Photoelectron Spectroscopy Studies of Semiconductor/Electrolyte Interfaces. *J. Electron Spectrosc. Relat. Phenom.* **2017,** *221*, 106-115.
5. Dahl, Ø.; Sunding, M. F.; Killi, V.; Svenum, I. H.; Grandcolas, M.; Andreassen, M.; Nilsen, O.; Thøgersen, A.; Jensen, I. J. T.; Chatzitakis, A., Interrogation of the Interfacial Energetics at a Tantalum Nitride/Electrolyte Heterojunction during Photoelectrochemical Water Splitting by Operando Ambient Pressure X-Ray Photoelectron Spectroscopy. *ACS Catal.* **2023,** *13* (17), 11762-11770.
6. Carvalho, O. Q.; Crumlin, E. J.; Stoerzinger, K. A., X-Ray and Electron Spectroscopy of (Photo)Electrocatalysts: Understanding Activity through Electronic Structure and Adsorbate Coverage. *J. Vac. Sci. Technol. A* **2021,** *39* (4), 040802.
7. Favaro, M.; Clark, P. C. J.; Sear, M. J.; Johansson, M.; Maehl, S.; van de Krol, R.; Starr, D. E., Spectroscopic Analysis with Tender X-Rays: SpAnTeX, a New AP-HAXPES End-Station at BESSY II. *Surf. Sci.* **2021,** *713*, 121903.
8. Barawi, M.; Mesa, C. A.; Collado, L.; Villar-García, I. J.; Oropeza, F.; O'Shea, V. A. d. l. P.; García-Tecedor, M., Latest Advances in in Situ and Operando X-Ray-Based Techniques for the Characterisation of Photoelectrocatalytic Systems. *J. Mater. Chem. A* **2024,** *12* (35), 23125-23146.
9. Teeter, G.; Harvey, S. P.; Perkins, C. L.; Ramanathan, K.; Repins, I. L., Comparative Operando XPS Studies of Quasi-Fermi Level Splitting and Open-Circuit Voltage in CZTSe/CdS and CIGS/CdS Junctions and Device Structures. *J. Vac. Sci. Technol. A* **2019,** *37* (3), 031202.
10. Siol, S.; Schulz, P.; Young, M.; Borup, K. A.; Teeter, G.; Zakutayev, A., Combinatorial In Situ Photoelectron Spectroscopy Investigation of Sb2Se3/ZnS Heterointerfaces. *Adv. Mater. Interfaces* **2016,** *3* (24), 1600755.
11. Çopuroğlu, M.; Sezen, H.; Opila, R. L.; Suzer, S., Band-Bending at Buried SiO2/Si Interface as Probed by XPS. *ACS Appl. Mater. Interfaces* **2013,** *5* (12), 5875-5881.
12. Sezen, H.; Ozbay, E.; Suzer, S., XPS for Probing the Dynamics of Surface Voltage and Photovoltage in GaN. *Appl. Surf. Sci.* **2014,** *323*, 25-30.

13. Favaro, M.; Jeong, B.; Ross, P. N.; Yano, J.; Hussain, Z.; Liu, Z.; Crumlin, E. J., Unravelling the Electrochemical Double Layer by Direct Probing of the Solid/Liquid Interface. *Nat. Commun.* **2016,** *7* (1), 12695.
14. Wesley, T. S.; Hülsey, M. J.; Westendorff, K. S.; Lewis, N. B.; Crumlin, E. J.; Román-Leshkov, Y.; Surendranath, Y., Metal Nanoparticles Supported on a Nonconductive Oxide Undergo pH-Dependent Spontaneous Polarization. *Chem. Sci.* **2023,** *14* (26), 7154-7160.

References cited in Paper D:

Style: ACS Energy Letters

1. Teeter, G.; Harvey, S. P.; Perkins, C. L.; Ramanathan, K.; Repins, I. L., Comparative Operando XPS Studies of Quasi-Fermi Level Splitting and Open-Circuit Voltage in CZTSe/CdS and CIGS/CdS Junctions and Device Structures. *J. Vac. Sci. Technol. A* **2019,** *37* (3), 031202.
2. Varadhan, P.; Fu, H. C.; Priante, D.; Retamal, J. R. D.; Zhao, C.; Ebaid, M.; Ng, T. K.; Ajia, I.; Mitra, S.; Roqan, I. S.; Ooi, B. S.; He, J. H., Surface Passivation of GaN Nanowires for Enhanced Photoelectrochemical Water-Splitting. *Nano Lett.* **2017,** *17* (3), 1520–1528.
3. Muñoz, A. G.; Heine, C.; Klemm, H. W.; Hannappel, T.; Szabo, N.; Lewerenz, H. J., Electrochemical Passivation of Homoepitaxial InP (100) Thin Films for Light Induced Hydrogen Evolution: A Synchrotron Radiation Photoelectron Spectroscopy Study. *ECS Trans.* **2019,** *35* (8), 141–150.
4. Kaufman, A. J.; Krivina, R. A.; Shen, M.; Boettcher, S. W., Controlling Catalyst–Semiconductor Contacts: Interfacial Charge Separation in p-InP Photocathodes. *ACS Energy Lett.* **2022,** *7* (1), 541–549.
5. Xiao, Y.; Kong, X.; Vanka, S.; Dong, W. J.; Zeng, G.; Ye, Z.; Sun, K.; Navid, I. A.; Zhou, B.; Toma, F. M.; Guo, H.; Mi, Z., Oxynitrides Enabled Photoelectrochemical Water Splitting with over 3,000 Hrs Stable Operation in Practical Two-Electrode Configuration. *Nat. Commun.* **2023,** *14* (1), 2047.

References cited in Paper E:

Style: Nature Materials

1 Takata, T. & et al. Photocatalytic water splitting with a quantum efficiency of almost unity. *Nature* **581**, 411-414 (2020).

2 Jiang, J., Kato, K., Fujimori, H., Yamakata, A. & Sakata, Y. Investigation on the highly active SrTiO3 photocatalyst toward overall H2O splitting by doping Na ion. *Journal of Catalysis* **390**, 81-89, doi:10.1016/j.jcat.2020.07.025 (2020).

3 Iwase, A. *et al.* Water Splitting and CO2 Reduction under Visible Light Irradiation Using Z-Scheme Systems Consisting of Metal Sulfides, CoOx-Loaded BiVO4, and a Reduced Graphene Oxide Electron Mediator. *J Am Chem Soc* **138**, 10260-10264, doi:10.1021/jacs.6b05304 (2016).

4 Takata, T. & Domen, K. Particulate Photocatalysts for Water Splitting: Recent Advances and Future Prospects. *ACS Energy Letters* **4**, 542-549, doi:10.1021/acsenergylett.8b02209 (2019).

5 Kato, H., Sasaki, Y., Shirakura, N. & Kudo, A. Synthesis of highly active rhodium-doped SrTiO3 powders in Z-scheme systems for visible-light-driven photocatalytic overall water splitting. *Journal of Materials Chemistry A* **1**, 12327, doi:10.1039/c3ta12803b (2013).

6 Kay, A., Cesar, I. & Grätzel, M. New Benchmark for Water Photooxidation by Nanostructured α-Fe2 O3 Films. *J. Am. Chem. Soc.* **128**, 15714-15721 (2006).

7 Maeda, K. & Domen, K. Photocatalytic Water Splitting: Recent Progress and Future Challenges. *J. Phys. Chem. Lett.* **1**, 2655-2661 (2010).

8 Han, H. S. & et al. Boosting the solar water oxidation performance of a BiVO4 photoanode by crystallographic orientation control. *Energy Environ. Sci.* **11**, 1299-1306 (2018).

9 Mu, L. & et al. Enhancing charge separation on high symmetry SrTiO3 exposed with anisotropic facets for photocatalytic water splitting. *Energy Environ. Sci.* **9**, 2463-2469 (2016).

10 Chen, S., Takata, T. & Domen, K. Particulate photocatalysts for overall water splitting. *Nature Reviews Materials* **2**, 17050, doi:10.1038/natrevmats.2017.50 (2017).

11 Hsieh, P. L. & et al. Facet-Dependent and Adjacent Facet-Related Electrical Conductivity Properties of SrTiO3 Crystals. *J. Phys. Chem. C* **125**, 10051-10056 (2021).

12 Kumar, G., Chen, Z. L., Jena, S. & Huang, M. H. Facet-dependent optical and electrical properties of SrTiO3 wafers. *J. Mater. Chem. C* **11**, 3885-3888 (2023).

13 Assavachin, S., Xiao, C., Becker, K. & Osterloh, F. E. Facets control charge separation during photoelectrochemical water oxidation with strontium titanate (SrTiO3) single crystals. *Energy Environ. Sci.* **17**, 3493-3502 (2024).

14 Pan, Z. *et al.* Mutually-dependent kinetics and energetics of photocatalyst/co-catalyst/two-redox liquid junctions. *Energy & Environmental Science* **13**, 162-173, doi:10.1039/C9EE02910A (2020).

15 Kaufman, A. J. *et al.* Absolute band-edge energies are over-emphasized in the design of photoelectrochemical materials. *Nature Catalysis* **7**, 615-623, doi:10.1038/s41929-024-01161-0 (2024).
16 Roe, E. T., Egelhofer, K. E. & Lonergan, M. C. Limits of Contact Selectivity/Recombination on the Open-Circuit Voltage of a Photovoltaic. *ACS Applied Energy Materials* **1**, 1037-1046, doi:10.1021/acsaem.7b00179 (2018).
17 Nellist, M. R., Laskowski, F. A. L., Lin, F., Mills, T. J. & Boettcher, S. W. Semiconductor–Electrocatalyst Interfaces: Theory, Experiment, and Applications in Photoelectrochemical Water Splitting. *Acc. Chem. Res.* **49**, 733-740, doi:10.1021/acs.accounts.6b00001 (2016).
18 Wagner, F. T. & Somorjai, G. A. Photocatalytic and photoelectrochemical hydrogen production on strontium titanate single crystals. *J. Am. Chem. Soc.* **102**, 5494-5502 (1980).
19 Wagner, F. T., Ferrer, S. & Somorjai, G. A. Photocatalytic hydrogen production from water over SrTiO3 crystal surfaces, electron spectroscopy studies of adsorbed H2, O2 and H2O. *Surface Science* **101**, 462-474 (1980).
20 Mu, L., Zeng, B., Tao, X., Zhao, Y. & Li, C. Unusual Charge Distribution on the Facet of a SrTiO(3) Nanocube under Light Irradiation. *J Phys Chem Lett* **10**, 1212-1216, doi:10.1021/acs.jpclett.9b00243 (2019).
21 Takata, T. *et al.* Photocatalytic Water Splitting with a Quantum Efficiency of Almost Unity. *Nature* **581**, 411-414, doi:10.1038/s41586-020-2278-9 (2020).
22 Lichterman, M. F. *et al.* Direct Observation of the Energetics at a Semiconductor/Liquid Junction by Operando X-Ray Photoelectron Spectroscopy. *Energy Environ. Sci.* **8**, 2409-2416, doi:10.1039/C5EE01014D (2015).
23 Lichterman, M. F. *et al.* An Electrochemical, Microtopographical and Ambient Pressure X-Ray Photoelectron Spectroscopic Investigation of Si/TiO2/Ni/Electrolyte Interfaces. *J. Electrochem. Soc.* **163**, H139, doi:10.1149/2.0861602jes (2015).
24 Axnanda, S. *et al.* Using "Tender" X-Ray Ambient Pressure X-Ray Photoelectron Spectroscopy as A Direct Probe of Solid-Liquid Interface. *Sci. Rep.* **5**, 9788, doi:10.1038/srep09788 (2015).
25 Wesley, T. S. *et al.* Metal nanoparticles supported on a nonconductive oxide undergo pH-dependent spontaneous polarization. *Chem Sci* **14**, 7154-7160, doi:10.1039/d3sc00884c (2023).
26 Marshall, M. S. J., Becerra-Toledo, A. E., Marks, L. D. & Castell, M. R. Defects on Strontium Titanate. **58**, 327-349, doi:10.1007/978-3-319-14367-5_11 (2015).
27 Lehner, J. M. *et al.* Environmentally Stable p(6 × 2) SrTiO3(001) Surface Reconstruction with Low-Valent Ti for Photocatalytic Water Splitting. *The Journal of Physical Chemistry C* **127**, 17285-17289, doi:10.1021/acs.jpcc.3c04514 (2023).
28 Shimizu, R. *et al.* Effect of oxygen deficiency on SrTiO3(001) surface reconstructions. *Applied Physics Letters* **100**, 263106, doi:10.1063/1.4730409 (2012).
29 Wang, Z. *et al.* Strain-induced defect superstructure on the SrTiO3(110) surface. *Phys Rev Lett* **111**, 056101, doi:10.1103/PhysRevLett.111.056101 (2013).
30 Ye, H., Park, H. S. & Bard, A. J. Screening of Electrocatalysts for Photoelectrochemical Water Oxidation on W-Doped BiVO4 Photocatalysts by Scanning Electrochemical Microscopy. *The Journal of Physical Chemistry C* **115**, 12464-12470, doi:10.1021/jp200852c (2011).

31 Burke, M. S., Kast, M. G., Trotochaud, L., Smith, A. M. & Boettcher, S. W. Cobalt-iron (oxy)hydroxide oxygen evolution electrocatalysts: the role of structure and composition on activity, stability, and mechanism. *J Am Chem Soc* **137**, 3638-3648, doi:10.1021/jacs.5b00281 (2015).
32 Favaro, M. *et al.* Understanding the Oxygen Evolution Reaction Mechanism on CoO(x) using Operando Ambient-Pressure X-ray Photoelectron Spectroscopy. *J Am Chem Soc* **139**, 8960-8970, doi:10.1021/jacs.7b03211 (2017).
33 Han, Y. *et al.* Observing the Electrochemical Oxidation of Co Metal at the Solid/Liquid Interface Using Ambient Pressure X-ray Photoelectron Spectroscopy. *J Phys Chem B* **122**, 666-671, doi:10.1021/acs.jpcb.7b05982 (2018).
34 Gu, H., Wang, Z. & Hu, Y. Hydrogen Gas Sensors Based on Semiconductor Oxide Nanostructures. *Sensors* **12**, 5517-5550 (2012).
35 Saeed, S. W. & Bjørheim, T. S. The Role of Space Charge at Metal/Oxide Interfaces in Proton Ceramic Electrochemical Cells. *J. Phys. Chem. C* **124**, 20827-20833 (2020).
36 Suzuki, T. T., Ohgaki, T., Adachi, Y. & Sakaguchi, I. Polarity reversal of resistance response to trace H2 gas in the air between asymmetrically shaped electrodes on rutile-TiO2 single crystal. *Journal of Applied Physics* **131**, 034501 (2022).
37 Ma, T., Jacobs, R., Booske, J. & Morgan, D. Understanding the interplay of surface structure and work function in oxides: A case study on SrTiO3. *APL Materials* **8**, 071110 (2020).
38 Mu, L., Zeng, B., Tao, X., Zhao, Y. & Li, C. Unusual Charge Distribution on the Facet of a SrTiO3 Nanocube under Light Irradiation. *J. Phys. Chem. Lett.* **10**, 1212-1216 (2019).
39 Hofstein, S. R. & Warfield, G. Physical limitations on the frequency response of a semiconductor surface inversion layer. *Solid-State Electronics* **8**, 321-341, doi:10.1016/0038-1101(65)90148-6 (1965).
40 Pan, Z. *et al.* Elucidating charge separation in particulate photocatalysts using nearly intrinsic semiconductors with small asymmetric band bending. *Sustainable Energy & Fuels* **3**, 850-864, doi:10.1039/C9SE00036D (2019).
41 Pan, Z. & et al. Mutually-dependent kinetics and energetics of photocatalyst/co-catalyst/two-redox liquid junctions. *Energy Environ. Sci.* **13**, 162-173 (2020).